New Nanostructured Aluminosilicates from Geopolymer Chemistry

by

Dinesh Medpelli

A Dissertation Presented in Partial Fulfillment
of the Requirements for the Degree
Doctor of Philosophy

Approved February 2015 by the
Graduate Supervisory Committee:

Dong-Kyun Seo, Chair
Pierre Herckes
William Petuskey

ARIZONA STATE UNIVERSITY

May 2015

ABSTRACT

Geopolymers, a class of X-ray amorphous, ceramic-like aluminosilicate materials are produced at ambient temperatures through a process called geopolymerization. Due to both low energy requirement during synthesis and interesting mechanical and chemical properties, geopolymers are grabbing enormous attention. Although geopolymers have a broad range of applications including thermal/acoustic insulation and waste immobilization, they are always prepared in monolithic form. The primary aim of this study is to produce new nanostructured materials from the geopolymerization process, including porous monoliths and powders.

In view of the current interest in porous geopolymers for non-traditional applications, it is becoming increasingly important to develop synthetic techniques to introduce interconnected pores into the geopolymers. This study presents a simple synthetic route to produce hierarchically porous geopolymers via a reactive emulsion templating process utilizing triglyceride oil. In this new method, highly alkaline geopolymer resin is mixed with canola oil to form a homogeneous viscous emulsion which, when cured at 60 °C, gives a hard monolithic material. During the process, the oil in the alkaline emulsion undergoes a saponification reaction to decompose into water-soluble soap and glycerol molecules which are extracted to yield porous geopolymers. Nitrogen sorption studies indicates the presence of mesopores, whereas the SEM studies reveals that the mesoporous geopolymer matrix is dotted with spherical macropores. The method exhibits flexibility in that the pore structure of the final porous geopolymers products can be adjusted by varying the precursor composition.

In a second method, the geopolymerization process is modified to produce highly dispersible geopolymer particles, by activating metakaolin with sodium silicate solutions containing excess alkali, and curing for short duration under moist conditions. The produced geopolymer particles exhibit morphology similar to carbon blacks and structured silicas, while also being stable over a wide pH range.

Finally, highly crystalline hierarchical faujasite zeolites are prepared by yet another modification of the geopolymerization process. In this technique, the second method is combined with a saponification reaction of triglyceride oil. The resulting hierarchical zeolites exhibit superior CO_2-sorption properties compared to equivalent commercially available and currently reported materials. Additionally, the simplicity of all three of these techniques means they are readily scalable.

DEDICATION

To my parents (Buchi Reddy and Vasantha), wife (Harini), sister (Priyanka), and niece (SriKruthi).

ACKNOWLEDGMENTS

First and foremost, I would like to thank my Mom and Dad for all of their sacrifices while bringing me up, for their constant encouragement, and for the influence they have had on me that will benefit my entire life. I would also like to thank my wife Harini for making the last few hurdles of my grad school go smoothly. Special thanks to my brother-in-law for taking care of me and my family, and to my sister for a little bit of everything.

I am also very grateful to Professor Seo, my supervisor, for providing me with an opportunity to work on this challenging and interesting project, and for always having time for me and my research. His guidance and support are highly appreciated. I am indebted to him for helping me in every aspect of being a good researcher. I would also like to extend my most sincere thanks to Prof. Petuskey and Prof. Herckes, my committee members, for always finding time and effort to contribute toward my success. In addition, my special thanks go to collaborators, Prof. Hristovski, Dr. Wong, Prof. Akthar, and Robert for their much appreciated contributions.

I would also like to thank my group members and all the friends I have made during my time here in graduate school. Special thanks to Samudra, Daniel, Arnab, Manas, Souvik, Basab, Kiwan, Rakesh, Das, Alex and Danielle for always being available and making my life much easier. I will never forget some of our activities, and scientific and not so scientific conversations.

I am also grateful to the funding agencies and everyone who have helped be along the way. Now I am ready to go out into the real world.

TABLE OF CONTENTS

Page

CHAPTER Page

LIST OF TABLES

LIST OF FIGURES

Figure Page

Figure Page

Figure Page

Figure Page

Figure Page

Figure Page

Figure Page

Figure Page

CHAPTER 1

1. INTRODUCTION

1.1. Silicates and Aluminosilicates

Oxygen and silicon are the first and second most abundant elements in the Earth's crust, respectively. Consequently, an enormous number of different forms of silicon-oxygen-based minerals exist accompanied by numerous other synthetic compounds. Under normal conditions of temperature and pressure, Si exists in a +4 oxidation state in combination with oxygen atoms and prefers a coordination number of four with a tetrahedral atomic environment – both in minerals and synthetic compounds. The essential building block of silicon found in silicates and aluminosilicates can be written simply as SiO_4^{4-}. These tetrahedral SiO_4^{4-} units have a strong tendency to polymerize into larger units via shared oxygens to form silicate minerals and compounds. In isolated SiO_4^{4-} compounds (ortho-silicates), the Si:O atomic ratio is 1:4, which decreases with the degree of polymerization of SiO_4^{4-} units. When SiO_4^{4-} units are fully polymerized as in the case of three-dimensional network structures, the ratio of Si:O ratio is at its minimum value of 1:2. These three-dimensional network structures can either be crystalline – in which case they are more famously known as tectosilicates, or be amorphous. Tectosilicates comprise nearly 75% of the crust of the Earth. With the exception of the quartz group, all tectosilicates are aluminosilicates, containing aluminum in addition to silicon.

An additional level of complexity is introduced when aluminum (the third most abundant element in the Earth's crust) replaces some of the silicon atoms to form

aluminosilicates. Since Al is highly electropositive and exists exclusively in a +3 oxidation state in combination with oxygen atoms, the normal silicate tetrahedral arrangement gets interrupted and thereby present fascinating consequences in structures and compositions. For each Si atom replaced by an Al atom, a deficiency in the electrical charge occurs which must be locally balanced by having other positive ions such as Na^+, K^+, and Ca^{2+} ions within the interstices of the structure. In addition to a coordination number of four, Al may also adopt coordination number of 6 with an octahedral atomic environment leading to the formation of many interesting structures. One such formation is layered structures such as clays which consist of aluminum in a six-fold coordination with oxygens. These layered structures do not have three-dimensional stability and may expand if the layers are forced apart by water, other molecules, or ions.

The aluminosilicate structures that result from mutual sharing of oxygens of SiO_4 and AlO_4 tetrahedra in three dimensions (network structures) may be crystalline or amorphous.[1] If such structures are crystalline, they are termed framework structures – feldspar, sodalite and zeolite are the three largest and the most common groups of this kind of aluminosilicates. Whereas, geopolymers and precipitated aluminosilicates are considered the amorphous analogues. This thesis will be exclusively focused on aluminosilicates with fully polymerized tetrahedra that are linked in a three dimensional array, namely, sodalites, zeolites, geopolymers, and precipitated aluminosilicates.

1.2. Sodalites

Sodalite means sodium stone and it was given this name by Thompson in 1811. The sodalite group is formed by approximately equal number of SiO_4 and AlO_4

tetrahedra linked by sharing corner oxygens, and Al and Si are completely ordered. In sodalite, cage-like truncated octahedra (sodalite or β-cage) are formed by binding six rings of four tetrahedra parallel to {100} and eight rings of six tetrahedra parallel to {111}. The six-membered rings define a set of channels which intersect to form large cavities. The framework has the composition $Na_6Al_6Si_6O_{24}$ but may have additional anions such as chlorine ions in the cavities which are tetrahedrally coordinated by sodium ions (Na_4-Cl units). Sodalite is one of the members of the sodalite group minerals and it contains chlorine as an essential constituent. Occasionally some of the sodium in the sodalite may be substituted by potassium or calcium.[2] Since sodalite has a very limited sorption capacity due to the presence of very narrow six ring windows, it is not considered a zeolite. Nevertheless, its low framework density (17.2 T-atoms per 1000 $Å^3$) is within the range of those for zeolites.[3]

1.3. Zeolites

Zeolites are the most important members of a diverse range of microporous materials. Traditionally, the term 'zeolite' refers to crystalline aluminosilicates or silica polymorphs based on corner-sharing TO_4 (T = Si or Al) tetrahedra forming a three-dimensional framework with homogeneously-sized and -shaped openings and voids of molecular dimensions.[4] Nowadays, the term zeolite framework generally refers to a corner sharing network of tetrahedrally coordinated atoms, and the framework elements are not limited to Al and Si atoms alone but other atoms such as P, Ti, B, Ga, Be and Ge etc., may be involved. Currently there are 225 zeolite structure types, as recognized by the International Zeolites Association,[5] each differentiated by a specific delineation, such

as the size of the rings, window/aperture opening, cage dimensions, charge density, framework density (FD, the number of T-atoms per 1000 $Å^3$), and the types of pores.

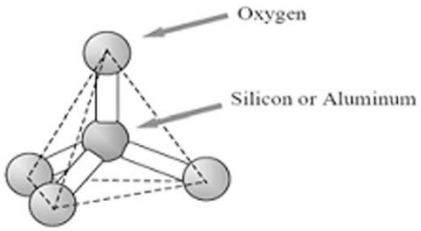

Figure 1. Primary building unit of zeolite structure, the TO_4 tetrahedra (T = Si or Al).

Structurally, the tetrahedra of T-atoms are the primary building units of the zeolites (**Figure 1**), which are connected together to form what are known as secondary building units (SBUs). SBUs are small groups of tetrahedra connected together to form specific groups (**Figure 2**).[6] Within each SBU, Si and Al atoms are located where the lines in the images meet (T sites) and the oxygen atoms are considered to be at the center of each line.

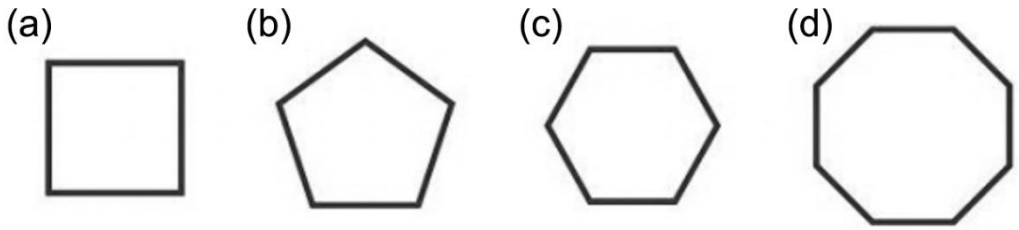

Figure 2. Selected secondary building units (SBU's): single 4-ring, S4R (a), single 5-ring, S5R (b), single 6-ring, 6R (c), and single 8-ring, 8R (d), introduced by Meier and Smith.[7]

These SBUs are in turn connected together to form larger 'cage-like' structures known as cage-building units or composite building units (CBUs) (**Figure 3**). These CBUs are named and identified so as to provide a way to classify zeolites based on their

structural framework. The CBUs are then connected together to form the overall framework structure of the zeolite. The same CBU unit may form different framework types via different linkages. For example, the SOD cages (or β-cages) can be linked (1) by sharing 4-rings giving rise to SOD (sodalite) framework; (2) through double 4-rings to form LTA (Linde Type-A) framework; and (3) via double 6-rings forming FAU (Faujasite Type) and EMT frameworks. Every distinct zeolite framework is given its own three letter unique framework type code.[8] For example, faujasites have the framework type code FAU.

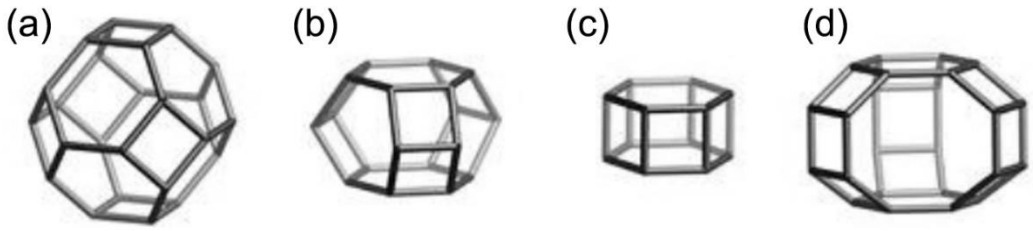

Figure 3. Selected cage-building units (CBUs): SOD (a), CAN (b), D6R (c), and GME (d) cages in known zeolites.

The connection of cages to form the framework further creates the pores through the structure. The pore size is defined by the minimum ring size which limits the pore, which is usually a 8 or 10 membered ring. While defining the rings or pore sizes, only the T-sites are counted. Depending on the framework structure, the created pores may be one, two or three-dimensional in nature as shown in **Figure 4**. If there is more than one kind of pore structure in the framework, they may be interconnected or entirely separated from one another (**Figure 5**).

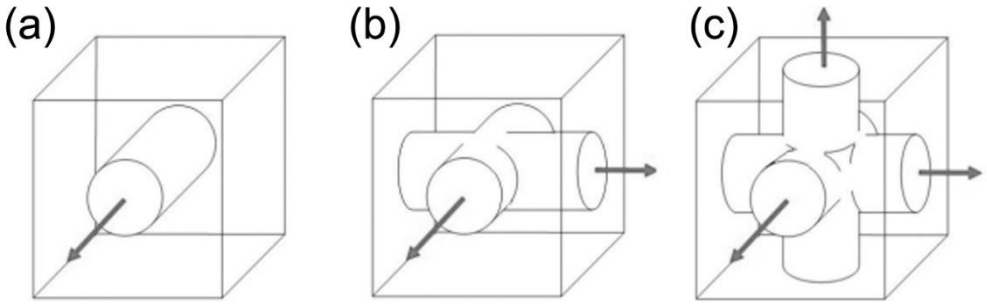

Figure 4. Interconnected pores in one dimension (a), in two dimensions (b), and in three dimensions (c), adapted from Holmes.[9]

Aluminosilicate zeolites may be represented by the empirical formula:

$$M_{2/n}O \cdot Al_2O_3 \cdot xSiO_2 \cdot yH_2O$$

In this oxide formula, x is generally greater than or equal to 2, which is governed by Lowenstein's rule,[10] which states that no two AlO_4 tetrahedra can be adjacent to each other within the framework, meaning every AlO_4 tetrahedron must be surrounded by four SiO_4 tetrahedra; n is the cation valency. Whereas, the structural formula of a zeolite is best expressed for the crystallographic unit cell as:

$$M_{2/n}[(AlO_2)_x(SiO_2)_y] \cdot wH_2O$$

where M is the cation of valency n, w is the number of water molecules and the ratio y/x has a value greater than or equal to 1 depending on the structure. The sum $(x + y)$ is the total number of tetrahedra in a unit cell.[11]

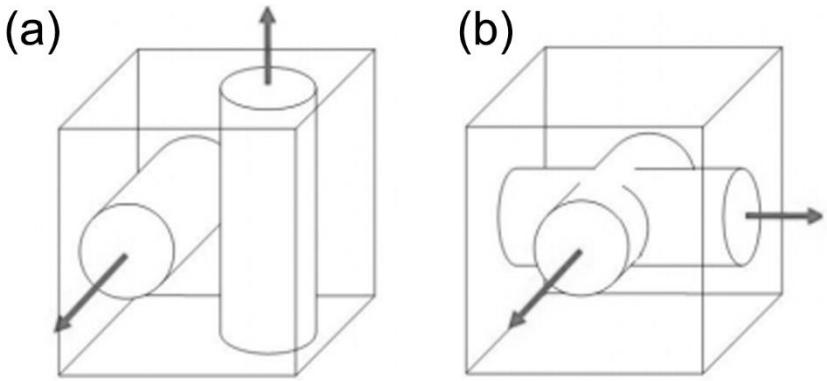

Figure 5. Independent pore systems that are not connected (a), and interconnected (b), adapted from Holmes.[9]

Zeolites can be found naturally as well as synthesized in the laboratory. Natural zeolites were first discovered in 1756 by Swedish mineralogist Cronstedt,[12] but their microporous properties and usefulness in adsorption and ion exchange were gradually recognized only in the 19th century. As of 2007, over 40 types of natural zeolites have been discovered and are widely used for drying and separation of gases and liquids, softening of hard water, treatment of sewage, and melioration of soils. Although natural zeolites lack in purity desired for catalytic applications, some well selected and modified ones are also used as catalysts or as supports for catalysts in the industry.[13]

Early efforts to prepare synthetic zeolites were led by geologists and mineralogists by methods which were believed to simulate natural processes (geothermal conditions) i.e., high-temperatures (above 200 °C) and corresponding elevated pressures associated with hydrothermal conditions. These attempts lasted several decades without any real success. In late 1930's there was a huge demand for zeolites in the industry which led to an initiation of great efforts to prepare synthetic zeolites. Part of the demand can be attributed to their newly found catalytic properties. In the context of cracking

hydrocarbons, these new catalysts possessed all of the properties required of a successful catalyst: activity, stability, selectivity, correct pore size, resistance to fouling, and low cost. The first ever synthetic zeolite was A-type zeolite (LTA) having a Si/Al ratio of 1, prepared by Union Carbide in 1949. It exhibited a very high ion-exchange capacity but it was not possible to convert it into acidic form, stable in the conditions suitable for the FCC-technology. Zeolite X with faujasite structure (FAU), having a Si/Al ratio of 1.2 was synthesized in Na-form in 1950 but it was inactive as an acid catalyst. To obtain acid catalytic activity, X-zeolite was ion-exchanged with rare-earths, mainly lanthanum and/or cerium. Once it was realized that zeolite can be prepared under mild hydrothermal (~ 100 °C and autogenous pressures) conditions – a criteria very important for the commercial synthesis; as opposed to geothermal conditions, a number of companies in the United States, such as Linde, UCC, Mobil, and Exxon invested research efforts towards synthesizing zeolites. The period of 1954 to early 1980s is considered as the golden age for the development of synthetic zeolites. By the end of 1954, zeolites A and X began to be produced industrially. In late 1950's Breck et al. prepared Y-zeolite (FAU structure) with Si/Al = 2.5 – 3, which could be ion exchanged to prepare ammonium form, and by calcinations convert into H-form, possessing strong Brønsted acid sites.[14] Later a method to stabilize Y-zeolite into an exceptionally stable form called as "ultrastable zeolites Y" – USY was developed, which played an extremely important role in the catalysis of hydrocarbon conversion. By 1964 Y-zeolite was synthesized commercially and found its way into refineries as an FCC catalyst.[15] From then on, a variety of zeolites composed of diverse structures with a range of Si/Al ratios, including pure silica polymorphs are developed. Even today USY remains the unrivaled catalyst

for petroleum cracking and hydrocracking processes, with an annual consumption of 2,000,000 tons.

Nowadays, aluminosilicate zeolites with low Si/Al ratios are usually prepared from alkaline solutions of silicates and aluminates under mild hydrothermal conditions (~100 °C and autogenous pressures). Instead, those with higher Si/Al ratios are typically synthesized from alkaline solutions containing additional components like quaternary ammonium cations, which are often called structure directing agents (SDAs). Post-synthesis, SDAs are removed via appropriate calcination steps. Synthetic zeolite crystals are typically in the size range ca. one to several microns. Such crystals are usually called conventional zeolites in the literature.

1.4. Geopolymers

Geopolymers are up-and-coming, relatively new ceramic-like aluminosilicate that lack long range ordering, at least to a length scale that can be detected by the X-rays. Although amorphous (semi-crystalline, at best), geopolymers are similar to aluminosilicate zeolites in the sense that their fundamental framework is a highly linked three-dimensional network of AlO_4 and SiO_4 tetrahedra. Likewise, the negative charge arising due to the presence of Al^{3+} in four-fold coordination localized on one or more of the bridging oxygens of each AlO_4 tetrahedron is compensated by alkali metal cations. Na and K ions are the most common cations, but others like Li and Cs can also be used. Some geopolymers can also contain alkaline earth cations, particularly Mg and Ca. The structural similarities between geopolymers and zeolitic materials on an atomic to nanometer length scale have been shown experimentally employing ^{29}Si solid-state magic

angle spinning nuclear magnetic resonance spectroscopy (^{29}Si MAS NMR)[16] and electron microscopic analysis, respectively.[17] However, geopolymers are strictly synthetic unlike zeolites which are found as minerals and can also be synthesized. Moreover, due to the lack of crystallinity, geopolymers do not exhibit any regular channels or micropores that are characteristic to zeolites. Geopolymers can be prepared in a wide range of compositions following the formula: $M_2O \cdot mAl_2O_3 \cdot nSiO_2 \cdot yH_2O$, usually with $m = 1$, $2 \leq n \leq 300$ and M represents one or more of the aforementioned alkali metal ions.[18] Nonetheless, the most common "nominal" compositions have been around $n = 4$ and $y = 10$ (M = Na, K or Cs), as they provide the best mechanical properties desirable for construction applications. Many researchers attempted to draw schematic diagrams of the three-dimensional geopolymer structure but owing to the disorder inherent to them and also due to the difficulty of precisely representing a three-dimensional framework in two dimensions, such efforts have not proven to be very successful. The schematic presented by Rowles et al.[16] (**Figure 6**) is widely considered to be the most appropriate representation.[19]

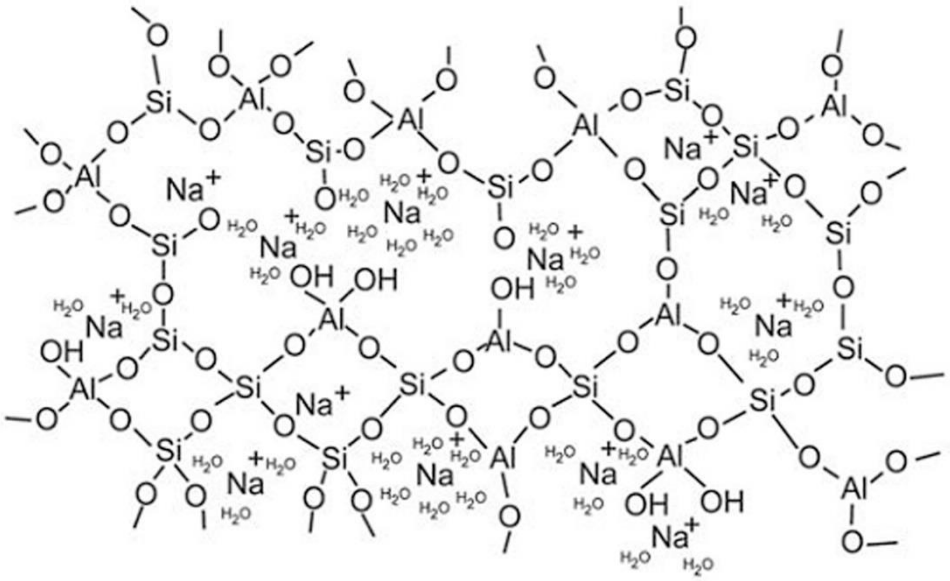

Figure 6. Proposed model of atomic structure of amorphous geopolymer showing charge balancing alkali metal ion (Na^+) in the vicinity of anionic AlO_4 tetrahedra along with the associated H_2O molecules, adapted from Rowles.[16]

In the aftermath of numerous fire disasters involving organic plastics in France between 1970 – 72, Joseph Davidovits started to explore inorganic polymers that can resist fire and consequently chose to develop amorphous to semi-crystalline three-dimensional aluminosilicate materials, which he called geopolymers (mineral polymers resulting from geochemistry or geosynthesis).[20] Even though the early geopolymers were synthesized at high temperatures (150 – 180 °C),[21] recently ambient temperature synthesis has been shown, in some circumstances leading to better products in terms of strength. This low-temperature and, hence, low energy requirement for the synthesis of geopolymers is the main reason behind enormous interest being shown in these materials. Nowadays, geopolymers are typically synthesized at ambient temperatures by alkali

hydroxide- or silicate-activation of a reactive aluminosilicate powders − in particular metakaolin (calcined kaolin clay),[22] or solid aluminosilicates obtained from industrial wastes – chiefly fly ash,[23] melt-quenched aluminosilicates,[24] natural minerals,[25] or mixtures of two or more of these materials.[26] Filler materials as an aggregator or reinforcer such as sand, concrete aggregates like basalt,[27] SiC,[28] carbon fiber[29] and other organic[30] and inorganic fibers[31] (synthetic or natural) to name a few, are sometimes used to enhance desired properties including strength and density.

Different terminologies exist to describe these alkali-activated aluminosilicates, namely, low-temperature aluminosilicate glass, alkali-activated cement, geocement, soil cement, alkali-bonded ceramics, alkali ash material, inorganic polymer concrete, inorganic polymer glasses, and hydroceramics, and a variety of other names.[19b] Irrespective of the terminology adopted, they are all synthesized from the same aforementioned chemistry involving a series of dissolutions, bond rearrangements and precipitations in alkaline mediated aqueous reaction substrate. Encouraged by the expert community during various international symposia dedicated to such a material, "geopolymer" and "inorganic polymer" are the two terms increasingly being used in the recent academic literature.

Geopolymers exhibit a wide range of properties and characteristics like high compressive strength, low shrinkage, fast or slow setting, acid resistance, fire resistance and low thermal conductivity, depending on the raw material used to make them and also the conditions employed to cure them. Due to the said properties, geopolymers have a very broad array of applications such as fire resistant materials,[29, 31] thermal insulators,[32] low-tech building materials,[31, 33] refractory items,[34] low energy ceramic tiles,[35] low-CO_2-

producing cements and concretes,[33, 36] composites for infrastructures repair and strengthening, foundry applications, high-tech resin systems, decorative stone artifacts, radioactive and toxic waste encapsulations,[37] and high-tech composites for aircraft interior and automobiles.[38] However, so far geopolymer technology has been driven by applications rather than technology, hence the geopolymerization process is mechanistically not fully understood yet. To this end, the recent efforts most notably led by Provis and van Deventer, are proving invaluable, although further investigations are necessary.[19b, 39] Out of the many different ways in which geopolymers are synthesized, chemically the simplest system of them all is alkali hydroxide/silicate activated metakaolin, primarily due to the relatively high-purity of metakaolin in comparison to other aluminosilicates sources that are used. This is often considered as the model system, whose results can be conveniently extended to other more complicated systems. Therefore, this thesis will be focused solely on geopolymers formed from alkali hydroxide/silicate activated metakaolin.

In the simplest terms, Provis et al.[17b, 19b] summarized the geopolymerization process to occur via the following four steps:

1) Alkaline attack on the aluminosilicate source resulting in the release of silicate and aluminate species into the solution. In the case of metakaolin system, 5- and 6-coordinated Al is converted into 4-coordinated aluminate species upon dissolution.[40]
2) Transportation of newly formed small dissolved species and the silicates initially supplied in the form of activating solutions occur via water-assisted

mechanism, enabling them to interact. Such interactions results in the formation of aluminosilicate oligomers.

3) Precipitation of dissolved species into an amorphous gel is then triggered once the silicate solution is destabilization by the presence of dissolved aluminate in sufficiently high concentration. This dissolution and gelation occur simultaneously and may be influenced by factors such as mechanical disruption (shearing or ultrasonication), and also the presence of additional particle surfaces (aggregates and/or other added oxides), which may provide nucleation sites.
4) Geopolymer gel with amorphous, cross-linked, three dimensional structure (often referred to as a geopolymeric gel binder phase) grows until the reacting slurry solidifies. The time taken for this is greatly influenced by the mix design and curing temperature, along with the presence or absence of contaminants. Depending on the mix design and the curing temperature, setting can be achieved almost instantaneously, or over a duration of a number of days. In fact, the reaction processes continue for quite some time after the point of setting, as is evident from the ongoing strength development[41] and/or the growth of zeolitic crystallites in some compositions.[42]

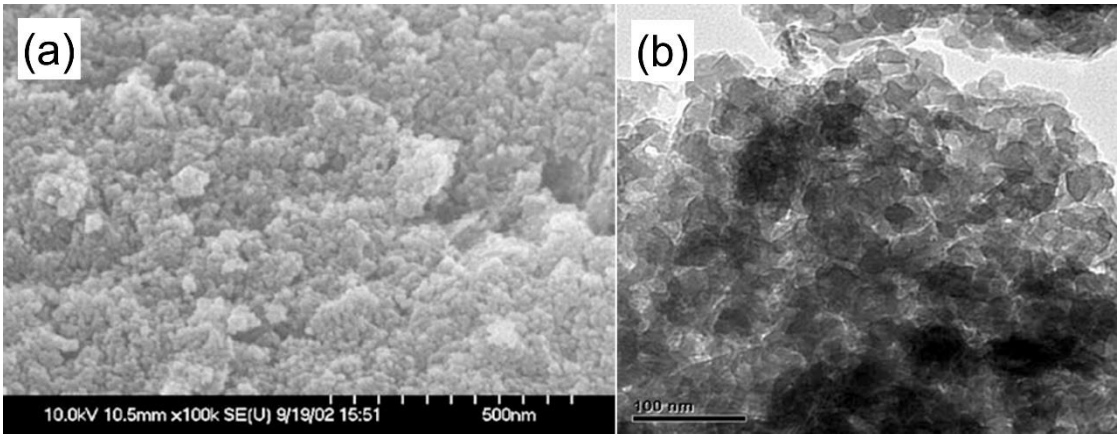

Figure 7. Nanoparticulate meshwork of fully reacted K-geopolymer as revealed by SEM (a), and TEM (b), adapted from Kriven et al.[19a]

Geopolymers are fundamentally a nanostructured material, as they are produced through geopolymer gel formation. Characterization by Kriven et al. using transmission electron microscopy (TEM) and scanning electron microscopy (SEM) has shown that the microstructure of geopolymers consist of a nanoparticulate meshwork of 5 – 40 nm diameter sized particles (**Figure 7a**) separated by nanoporosity whose features are of the order of 3 – 10 nm (**Figure 7b**). Moreover, the diameter of the particles is influenced by the type of alkali ions present. Specifically, the precipitate diameters are of the order of 5–10 nm for sodium-based, 20–30 nm for potassium-based and 30–40 nm for cesium-based geopolymers.[19a] The particles result from dissolution of the aluminosilicate precursor, followed by nucleation and growth of nanometer-sized particles that aggregate at a critical concentration, causing the geopolymer to solidify. The water used in synthesis is expulsed to the pore network, which has a non-uniform morphology. It is emphasized that the dissolution of the aluminosilicate precursors is carried out usually at an extremely high metal concentration range with a typical water content less than 45

wt%. With such limited amounts of water, the network structure of the resulting geopolymer gel is much denser than what is expected for the inorganic gels (such as silica and alumina gel) from typical sol-gel chemistry. Therefore, the internal surfaces of the pore structures of geopolymers are not generally accessible by external molecules.

1.5. Precipitated Aluminosilicates

Precipitated aluminosilicates are synthetic, amorphous materials produced in the form of powders with intricate particulate assembly. As the name suggests, they are prepared by the co-precipitation of silicate and aluminate species from aqueous solutions. Similar to zeolites and geopolymers, precipitated aluminosilicates include charge balancing cations such as Na and Mg ions. Although Al^{3+} in precipitated aluminosilicates is understood to be in a four-fold coordination with a tetrahedral atomic environment, no structural studies have been reported in order to validate such a conclusion. Nearly all of the work dedicated to precipitated aluminosilicates is patented[43] with only a handful of peer-reviewed reports.[44] Moreover, the limited number of available peer-reviewed reports all focus on their applications rather than the structural and/or compositional studies,[45] meaning precipitated aluminosilicates remain an inadequately studied material. Although lacking in atomic structure, their microstructure is reasonably well established. The primary particles of precipitated aluminosilicates are in the nanometer range (~ 10 – 100 nm), which invariably aggregate or agglomerate into irregular shapes with fluffy textured secondary particles that are 5 – 20 μm in size. Owing to their microstructure, they exhibit high surface areas, typically in the range of 60 – 125 m^2/g.

Despite being poorly understood, there is a lot of application-driven interest in them from the industry. Several grades of synthetic amorphous aluminosilicates have been already commercialized by J. M. Huber Corporation under the trademark Zeolex® and Hydrex®. Zeolex® products are sodium aluminosilicates, whereas Hydrex® products are magnesium aluminosilicates. They are generally synthesized at room temperature or slightly elevated temperatures by controlled addition of aluminum sulfate (or alum) solution to a solution of silicate while maintaining the pH between 9 and 12.[46] The precipitated aluminosilicate particles are then separated via filtration or centrifugation and purified by repeated washing. They often contain co-precipitated sulfate (~ 5%) according to the literature supplied by the manufacturers.

Precipitated aluminosilicates exhibit a wide range of characteristics like high structure (the extent to which aggregates form complex three-dimensional entities is often referred as a "structure"), high surface areas (~ 60 – 125 m^2/g), high refractive index, high whiteness, low abrasivity, and interesting light scattering and ultraviolet (UV) reflecting properties. As a result of these properties, precipitated aluminosilicates are used as reinforcing fillers in all types of elastomeric products, fillers in non-black or colored rubber articles, fillers in paper and printing industry, titanium dioxide extender in flat white paints, UV protector, and surface smoothers of hoses, gaskets and flooring materials. In fact, precipitated aluminosilicates are the first synthetic non-black filler. For reinforcement applications, typical loading of precipitated aluminosilicate range from a low 10 phr (parts per hundred pounds of resin) to a high 150 phr.[43b]

1.6. Similarities Between Zeolites and Geopolymers

The link between geopolymers and zeolites has been suggested by numerous studies. It has been shown that there are common nanostructural features between geopolymer gels and zeolites, but the former lacks long-range crystalline order. Atomic level ordering in geopolymer gels has been demonstrated by using ^{29}Si MAS NMR studies on Na and K geopolymers by Rowles et al.[16, 47] Whereas, more recently, Bell et al. disclosed that the structural ordering in Cs geopolymer is similar to pollucite, a zeolite mineral, up to a length scale of one nm by employing X-ray pair distribution function (PDF) analysis based on synchrotron X-ray scattering data.[17a] However, similar X-ray PDF investigations on Na and K geopolymers by the same authors proved less fruitful, which according to the authors is due to the lower X-ray contrast produced by these systems compared to Cs system. Furthermore, visible evidence of the presence of nanocrystalline zeolites (~5 nm) in geopolymer samples prepared under certain conditions has been revealed by various authors via high-resolution electron microscopic (HRTEM) studies.[48] In a review article by Provis et al. such zeolitic units in the nanostructure of the disordered geopolymer gel are discussed in detail.[17b] The same authors proposed that the X-ray amorphous geopolymer gels may contain nanocrystalline zeolites compacted in an amorphous gel phase. Although ambiguously, they also summarized the compositions and physicochemical conditions suitable for the formation of such phases.

In terms of physicochemical conditions, much analogy are drawn between the synthesis of geopolymers and low silica zeolites for examples, both require high pH alkali solutions and both undergo a series of dissolution-reorientation-solidification

reactions under hydrothermal conditions. The term hydrothermal is used rather loosely and includes the crystallization of zeolites from aqueous solutions at temperatures between 80 – 250 °C, and geopolymers are formed below 80 °C, while the pressures are autogenous meaning the saturated vapor pressures at the designated temperatures.[20] The two most important factors that govern whether or not X-ray diffracting crystals will form during geopolymerization are: 1) amount of water (expressed as mole fraction, x_{H_2O}), and 2) heating (or curing) temperature. Zeolites are the preferred products in the samples synthesized with large amount of water (X_{H_2O} greater than ~0.73) and higher temperatures (≥80 °C). For instance, a variety of low silica zeolites including zeolite X (FAU), sodalite (SOD), Linde A type (LTA), gismondite (GIS) and chabasite (CHA) have been prepared by reacting metakaolinite with solution of alkalis even before the introduction of geopolymers or the geopolymerization process.[49] These zeolites were prepared using solutions containing $x_{H_2O} > 0.84$ at temperatures ≥ 80 °C over a period of 7 days.

The additional factors that dictate the formation of zeolitic phases during geopolymerization, although less distinctively, are: heating time, Si/Al and Na/Al ratios, and the type of alkali. Specifically, even the low water content compositions, when heated (cured) for extended periods under moist conditions or after a brief period at elevated temperatures are known to form zeolite structures to a certain extent (may or may not be detected by XRD analysis), particularly in low Si/Al (≈ 1) ratio samples. In one example, using HRTEM, Bell et al. observed the formation of nanocrystals (6 – 10 nm) of Linde A type (LTA) zeolite from the composition $2SiO_2$:Al_2O_3:Na_2O with x_{H_2O} = 0.62 when heated at 50 °C for 48 h. Using synchrotron XRD data and pattern fitting

analysis, they were able to quantify the amount of LTA to be ~4% with the rest existing as an amorphous phase. They concluded that the concentrated nature of geopolymer gels permitted only a small amount of zeolite crystallization.[48] On the contrary, Rowles et al. observed the formation of zeolite X (~44 %, as quantified by ^{29}Si MAS NMR) from the similar composition with even lower amount of water (X_{H_2O} = 0.60) when heated at 70 °C for 24 h signifying the temperature effect. One common feature of both the studies is that the metakaolin was activated with alkali hydroxide with no soluble silicate (Si/Al = 1). Furthermore, Duxson et al. demonstrated that the presence of soluble silica in the activating solution hinders the formation of zeolitic structures.[50] By systematically increasing the amount of silica in the KOH activating solution from 0 – 0.5 (i.e., total Si/Al ratio from 1.0 – 1.5) in the samples prepared by activating metakaolin at 120 °C for 24 h, they showed that although the specimens synthesized using the highest levels of soluble silicon appear amorphous to XRD, specimens synthesized with small amounts of soluble silicon (Si/Al $\leq$ 1.25) exhibit peaks due to zeolitic phases. Addition of soluble silicon to the activating solutions used in the synthesis of geopolymers can be observed to substantially reduce the level of long-range structural ordering with increasing concentration, but does not appear to fundamentally change the reaction mechanism.

Additionally, Duxson et al. also remarked that the aluminosilicate gel formed depends not only on the concentration of the added soluble silica, it also depends on its degree of polymerization, which in turn is influenced by the ratio of Na/Al (equivalent to NaOH/Si ratio). Silicate solutions with higher Na/Al ratio have a lower degree of polymerization of soluble silica and lead to geopolymers with a higher level of long-range ordering. Zeolite formation is also known to occur in KOH activated metakaolin

(KOH/metakaolin) systems but crystallization is less rapid compared to the NaOH/metakaolin systems.[41] Moreover, the presence of Ca is recognized to suppress the formation of zeolitic phases. These physicochemical conditions that favor the formation of geopolymers versus zeolites are summarized in **Table 1**, although not precisely due to the lack of distinct boundaries in what is already a very complex system.

Table 1. Synthetic parameters that dictate the formation of geopolymers versus zeolites from the geopolymerization process.

Synthetic Parameters	Favorable Conditions for the Formation of	
	Geopolymers	Zeolitic Phases
Water content (X_{H_2O})	Low (< ~0.73)	High (> 0.76)
Temperature	Low (25 – 80 °C)	High (80 – 250 °C)
Alkali content (A/Al)[a]	Low (≈ 1)	High (>1)
Curing time	Low (several hours)	High (several days)[b]
Activating solution	Alkali silicate (presence of soluble silica)	Alkali hydroxide[c] (no to little soluble silica)

[a]A is an alkali cation (Na, K or Ca)
[b]Under humid conditions
[c]The rate of formation of zeolite from the hydroxide of Na<K<<Ca

As a result of this obvious relationship between geopolymers and zeolites, Kriven et al. suggested that the geopolymers are metastable, kinetic products which over time will convert into zeolites.[51] Furthermore, zeolites themselves are known to undergo transformations into the related stable phases such as of feldspars, the ultimate aluminosilicate products, as shown schematically in **Figure 8**.[52]

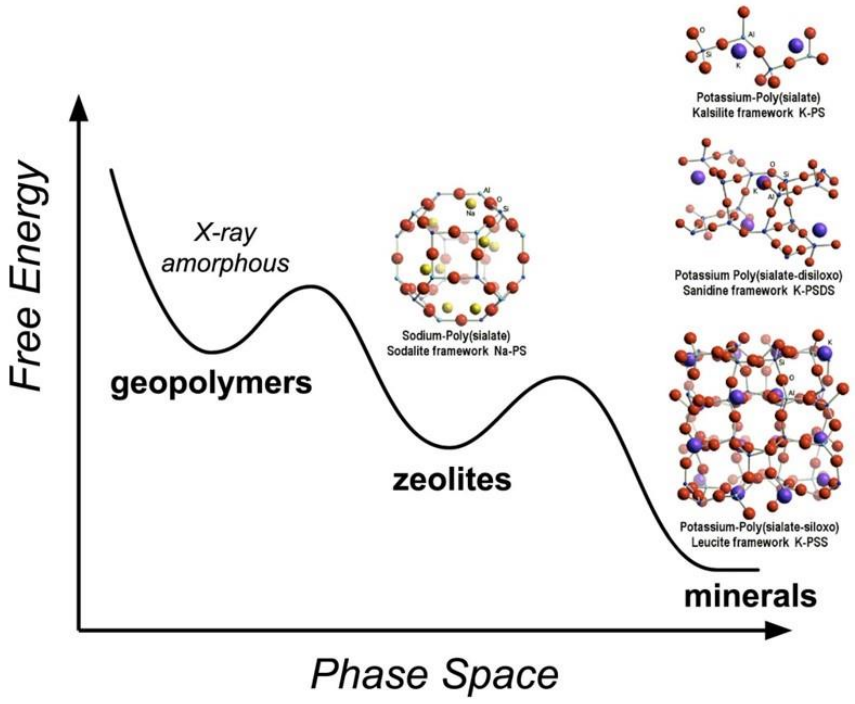

Figure 8. Free energy diagram of chemically related aluminosilicates, adapted from Kriven et al.[27]

1.7. Recent Trends in Zeolites and Geopolymers

The steady interest in porous solids is due to the potential of these materials to offer sustainable solutions to global issues such as increasing energy demands and concurrently meet more stringent environmental standards for industrial pollutants, depletion of resources, and health improvement. According to the International Union of Pure and Applied Chemistry (IUPAC), solids containing pores whose widths are less than 2 nm are classified as microporous materials, whereas solids having pores widths between 2 – 50 nm are categorized as mesoporous materials, and those enclosing pores wider than 50 nm are termed macroporous materials.[53] The porous materials that are considered in this thesis are zeolites and geopolymers. Zeolites are inherently

microporous whereas geopolymers are generally considered nanoporous but the internal surfaces of the pores present in them are generally not accessible by the external molecules.

Recently, over the past decade or so, much efforts are being dedicated to prepare zeolites with enhanced accessibility to their micropores. Zeolites already found their way into a multitude of fields such as catalysis, adsorption, separation and purification, ion-exchange, building materials, and cosmetics to name a few.[54] Most, if not all of these applications are dictated by how fast the external molecules can diffuse in and out of the zeolite crystals which are typically micron sized.[55] Limited diffusion through micropores not only hinders the complete utilization of the zeolitic crystals but also generate undesired byproducts in the case of catalysis.[56] The main strategy to improve the diffusion through the narrower micropores is to decrease the average diffusion path lengths. Theoretically, intracrystalline diffusion time decreases quadratically with decreasing the particle size (i.e. diffusion path length). The diffusion path lengths can be decreased by creating hierarchical pore systems i.e. systems containing pores of at least one bigger length scale (meso and/or macropores) in addition to the inherently present micropores in zeolites. Ideally, the bigger pores should run from the outside to the inside of a zeolite crystal and lead into the micropores.

Zeolites with hierarchical pore systems include: 1) micron sized zeolites with intracrystalline meso and/or macropores, 2) zeolite composites where the support material provides meso and/or macropores, and 3) self-assembled structures of nanozeolites where the aggregation of nanocrystals create intercrystalline meso and/or macropores. Intracrystalline meso and/or macropores can be introduced by employing

templating methods (hard or soft templates)[57] in a bottom-up fashion or non-templating methods (demetallation from preformed zeolite crystals) via a top-down approach, whereas intercrystalline meso and/or macropores can be introduced by controlled crystallization of nanozeolites following a bottom-up methodology.[55, 58] At present, very elegant templating methods with precise pore size control exist but are too expensive to be realized industrially due to the high cost of templates and also due to the additional cost and environmental impact involved in burning the templates. Selective demetallation, a non-templating and post synthetic method is very promising industrially and its applicability towards many zeolite frameworks with Si/Al $\geq$ 4 is shown by strategically chosen dealumination or desilication (in the presence of pore-growth moderators such as tetrapropylammonium (TPA^+) cations) or sequence of both processes.[59] Recently, carefully selected sequence of mild dealumination followed by alkaline treatment and subsequent mild acid wash was developed to introduce mesoporosity into FAU-type zeolites with Si/Al as low as 2.4.[60] More recently, mild acid washing with Na_2H_2EDTA was developed to introduce mesopores into even aluminum rich zeolites such as Zeolite X and A (both in NH_4 form only, with a Si/Al = 1.2) completing the applicability of demetallation to zeolites with almost entire range of Si/Al ratios.[61] Controlled crystallization without using expensive templates/surfactants to obtain nanozeolites with intercrystalline meso and/or macropores is also a promising methodology to produce low silica zeolites with improved diffusion. Considering the huge interest in hierarchical zeolites in academia and industry alike, it is predicted that many new elegant synthetic approaches will be added to the already existing collection of methods.

Geopolymers are promising engineered materials which are being increasingly studied as a more environment-friendly alternative to Portland cement in construction due to their large-scale availability, excellent thermal stability and superior mechanical properties. As mentioned in section 1.4, geopolymers are inherent nanomaterials with a xerogel-like microstructure made up of highly fused nanoparticles whose diameters are in the range of 10 – 30 nm. The dense nature of the geopolymer microstructure narrows the pore channels in the xerogel-like structure, preventing effective molecular flow, as evidenced from the ill-shaped hysteresis loops in gas sorption isotherms.

Nevertheless, over the past five years, new research efforts have been geared toward utilizing the geopolymers for nontraditional applications, such as evaporative cooling, drug delivery, ion exchange, and catalysis, mainly by taking advantage of the innate nanostructure of geopolymers. For instances, by employing much high water amounts (72 – 82 wt% as opposed to a typical ~45 wt%) in synthesis, more open geopolymer pore structures have been reported recently by Forsgren et al.,[62] and Jämstorp et al.[63] These studies reported that the porosity and average pore size can be tuned by the changing the water content in the synthesis. Furthermore, drug permeation and release rates could also be adjusted according to the requirements. Although, the increased porosity and pore sizes with water content had an adverse effect on the compressive strength of these materials, it was sufficient for such drug delivery applications. In a separate study by Cai et al., resistance of drug loaded geopolymers for common tampering practices were evaluated and compared to the marketed controlled-release tablets. They found the geopolymer matrix to have increased resistance to such common tampering practices and therefore proposed geopolymers as a potential material for

reducing drug abuse.[64] While Okada et al. have shown porous geopolymers with specific compositions to have suitable water release and consequent evaporative cooling properties for the remediation of "heat island effect" (which is defined as the phenomenon of urban areas having higher temperatures compared to their surrounding rural areas).[65]

In terms of ion-exchange capability, O'Connor et al. demonstrated that the the Na^+ ions in a conventional Na-geopolymer can be completely exchanged by K^+, Ag^+, NH_4^+ and Pb^{2+} ions while a partial exchange can be achieved by Li^+ (82%), Cd^{2+} (78%) and Mg^{2+} (57%). Geopolymers exchanged with K^+, Li^+ and NH_4^+ were proven to be suitable precursors for crystalline ceramics, forming leucite, spodumene and mullite respectively, upon heating at 1100 °C. They also showed the Ag^+ exchanged compound was a powerful antimicrobial agent against Staphylococcus aureus. Moreover, they also suggested that NH_4^+ ion in the NH_4^+-exchanged geopolymer decomposes when heated at 600 °C and therefore may be a potential solid acid catalyst for organic reactions such as the Friedel–Crafts alkylation. Furthermore, based on the efficient exchange by Pb^{2+} and Cd^{2+}, they also highlighted the potential of Na-geopolymer for the cost-effective removal of heavy metal ions from wastewater streams.[66] Additionally, Taya from our group demonstrated ion exchange of K^+ ions from high surface area porous geopolymer (K-geopolymer) by Na^+ (77%) and Cs^+ (61%) ions.[67]

In another recent study by Sazama et. al., modified geopolymers have been shown to be a promising heterogeneous catalyst for selective reduction of nitrogen oxides by ammonia and the total oxidation of volatile hydrocarbons. Catalytic sites were generated by modifying Na-based or K/Ca-based geopolymer through an ion exchange process

using aqueous solutions of transition metal ions including Fe^{3+}, Co^{2+}, Cu^{2+} and Pt^{2+}.[68] In similar synthetic approaches in which conventional geopolymer is employed as a starting material, photocatalytic activities have been realized in Ni^{2+}-ion exchanged geopolymer and TiO_2-containing geopolymer.[69] More recently, our group has successfully prepared a new class of high-surface area solid base catalysts by modifying the hierarchically porous geopolymer with calcium. These novel catalysts were demonstrated to be highly active for the conversion of soybean oil to biodiesel with good recyclability emphasising their potential for cost-effective biodiesel production.[70]

Although geopolymer chemistry is quite complex, recent progress points to ever-greater research efforts for discovering yet-to-be explored applications for this unique and versatile material. Moreover, it is anticipated that improved insights into the geopolymerization process will appear during the coming years. The new efforts will lead to a significant improvement in our understanding of geopolymers and possibly also to a momentous technological developments through their implementation in industrial applications.

1.8. Current Work

The work presented in this thesis outlines the preparation of three new nanostructured aluminosilicate materials, namely: geopolymers with hierarchically meso/macroporous structures, dispersible geopolymer particles, and highly crystalline hierarchical zeolites, all produced by modifying the geopolymerization process in ways that are readily scalable and cost-effective.

The limitations of the existing geopolymer technology described previously are:

1) Lack of synthetic procedures to introduce interconnected pores within the geopolymer monoliths other than merely increasing the amount of water used in the synthesis.
2) Nonexistent techniques (particularly bottom-up) to produce geopolymeric products in the powder form.
3) Dearth of methods in producing highly crystalline zeolites from the geopolymerization process, although the presence of zeolitic phases with varying degree of crystallinity in the geopolymer products has been well-recognized – even from the early days of geopolymer technology.

The work described in this thesis addresses the aforementioned problems of the contemporary geopolymer technology in the following ways:

1) A new synthetic procedure is presented in order to introduce interconnected, hierarchical meso-/macropores into the geopolymer products by developing a reactive emulsion templating method with triglyceride oil.
2) For the first time, it is made possible to produce geopolymeric products in the powder form through a bottom-up approach. This was achieved by activating metakaolin with sodium silicate solutions containing excess alkali, and curing for short duration under moist conditions.
3) Likewise, a preparation method to make highly crystalline, hierarchical faujasite zeolites from the geopolymerization process is demonstrated for the first time. This was accomplished by sodium silicate activation of metakaolin

in the presence of excess alkali, in combination with the reactive emulsion templating with triglyceride oil.

In addition to describing the newly developed synthetic procedures to expand the geopolymer technology, this thesis also discusses the performance of some of the produced novel materials towards the tested applications. Particularly, iron oxide modified nanoporous geopolymers are assessed for the removal of arsenic from contaminated water, and highly crystalline hierarchical faujasite zeolites are evaluated for carbon dioxide sorption properties in the context of several industrially relevant CO_2 separation applications.

CHAPTER 2

2. CHARACTERIZATION TECHNIQUES AND EXPERIMENTAL METHODS

2.1. Introduction

To further the understanding of the syntheses proposed and the final materials produced in this thesis, a wide range of characterization techniques have been used. Powder X-ray diffraction (PXRD) was used for identification and characterization of geopolymers and zeolites at various stages in their synthesis, and also to determine the crystallite sizes. Gas sorption studies, i.e. N_2 adsorption and desorption studies at 77 K, were used to evaluate the pore properties, namely surface area, pore volume and pore widths. Electron microscopy, i.e. scanning electron microscopy (SEM) and transmission electron microscopy (TEM) were used to investigate the macro and microscopic structural properties. Dynamic light scattering (DLS) was used to identify the hydrodynamic radii of the particles. This chapter is divided into individual characterization techniques, for which the theory and applications specific for this work are reviewed to assist the discussion and results in the proceeding chapters.

2.2. Powder X-ray Diffraction (PXRD)

X-ray diffraction is a rapid and non-destructive analytical technique used for determining the atomic structure of a crystalline material which also provides information on crystallite size. In crystalline materials, atoms are arranged in regular, systematic and repeating manner throughout the crystal in all three dimensions of space. Due to the fact that atoms contain electrons which are able to absorb and re-emit electromagnetic

radiation in directions not necessarily equal to the incident direction, atoms can act as light scatterers. The interference of the scattered light leads to the general phenomena of diffraction. Fundamentally, diffraction is a phenomenon that is observed when electromagnetic radiation impinges on periodic structures with geometric variations on the length scale of the wavelength of the radiation. The interatomic distances in crystals and molecules are found to be in the range of 1 – 4 Å, so X-rays with a wavelength ranging between 0.5 – 2.5 Å are a suitable radiation for observing diffraction in crystals.[71]

Max van Laue, in 1912, discovered that crystalline samples can act as diffraction gratings for X-rays. X-ray diffraction is now a common tool to study the atomic structure in crystalline materials. X-ray diffraction is based on constructive interference of monochromatic X-rays diffracted from a given diffracting plane. For an infinite row of scatterers, such as in perfect crystals, the only condition at which constructive interference will occur and a reflection will be observed is when the Bragg law condition is met.[72] Bragg's law states that when monochromatic X-rays are incident onto a crystal with parallel diffracting planes, their angle of incidence (θ) is same as the angle of scattering (θ). Furtheremore, when the path difference, d, between the diffracted X-rays is equal to a whole number, n, of wavelength, a constructive interference will occur (**Figure 9**). Bragg explained this in the form of an equation now known as Bragg's law:

$$2d \cdot sin\theta = n\lambda \qquad (1)$$

The collected diffraction pattern contains peaks called Bragg peaks, that are directly correlated to atomic distances from which crystal structure can be determined. Under all other conditions, the scattering is annihilated due to destructive interference.

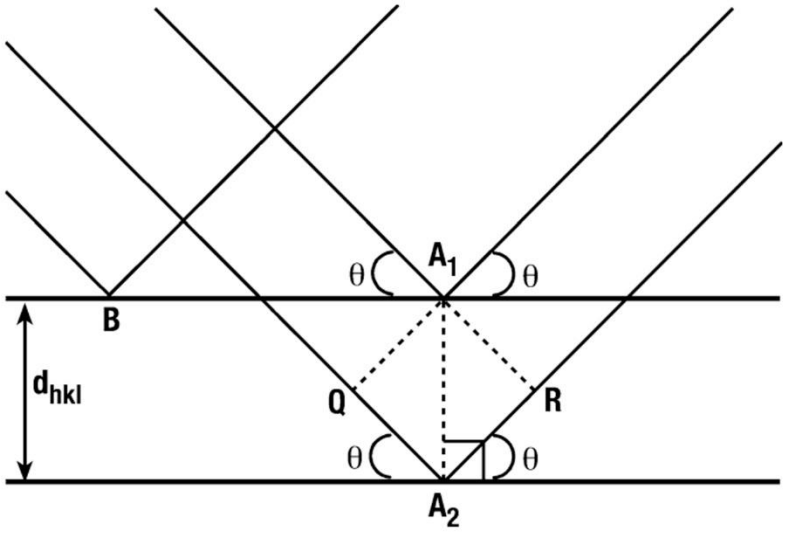

Figure 9. Diffraction of two parallel planes. Constructive interference occurs when the path difference (i.e., $QA_2 + A_2R = 2d_{hkl}\sin\theta$) of the reflected waves is equal to an integral number of wavelengths, adapted from Chester.[73]

Powder X-ray diffraction is one of the most important, powerful and widely used non-destructive analytical technique for the study of solid state materials. Many materials, especially zeolites, can be synthesized only in the form of polycrystalline powders and are not amenable to single crystal XRD measurements. In the example of zeolites, crystalline dimensions of zeolite samples are typically smaller than 10 μm, for example. Moreover, for most crystalline samples of industrial importance, the bulk properties of a powder or a polycrystalline solid, averaged throughout the sample, are required rather than a single crystal data, which becomes important for determination of the crystal structure or for studying some other fundamental physical property. Powder diffraction is diffraction of light by powders or microcrystalline samples, where ideally every crystalline orientation is represented equally. The resulting orientation averaging

causes the three dimensional reciprocal space to be projected on a single dimension. The diffractogram or diffraction pattern is a unique "fingerprint" of materials. Phase identification is performed by comparing the diffraction patterns to the known standard sample or to databases. A perfect crystal would extend in all three dimensions to infinity but due to the finite size of the actual crystals no crystal can be defined as perfect. Such an imperfection is noticed to lead to broadening of the diffraction peak. Nevertheless, this type of peak broadening has been observed to be negligible when the crystallite size is larger than 200 nm (2×10^{-7} m). Crystallite size of a nanocrystalline bulk material is an average measure of the size of a coherently diffracting domain that can be calculated by using the Scherrer's equation:

$$t = \frac{K\lambda}{B \cdot \cos\theta} \qquad (2)$$

which relates the average dimension of the crystallites (t) to the width (B = Full-Width at Half-Maximum (FWHM)) of the diffraction peak (in radians) observed at 2θ. K is the Scherrer's constant, somewhat arbitrary value between 0.87 – 1.0 but usually 1 assuming spherical particles[74] and λ is the wavelength of the X-rays (1.5418 Å in the case of Cu-K_α radiation).[75] The smallest crystallite size that can be calculated with reasonable confidence using this equation is around 10 nm, where a typical diffraction maximum is not possible and the background signal has a substantial presence in the broad diffraction peak of the nanocrystallite.

Different materials can exhibit different degrees of crystallinity and therefore give different powder X-ray diffraction patterns. Amorphous materials with no long range ordering give no diffraction at all, large crystals give patterns with sharper and intense

peaks and materials of intermediate crystallinity give diffraction patterns with broad peaks. This range of phases can be represented by various types of aluminosilicates prepared under different synthetic conditions. Diffraction pattern of metakaolin or calcined kaolin, the precursor used for geopolymerization in this study gives a broad amorphous peak at ~22° 2θ in Cu-K_α XRD. It has been well documented that this peak at ~22° is replaced by a new 'amorphous hump' centered at ~28–30° 2θ upon activation with alkaline silicate solution suggesting that the bonding environment changes during geopolymerization. This new broad hump centered at ~28–30° 2θ is considered to be the distinguishing feature of the diffraction pattern of any geopolymer irrespective of the choice of solid aluminosilicate source (metakaolin, fly ash or blast furnace slag), activating solution (sodium or potassium hydroxide with or without dissolved silicate) and curing conditions. Rowles and O'Connor observed that partially activated compositions which had significant amount of unreacted metakaolin within the geopolymeric matrix exhibited a diffraction pattern with the ~22° peak superimposed with ~28° peak [76]. Therefore, although amorphous, depending upon the position of the hump, power X-ray diffraction is capable of 1) identifying the nanostructure of geopolymer and 2) revealing the extent of geopolymerization that has occurred. Moreover, by taking peak-broadening effects of small crystals into the account, Provis et al. argued that this amorphous hump is due to the presence of zeolite nanocrystals on a length scale below the detection limits of XRD.[17b] Yang et al. attributed this hump at ~28° to the presence of a phase they called 'precrystallization' with zeolites present on a length scale of no more than 4 unit cells, or approximately 8 – 10 nm.[77] On the contrary, pure crystalline zeolites with micron sized crystals containing many unit cells produces

X-ray diffraction patterns with many diffraction lines. Nanozeolites whose size range between 20 – 100 nm with approximately 8 – 42 unit cells (assuming FAU (faujasite) structure), on the other hand, produce diffraction patterns with many diffraction lines that are broadened significantly. The crystallite size of such nanozeolites can be calculated using the Scherrer's equation applied to the broadened reflections. For example, average crystallite size of nanocrystalline FAU (zeolite X or Y) can be calculated from the reflections at a 2θ value of 6° (111), 16° (331) and 27° (642).[78]

2.3. Gas Sorption Studies

Adsorption and desorption of gas molecules on the surface of a porous material provides vital information about the surface area, pore volume and pore size distribution (PSD). The basis for sorption measurements is physisorption of gas molecules on the surface. Physisorption is a van der Waals type of interaction (dispersion or dipolar) between the adsorbate (gas molecules) and the adsorbent (porous material). These interactions are weak, on the order of 20 $kJ \cdot mol^{-1}$, so the adsorbate molecules easily adsorb and desorb from the surface of the adsorbent, and the surface coverage increases at lower temperatures.

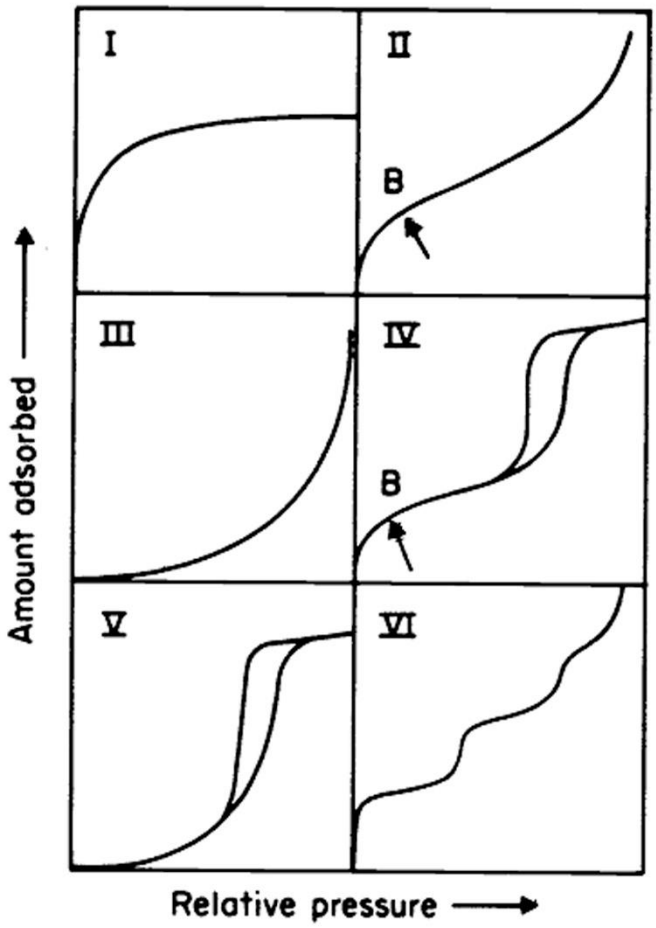

Figure 10. Types of physisorption isotherms, adapted from Sing.[79]

Essentially, when a solid is exposed in a closed space to a known amount of gas at pressure P, the weight of the solid characteristically increases and the pressure of the gas decreases i.e. the gas is adsorbed by the solid. After certain time, the pressure P does not change any more and correspondingly the weight of the solid stops to increase any further, at which point a dynamic equilibrium has been established. The amount of gas adsorbed is experimentally determined by monitoring the fall in the gas pressure (volumetry) or increase in the solid weight (gravimetry). A series of measurements at different pressures and constant temperature are collected and composed into a data set

called an isotherm. When possible, the solid samples are finely ground in order to minimize the time taken to achieve equilibrium pressures. Typically, pressure is varied from vacuum to 1 bar at liquid N_2 temperature, 77 K. The pressure is properly normalized to the saturation vapor pressure P_o and the adsorbed amounts are so referred to the dimensionless relative pressure P/P_o. Physisorption isotherms are currently classified in six classes (I – VI) according to the IUPAC classification, as shown in **Figure 10**. The presence of pores of different dimensions can be differentiated from the shape of the isotherms.[79]

The recorded values are generally interpreted relying on various models. For surface area measurements, a BET equation, developed by Brunauer, Emmett and Teller is a commonly used model:

$$\frac{P}{V(P-P_o)} = \frac{1}{V_m c} + \frac{c-1}{V_m c} \cdot \frac{P}{P_o} \qquad (3)$$

where V is the volume adsorbed, V_m is volume of monolayer, P and P_0 are equilibrium and saturation pressures, and c is a constant (BET constant) related to the enthalpy of adsorption. The specific surface area (S_{BET}) is then calculated from V_m by the following equation:

$$S_{BET} = \frac{V_m \cdot n_a \cdot a_m}{m \cdot V_L} \qquad (4)$$

where n_a is Avogadro constant, a_m is the cross sectional area occupied by each nitrogen molecule (0.162 nm^2), m is the weight of the sample, and V_L is the molar volume of nitrogen gas (22,414 cm^3).

The 't-plot' method is commonly used to estimate the pore volume and specific surface area of microporous materials like zeolites by comparing the isotherms of

samples under investigation with those of reference samples. The multilayer film thickness of adsorbate (t-values) is evaluated on a reference nonporous solid with similar surface properties to the samples under investigation. Alternatively, standard reference plots like the one obtained from Harkins and Jura equation for silica and alumina substrates can be used:

$$t\ (nm) = 0.1 \left[\frac{13.99}{0.034 - \log\left(P/P_o\right)}\right]^{1/2} \qquad (5)$$

The volume adsorbed on the sample under investigation at different pressures is plotted against 't' and the corresponding statistical average layer thickness is calculated from the standard isotherm obtained with a nonporous reference solid. A straight line passing through the origin is obtained for nonporous materials. Variation in the intercept value and deviation in shape of the 't-plot' from linearity indicates the presence of pores of a definite size. This way, micropore volume and surface areas can be calculated. Difference in surface areas obtained from BET equation and 't-plot' method gives external surface area.[80]

The total pore volume is calculated by measuring the volume of N_2 adsorbed at $P/P_o \approx 1.0$. Mesopore volume is then obtained by calculating the difference in total pore volume and micropore volume obtained from the 't-plot' method. The distribution of pore volumes with respect to the pore widths is called a pore size distribution (PSD). To determine PSD, the pore geometry, such as cylindrical, spherical or slit shape, is taken into account. A Model of Barrett, Joyner, and Halenda (BJH model) for PSD measurements assumes a cylindrical pore system. The BJH model assumes that

condensation of adsorbate in pores of smaller widths occurs at lower partial pressures and larger pores are filled at higher partial pressures. On the contrary, adsorbate desorbs from pores of larger diameter as the partial pressure decreases. A representative nitrogen sorption isotherm is shown in **Figure 11**.

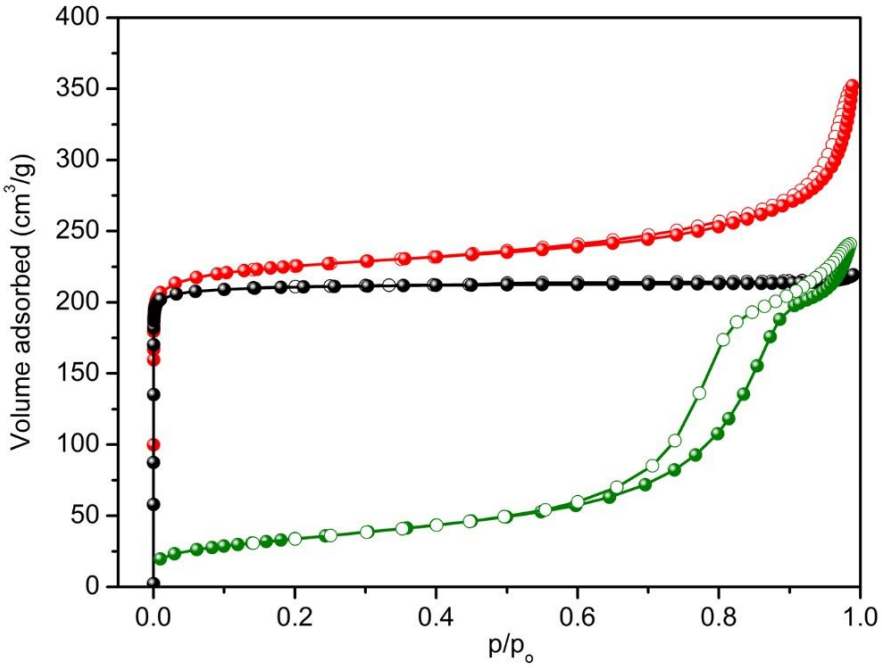

Figure 11. Typical nitrogen isotherms of a material containing only microporous (black), only mesopores (olive), and a combination of both micropores and mesopores (red).

2.4. Electron Microscopy

Electron microscopy, as the name suggests, uses electrons as an illumination source rather than light in the case of light microscope. The spatial resolution of an illuminating source is proportional to its wavelength, and thus the spatial resolution limit of an optical microscope, whose shortest possible wavelength is about 400 nm, is set at

about 0.2 μm.[73] However, after de Broglie (in mid-1920's) hypothesized that electrons exist as waves with wavelengths on the order of tens of angstroms, much research has been dedicated in developing microscopes with electrons as an illuminating source which possibly can reach a resolution of few angstroms.[81] Within a decade, Knoll and Ruska constructed the first ever electron microscope, a transmission electron microscope (TEM). Since early electron microscopes were all TEM's which are built based on the concept of transmission light microscopes, there are much similarities between the two instruments. Both the instruments have illuminating source, lenses, a sample stage, a viewing port, and an image collecting setup. But the lenses in TEM are electromagnetic lenses unlike glass lenses in optical microscope, and TEM operates under high vacuum in contrary to an optical microscope which operates at ambient pressure. In mid-1930's Knoll also built an electron microscope called scanning electron microscope (SEM) which can scan a narrowly focused electron beam over the specimen to generate an image by collecting various signals produced at the surface of the specimen. Typically low energy secondary electrons (SE) generated from the top few nanometers of the specimen or high energy back scattered electrons (BSE) are used for imaging purposes under SEM. SEM is operated at slightly lower vacuum than a TEM and SEM can accommodate large specimens. Since the wavelength of an electron is inversely proportional to its momentum or acceleration voltage, TEM (typically ~ 60–500 kV) with higher acceleration voltage has smaller resolution than SEM (typically ~ 1–30 kV) (**Figure 12**).[81]

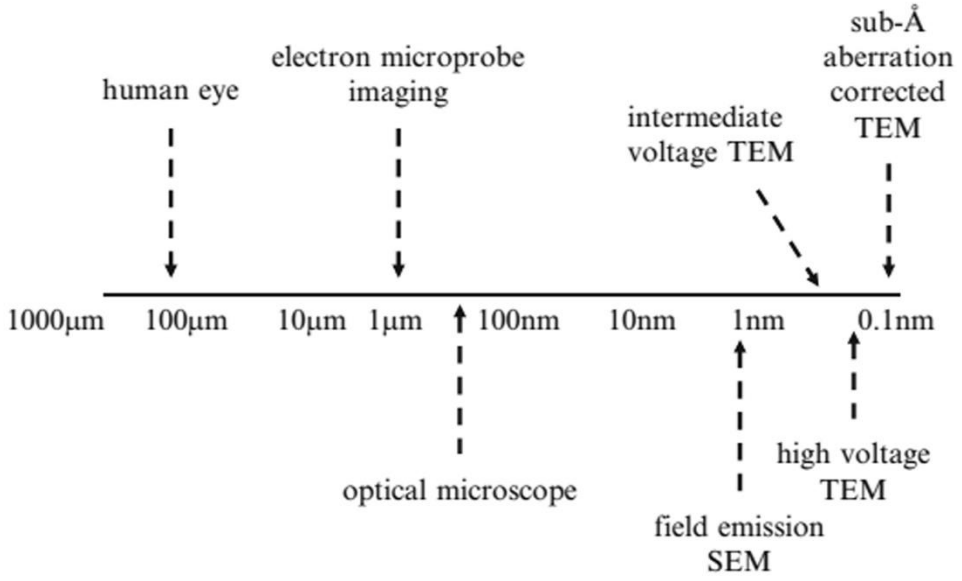

Figure 12. Increase in resolution from ~0.1 mm using the unaided human eye to sub-Å by means of aberration corrected TEM, adapted from Chester.[73]

In TEM the beam passes through the sample deposited on a thin metal grid (typically, copper grid) coated with a thin layer of carbon (usually, carbon film or lacey carbon) and reaches the detector. Samples to be viewed under TEM must be approximately 1000 Å or less in thickness in the area of interest so that sufficient electrons would be transmitted to form an image. The image collected in bright field imaging mode gives contrast information about the sample, in which darker areas in the image represent thicker areas or areas with higher atomic number and vice versa. A representative TEM image is shown in **Figure 13a & b**. If the samples are crystalline and are thin enough, lattice fringes may be visible as seen in **Figure 13b**. Lattice fringes can give information about the atomic structure of the sample. The lattice fringes are not direct images of the atomic structure but can reveal information about the lattice spacing

and atomic structure of a crystal. The choice of specimen support is important for high resolution TEM, since thicker support film decreases the resolution and may make lattice fringes difficult to detect. Good results are obtained using amorphous carbon films under 10 nm in thickness or carbon lacey films, where the nanocrystals can be suspended on a carbon "net" with little or no background interference.[82]

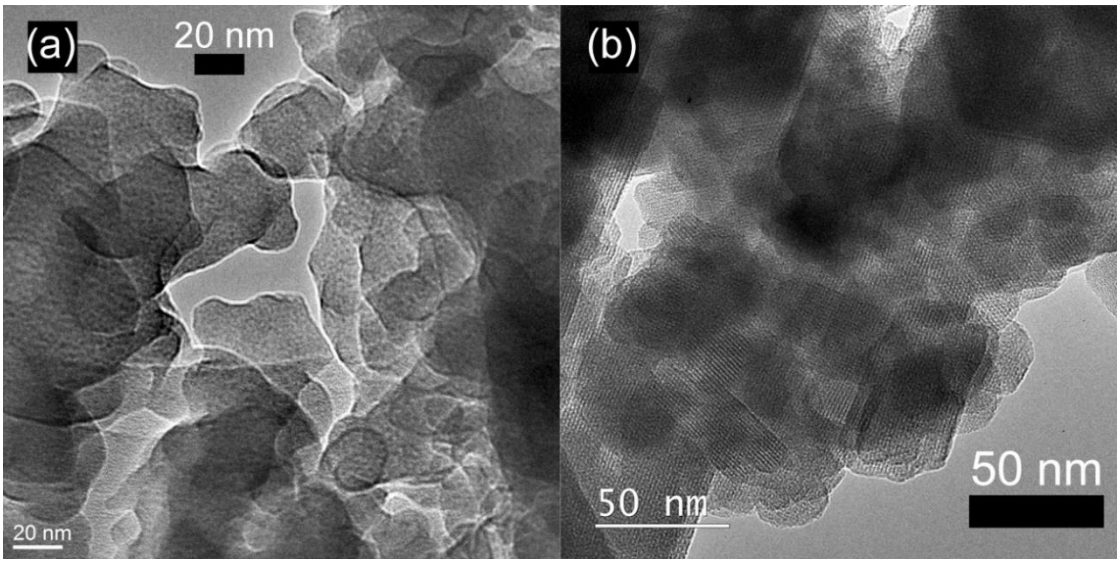

Figure 13. TEM images of amorphous geopolymer particles (a), and NaX-type hierarchical zeolite nano-crystals (b) chosen as representative samples. Both samples reveal darker and lighter areas signifying thick and thin regions, respectively, but only crystals within thin regions display lattice fringes.

It has been well documented in the literature that zeolites are susceptible to beam damage under TEM. The rate of beam damage has been observed to be dependent on the Si/Al ratio, on the size of cations[83] and on the extent of hydration.[84] The damage has been identified to be via two possible mechanism: knock-on damage – the atom in the specimen is knocked from its site by the incident electron, and radiolytic damage –

incident electron transfers energy to the electrons in the specimen resulting in bond breakage and consequently the possible alteration of the structure.[85] Knock-on damage can be decreased by increasing the energy of incident electrons, while radiolitic damage can be reduced by decreasing the incident beam energy. Therefore, it is very important to identify an intermediate beam energy (~100 – 120 kV) to minimize the rate of beam damage. Using dehydrated zeolite specimens also seems to lower the rate of beam damage.

Although various types of signals are generated in SEM, only two types, namely low energy secondary electrons (SE) emitted due to inelastic interactions and high energy back scattered electrons (BSE) emitted due to elastic interactions are used for imaging purposes. Since SE's are emitted only from the top few nanometers of the specimen, they produce images having three-dimensional nature and hence enables studying the topology and the morphology of the materials as shown in **Figure 14**. For example, faujasite type and Linde type-A zeolites have been shown to exhibit octahedral and cubic morphologies respectively by SEM.[86] Meanwhile since the aluminosilicates like geopolymers and zeolites are nonconductive and contains atoms with low atomic numbers, they may collect the charge gained from the electron beam and may result in artifacts in the image.[82] In order to avoid charging, nonconductive samples are sputter coated with a thin layer (several nanometers) of conductive material, such as gold or gold/palladium or platinum or chromium. The presence of clusters of conductive material on the sample surface may make the surface morphology investigations more difficult. Consequently the balance between the surface conductivity and the conductive film thickness becomes important. Additionally, sputter coated conductive materials tend

to cluster and form islands if stored for long duration of time. In practice, it is advised to sputter coat the specimens freshly i.e. at least on the same day of investigation under SEM.

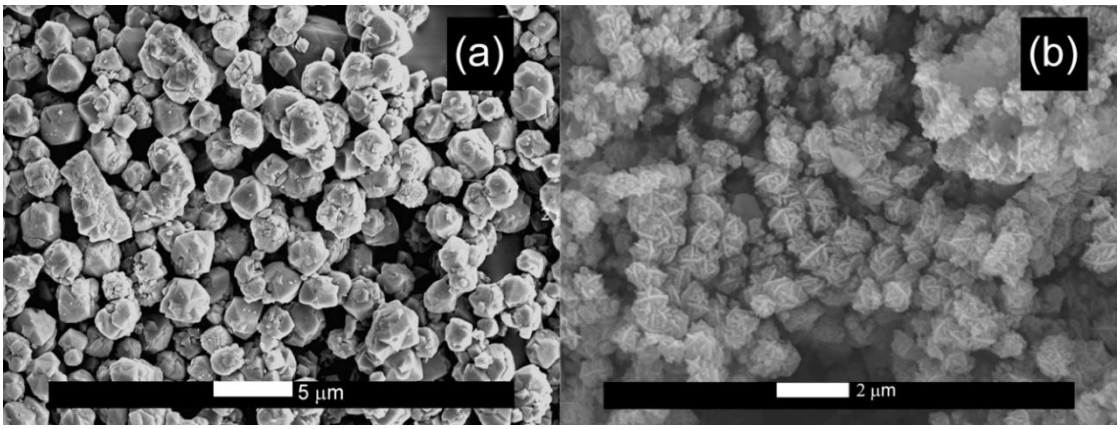

Figure 14. SEM images revealing the topology and morphology of zeolite 13X (a), and NaX-type hierarchical zeolite (b) chosen as representative samples.

2.5. Dynamic Light Scattering

Light scattering is a non-invasive and non-destructive technique used for characterizing numerous liquid dispersions. It is an absolute technique since external calibration standards are not required. Light scattering is used in many fields, from physics, chemistry, biology to medicine, food industry and pharmaceutical research – to study dispersions of particles and macromolecules.[87] Some of the systems frequently studied in both academia and industry are emulsions, micelles, liposomes, polymers, ceramic precursors, paints, and adhesives due to their fundamental and technological importance. Light scattering can be divided into two general categories, namely, static light scattering (SLS) and dynamic light scattering (DLS). In SLS, also known as

classical light scattering or multi-angle light scattering (MALS), the intensity of the scattered light is measured as a function of angle. This is often called Rayleigh scattering and can determine the molar mass, root mean square (rms) radius, and second virial coefficient of macromolecules. SLS was an established technique before DLS became possible during the sixties, with the advancements in laser technology. In DLS, also known as photon correlation spectroscopy (PCS) or quasi elastic light scattering (QELS), time-dependent fluctuations in the scattered light frequency or intensity are measured to infer diffusion coefficients and hence the hydrodynamic diameter of macromolecules or particles. Small particles have larger diffusion coefficients, and vice versa (**Figure 15**).

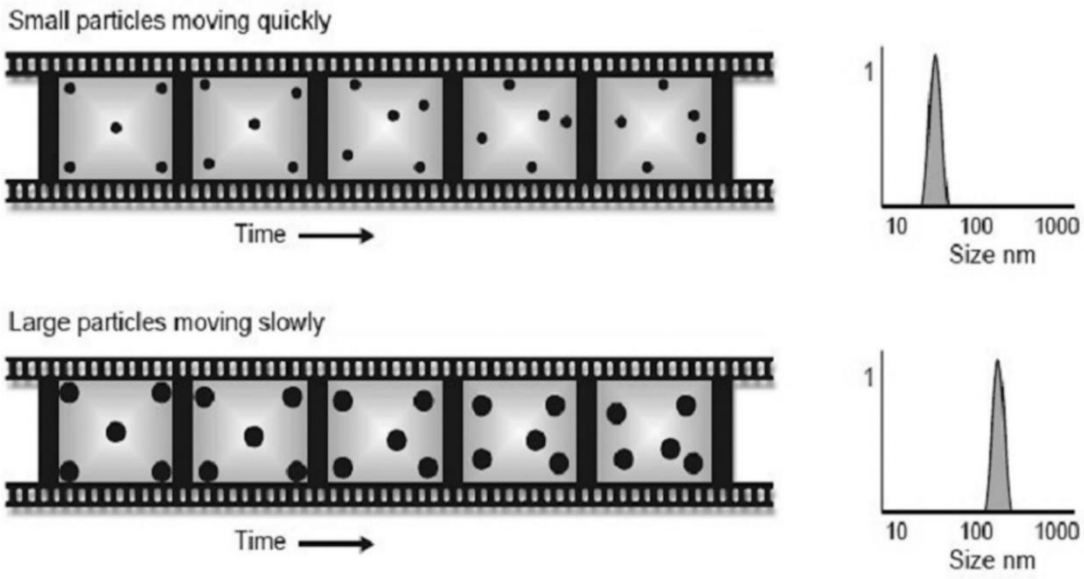

Figure 15. The particles in a liquid move about randomly and their motion speed is used to determine the size of the particles in DLS, adapted from Malvern.[88]

From an electromagnetic view point, light scattering is related to the movement of the scatterers (particles or macromolecules) suspended in a fluid, either liquid, or gas. The movement can be a random motion called Brownian motion or a uniform motion.

As light scatters from the moving scatterers, their motion imparts a randomness to the phase of the scattered light, such that when the scattered light from two or more particles is added together, there will be a fluctuating destructive or constructive interference. This leads to time-dependent fluctuations in the intensity of the scattered light. The fluctuations are directly related to the rate of diffusion of the scatterers through the dispersing medium. Therefore, the fluctuations can be analyzed to determine a hydrodynamic diameter for the sample. The fluctuations are quantified via a normalized second order correlation function given by:

$$g^{(2)}(\tau) = \frac{<I(t)I(t+\tau)>}{<I(t)>^2} \qquad (6)$$

where I(t) is the intensity of the scattered light at time t, and τ is the delay time. A liquid that does not have any scatterers produces a perfect correlation lacking any decay. If the particles are large the signal will change slowly and the correlation will persevere for a long time (**Figure 16**). If the particles are small and move rapidly then correlation reduces more quickly. A lot of information about the sample can also be inferred by looking at the correlogram. The time at which the correlation starts to substantially decay indicates the mean size of the sample. The gradient of the correlation indicates the polydispersity of the sample i.e., the steeper the line, the more mono disperse the sample is. Conversely, the more extended the decay becomes, the greater the sample polydispersity.

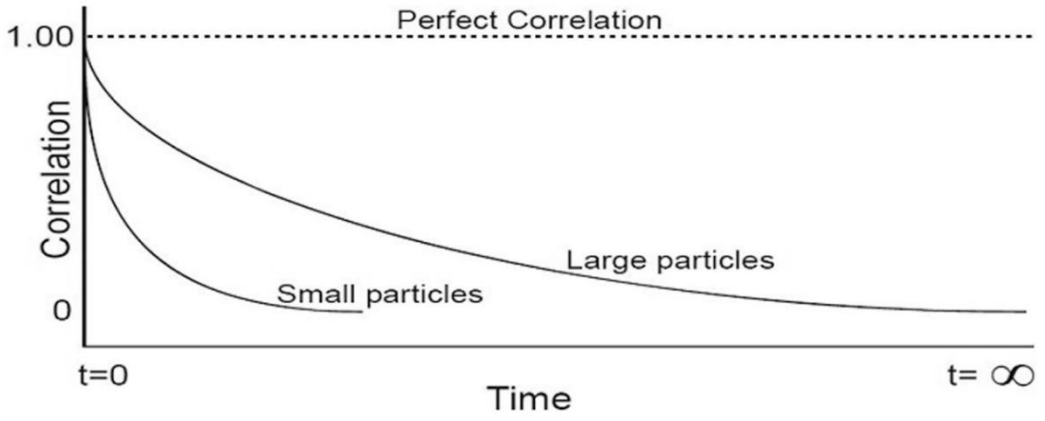

Figure 16. Typical correlogram from a sample, adapted from Malvern.[88]

The correlation function also contains diffusion coefficient information. The diffusion coefficient (D) is obtained by fitting the correlation function to an exponential function. Finally, the diffusion coefficient (D) can be interpreted as the hydrodynamic diameter (d_H) of a diffusing sphere via the Stokes-Einstein equation given by:

$$d_H = \frac{k_B T}{3\pi\eta D} \qquad (7)$$

where k_B is Boltzmann constant, T is absolute temperature, and η is viscosity. The DLS measurement principle requires that Brownian motion is the only cause of motion in the sample, i.e. effects of sedimentation, thermal convection and fluid flow have to be avoided. This usually limits the upper particle size that can be measured with DLS to a few micrometers. The lower size limit is determined by the time resolution of the specific measurement device and lies typically in the range of a few nanometers.[89]

2.6. Zeta Potential

Zeta potential analysis is a technique used to determine the surface charge of particles in solution (colloids). When oxide particles are suspended in a liquid medium

an electrical double layer is formed around them with one layer composed of ions tightly adsorbed on the surface of the particles called Stern layer. The other layer is composed of ions less firmly adsorbed called diffuse layer, as showed in **Figure 17**. This double layer of ions move with the particles as they diffuse throughout the solution (**Figure 17**). The boundary of the double layer is called a slipping plane (or surface of hydrodynamic shear) and the electric potential at this boundary is known as the zeta potential. Ions beyond the slipping plane stay with the bulk dispersant and do not move with the particles. The zeta potential of the colloidal particles typically range from +100 mV to -100 mV. Experience has shown that the stability of the colloidal systems can be correlated with this readily measurable experimental quantity. Colloidal dispersions with zeta potential values more positive than +30 mV or more negative than −30 mV typically have high degrees of stability.[90] Dispersions with a low zeta potential value are susceptible to Van Der Waal inter-particle attractions and will eventually aggregate and flocculate. Zeta potential is an important tool for understanding the state of the colloidal particle surface and predicting the long term stability of the colloids. A zeta potential value on its own without defining the solution conditions is essentially a meaningless number since it is greatly altered with a change in the pH of the suspension. A zeta potential versus pH curve will be positive at low pH and lower or negative at high pH. There may be a pH point where the plot passes through zero zeta potential. This point is called the isoelectric point and is often the point where the colloidal system is least stable and flocculate rapidly. Isoelectric point is a very important parameter from a practical perspective. In addition to the pH, zeta potential value is also very sensitive to the ionic strength of the medium and the concentration of the suspensions.

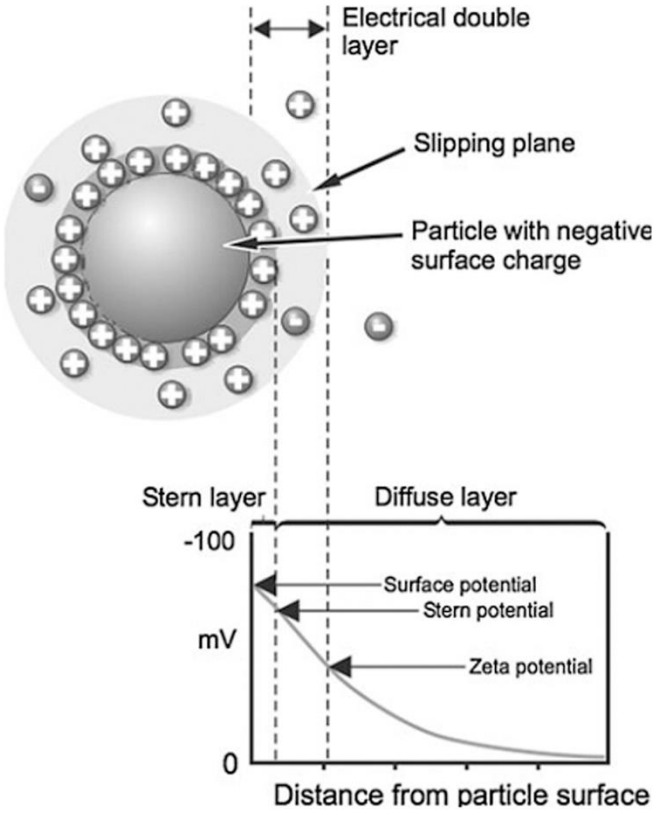

Figure 17. Schematic representation of a double layer that surrounds a negatively charged particle in an aqueous medium. The potential that exist at the slipping plane is known as the ζ-potential, adapted from Freire.[91]

The presence of electrical charges on the surface of particles cause them to interact with an applied electric field. These effects are collectively defined as electrokinetic effects. Depending on the way in which the particle motion is induced, these effects can be classified into four discrete categories, namely, electrophoresis, electroosmosis, streaming potential, and sedimentation potential. In electrophoresis, the movement of a charged particle relative to the liquid it is dispersed in under the influence of an applied electric field is measured. The speed of a particle in a unit electric field is

referred to as its electrophoretic mobility (U_E). Zeta potential (ζ) can then be calculated from the measured electrophoretic mobility using the Henry equation:

$$U_E = \frac{2\varepsilon\zeta f(\kappa a)}{3\eta} \qquad (8)$$

where ε is dielectric constant, η is viscosity, and f(κa) is Henry's function in which κ^{-1} is the thickness of the electric double layer and 'a' is the radius of the particle, and therefore κa measures the ratio of the particle radius to electrical double layer thickness.[92]

CHAPTER 3

3. GEOPOLYMER WITH HIERARCHICALLY MESO-/MACROPOROUS STRUCTURES FROM REACTIVE EMULSION TEMPLATING

3.1. Introduction

Over the past decades, geopolymers have received increasing attention as attractive ceramic materials due to the low energy requirements in their production and their promising mechanical properties (compression strength, heat and chemical resistance, etc.).[19a, 50, 93] More recently, new research efforts have been geared to utilizing the material for non-traditional applications such as evaporative cooling,[65] catalysis[68] and drug delivery.[94] Success of such emerging applications of geopolymer materials further requires exploring new methods for controlling pore structures of the materials in nanoscale. In this communication, we demonstrate that a simple *reactive* emulsion templating with biorenewable oil can produce hierarchically porous geopolymer materials with coexisting controllable mesopores and spherical macropores, without the need of significantly modifying the conventional geopolymer synthetic process.

Geopolymers are typically produced by dissolving solid aluminosilicate precursors in a highly alkaline solution (typically with KOH or NaOH) to form a viscous solution ("geopolymer resin") and subsequently curing the resin at ambient temperatures. Recent studies have shown that geopolymers are inherently a nanomaterial exhibiting a dense gel-like structure with 5 − 40 nm-sized amorphous aluminosilicate particles.[17b, 19a, 27] Their chemical structure consists of an amorphous, three-dimensional network of corner-sharing aluminate and silicate tetrahedra, with the negative charge due to Al^{3+} ions

in the tetrahedral sites balanced by the alkali metal ions.[19a, 93] **Figure 18** shows schematic diagrams for the *reactive* emulsion templating process employed in this work and for the final geopolymer product.[95] Emulsions are droplets of one fluid (e.g., oil) dispersed in a second immiscible fluid (e.g., water), which are often stabilized by a surfactant.[96] Mechanically induced droplet breakup generates (meta)stable emulsions with a distribution of droplet sizes. One novelty of the synthetic design in this work is that by employing a vegetable oil (mainly triglycerides[97]), mixing of a geopolymer resin with the oil generates carboxylate surfactants (soap molecules) *in situ* through the saponification reaction of the triglycerides with the highly alkaline geopolymer resin (hence "*reactive*"). The excess oil forms oil droplets which are then embedded in the geopolymer resin. Notably, it has been found in our work that the oil in the droplets continues to undergo saponification reaction during the curing of the mixture in our reaction condition, which turns the originally hydrophobic triglycerides all into soap and glycerol ($CH_2(OH)-CH(OH)-CH_2(OH)$). Those molecules are soluble in water and thus can be extracted by water from the cured solid material, resulting in a porous geopolymer material (**Figure 18b**, see Results and Discussion for details).

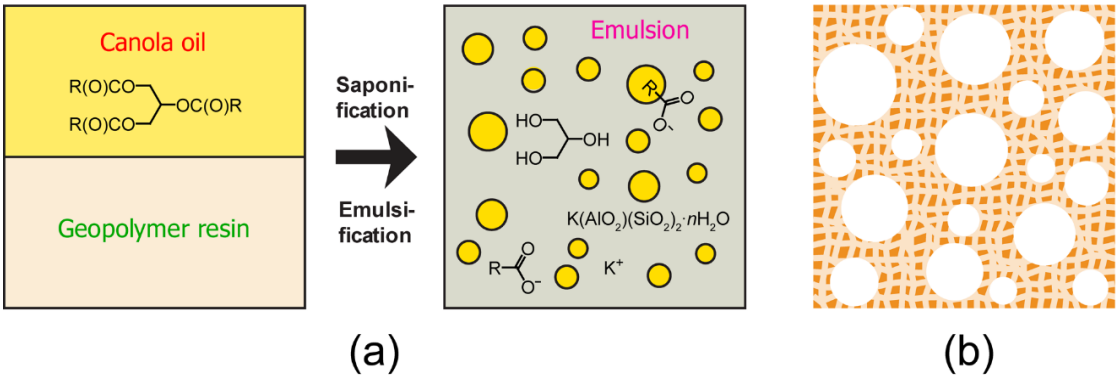

Figure 18. Scheme for the reactive emulsion templating of geopolymer with canola oil (a), and schematic diagram of the resulting hierarchically porous geopolymer with a random mesoporous matrix dotted with spherical macropores (b). The objects in the figures are not scaled.

3.2. Experimental

3.2.1. Synthesis

In the first step of the synthesis, a potassium silicate solution was prepared by dissolving an appropriate amount of KOH pellets (Sigma Aldrich) in deionized water in a polypropylene cup in a water bath. A suitable amount of fumed silica (Cabot, CA-BO-SIL® EH-5) was then added into the KOH solution and the mixture was stirred with an IKA mechanical mixer for 30 minutes at 800 rpm to give a clear solution. The geopolymer resins were then prepared by mechanically mixing metakaolinite into the potassium silicate solution to form a homogenous fluidic liquid. The metakaolinite was produced in advance by calcining kaolinite ($Al_2Si_2O_7 \cdot H_2O$, Alfa Aesar) at 750 °C for 10 h. Various samples were prepared with different water amounts and K/Al ratios but at a fixed Si/Al ratio of 2 (**Table 2**). The pH of the resins was about 14 for all the

compositions. Canola oil (The J.M. Smucker Company, Crisco®), waste vegetable oil (REV biodiesel) or paraffin oil (Alfa Aesar) was then added to the resin at a 1:1 oil-to-water volume ratio and mixed for an additional 15 minutes to give a homogeneous but viscous emulsion. The emulsion was transferred to a polypropylene cup and cured in a laboratory oven at 60 °C for 24 h.

The cured product was then broken into small pieces (approximately 1×1×1 cm^3) and subjected to extraction with hot deionized water, except for **S4** for which hexanes were used. Three series of samples were prepared as shown in **Table 2** in order to investigate the effect of three synthetic parameters on the resulting geopolymer; (1) type of oil (**S2**, **S3**, **S4** and **S5)**, (2) mole fraction of water (**S1**, **S2** and **S7)**, and (3) amount of potassium hydroxide (**S6**, **S7** and **S8)**. Paraffin oil was selected (**S4**) in order to examine the role of saponification, as paraffin oil is pure hydrocarbons and does not undergo a chemical reaction with geopolymer resin. To produce a "control" sample (**R** in **Table 2**), the same synthetic procedure was followed without adding any oil.

3.2.2. Characterization Methods

Powder X-ray diffraction (PXRD) patterns of the finely ground samples were collected using a Siemens D5000 diffractometer with Cu-Kα radiation. Carbon-Hydrogen-Nitrogen (CHN) elemental analyses were performed by employing Perkin-Elmer 2400 Series II CHNS/O Analyzer with a thermal conductivity detector (TCD). Samples for scanning electron microscopy (SEM) were prepared by placing small pieces of the products (approximate cubes of few millimeters in length) on a SEM stub using a copper conducting tape. Samples were then gold coated for 150 s and were studied using SEM-XL30 Environmental FEG (FEI) microscope operating at 10 kV. For transmission

electron microscopic (TEM), colloidal suspensions of ground samples in ethanol were dried on to copper grids and were studied using JEOL TEM/STEM 2010F operating at 200 kV.

N_2 sorption isotherms were obtained with a Micrometrics ASAP 2020 volumetric adsorption analyzer at 77 °K. Samples were degassed at room temperature for 10 h under vacuum until a residual pressure of ≤10 μmHg was reached. Specific surface areas were estimated using Brunauer-Emmett-Teller (BET) equation, in the relative pressure range from 0.06 to 0.2.[98] Pore volumes were calculated from the amount of nitrogen adsorbed at a relative pressure (P/P_o) of 0.99. Pore size distributions were obtained using the Barrett-Joyner-Halenda (BJH) method assuming a cylindrical pore model.[99] Total pore volume of the products was determined by pycnometry with deionized water at 23 ± 2 °C and ambient pressure, whose principle relies on the permeation of water through the open pore network of monolithic solid samples.

Table 2. Pore properties of the porous products from various synthetic conditions.

Sample	Mole Fraction of H_2O (x)	K/Al Ratio	Oil Used	Surface Area (m^2/g)	Pore Volume[a] (cm^3/g)	Average Pore Width[b] (nm)	Total Pore Volume[c] (cm^3/g)	Mesoporosity[d] (%)/ Total Porosity[e] (%)
S1	0.63	2	canola	69	0.44	22	1.5	16/53
R	0.68	2	no oil	62	0.16	7	0.69	5.1/22
S2	0.68	2	canola	97	0.53	17	1.7	19/58
S3	0.68	2	canola + paraffin (1/1; vol/vol)	42	0.40	41	1.7	15/47
S4	0.68	2	paraffin	5	0.03	34	1.1	0.88/31
S5	0.68	2	waste vegetable oil	123	0.37	14	1.6	15/65
S6	0.73	1	canola	55	0.30	17	1.1	13/49
S7	0.73	2	canola	124	0.61	18	1.7	20/53
S8	0.73	3	canola	84	0.70	34	2.1	23/67

[a]From the pores with width no larger than 150 nm in the BJH desorption pore distribution.

[b]4(BJH desorption pore volume)/(BET surface area).

[c]Determined by pycnometry.

[d]From pore volume[a].

[e]From total pore volume[c].

3.3. Results and Discussion

CHN analysis showed only small amounts of carbon (0.5 ± 0.3 wt%), hydrogen (1.3±0.3 wt%), and nitrogen (0.005±0.002 wt%) in average for all samples, **S1** – **S8**, with the maximum carbon content of 1.2 wt% found for **S6**. The values compares well with 0.83 wt% C, 1.4 wt% H and 0.005 wt% N for the sample **R**, which indicates that the hot water extraction removed the organics properly. **Figure 19** shows scanning electron microscope (SEM) and transmission electron microscope (TEM) images of the sample **S2** as a representative example. The material exhibits discrete spherical pores whose diameters range from about 5 to 40 μm in **Figure 19a**. A closer look in **Figure 19b**

reveals that the pore wall separating the spherical pores has a finer structure throughout the matrix. The corresponding TEM micrographs in **Figure 19c & d** show the gel-like nanostructure of the material consisting of nanoparticles of about 20 nm that are strongly fused by necks, which is consistent with previous results.[19a, 27] The materials were amorphous based on the largely featureless 'hump' centered at approximately 27 – 30° in 2θ, the unique feature of geopolymer, in their powder X-ray diffraction patterns (not shown).[93a] The combination of the SEM, TEM and XRD results surmises that the geopolymer products exhibit a mesoporous geopolymer matrix made of rather leisurely connected amorphous aluminosilicate nanoparticles and that large spherical macropores are scattered over throughout the mesoporous matrix (**Figure 18b**). It is reminded that the extraction process removed the organic components completely, which strongly suggests that the mesopores in the geopolymer matrix are connected and *open* to allow the solvent and other molecules to flow in and out.

The samples were characterized further by applying Brunauer-Emmett-Teller (BET) and Barrett-Joyner-Halenda (BJH) analyses to N_2 sorption isotherms for the samples, and the results are summarized in **Table 2**. **Figure 20** shows the isotherms and BJH desorption pore distribution of the samples with the same precursor composition at K/Al = 2 and x = 0.68 but with different types of oil (**S2** − **S5**) along with the control sample **R** prepared without oil. All the samples except **S4** show a noticeable hysteresis in their isotherms (**Figure 20a**), indicating the presence of mesopores.[100] The sizes of mesopores show a relatively narrow distribution in **Figure 20b** centered in the mesopore region (10 – 50 nm). Excluding **S4**, the sample **R** shows the lowest BJH cumulative pore volume (0.16 cm^3/g) and the smallest average pore diameter (7 nm), while the ones

prepared with oil containing triglycerides (**S2**, **S3** and **S5**) show a significantly higher porosity with the BJH pore volume up to 0.53 cm^3/g and the average pore width up to 41 nm. The sample **S4** prepared with paraffin oil shows a BJH pore volume even lower than the control sample **R**.

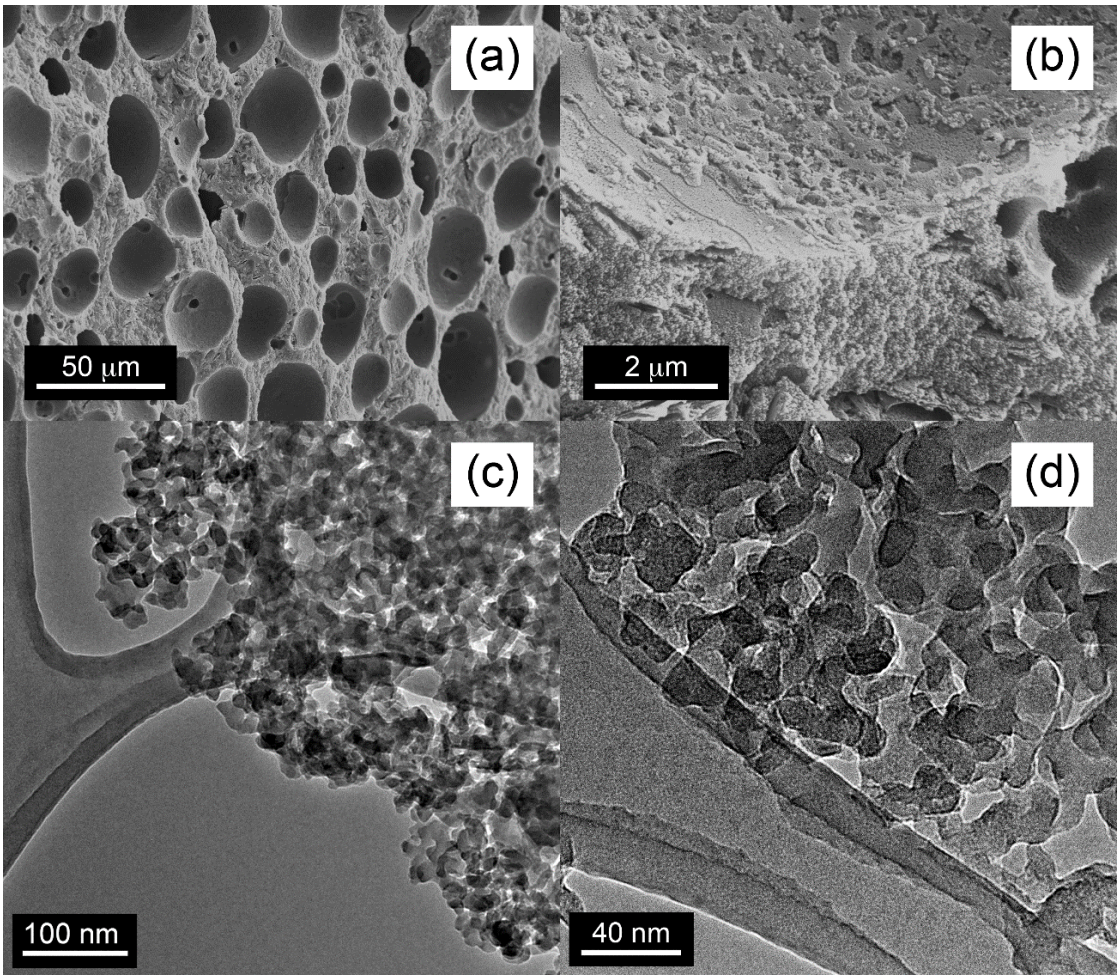

Figure 19. SEM images in (a) and (b) (scale bar = 50 and 2 μm, respectively) and TEM images in (c) and (d) (scale bar = 100 and 40 nm, respectively) of sample **S2**.

The presence of mesopores (10 – 50 nm) indicated from the gas sorption studies is consistent with the textural pores among the fused nanoparticles seen in **Figure 19c & d**.

It is noted that the samples maintained their monolithic feature during the solvent extraction. When water was used for extraction, however, the original pieces broke into smaller monolithic particulates of about 3 mm in diameter, which might be due to the large capillary forces exerted by water in the micro-cracks that developed during curing. The solids were robust and did not lose their structural integrity during sample handling and soaking for water pycnometry, although the quantification of the mechanical strength of the materials is warranted in the future. Such a structural integrity is unusual for geopolymer materials with high total porosities up to 67% observed in our case (**Table 2**). The porosity from mesopore structure (given as nanoporosity in **Table 2**) is actually no greater than 23%, and hence the matrix itself possibly maintains its rigidity while the additional spherical macropores increase the total porosity of the materials.

The negligible nanoporosity (0.88 %) for the sample **S4** is intriguing because paraffin oil turned out in our experiments to mix well with the geopolymer resin and could produce porous geopolymer (total pore volume = 1.1 cm^3/g). Detailed SEM studies on **S4** (not shown) indicate that the material indeed exhibits the spherical macropores (20 – 50 μm) like others, but interestingly the pore walls show additional macropores of about 2 μm instead of mesopores. It is suspected that the small macropores are open and connected together, as all the paraffin oil could be extracted out according to the CHN analyses. In any event, the presence of the small macropores in **S4** instead of the mesopores found in other samples indicates that the saponification reaction does play a significant role in pore formation probably by providing the *in situ* formed surfactant and also water-soluble glycerol byproduct.

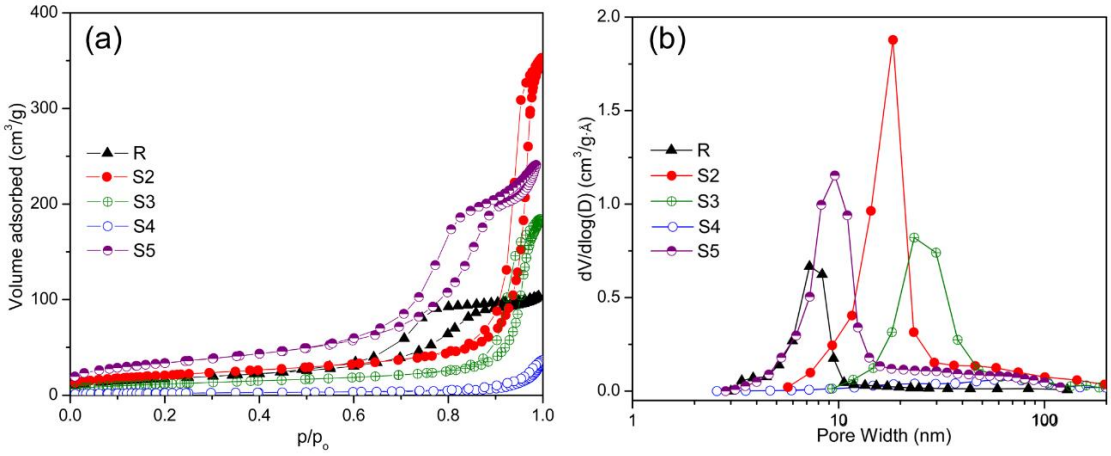

Figure 20. Nitrogen sorption isotherms (a), and BJH desorption pore size distribution curves (b) of samples **R1**, **S2**, **S3**, **S4** and **S5**. All samples have same composition but they differ in the type of oil (**Table 2**) used in their preparation.

In addition to the oil type, the amount of water and K/Al ratio are shown to control porosity of the products as well. With a fixed ratio of K/Al = 2 and canola oil, samples **S1**, **S2** and **S7** show an increase in the BJH cumulative pore volume 0.44 to 0.61 cm^3/g upon increasing the mole fraction of water from 0.63 to 0.73, while their pore widths are more or less the same **(Table 2**). Meanwhile, the increase in the K/Al ratio also significantly increases the pore volume and pore width. With canola oil and *x* fixed at 0.73, the samples **S6** – **S8**, prepared with K/Al = 1, 2 and 3, show BJH cumulative pore volumes of 0.30, 0.61 and 0.70 cm^3/g and the average pore widths of 17, 18 and 34 nm, respectively. The higher amount of KOH in the precursor solution may lead to a more extensive saponification reaction, which in turn provides a higher porosity in the final product. Despite the excess amounts of KOH in the precursor, it is worth mentioning that all the products showed a neutral pH after the water extraction, indicating again that the pore structure is open for permeation of water in the matrix, hence enabling the removal

of the excess alkaline component during the extraction. It is noted that the products were found to keep their structural integrity and the original porosity even after prolonged soaking in acidic solutions with a pH value as low as 3.

3.4. Conclusions

We have demonstrated that a simple synthesis of hierarchically porous geopolymers is possible by employing emulsion templating with triglyceride oil. The coexisting distinctive mesopores and macropores were characterized using the N_2 sorption, SEM, TEM and pycnometric studies. We have also shown that the pore size and/or volume can be controlled by changing synthetic parameters such as oil type, and water and alkali contents in precursor solution. Further studies are due for elucidation of the precise role of those synthetic parameters and potentially others in controlling the porosity and also for quantitative examination of stability of this new class of porous ceramics under various physical and chemical stresses.

CHAPTER 4

4. PHASE DIAGRAMS OF POROUS GEOPOLYMERS

4.1. Introduction

In the aftermath of numerous fires involving organic plastics in France between 1970 – 73, Joseph Davidovits explored fire resistant inorganic polymers and developed amorphous to semi-crystalline, three-dimensional aluminosilicate materials which he called geopolymers.[93a] Although geopolymers are X-ray amorphous, their compositions and structural building blocks are very similar to zeolites, microporous crystalline materials that find applications in the petroleum and other industries.[50] Both the Al and Si ions are tetrahedrally coordinated, forming a polymeric network structure. Because of the +3 charge of the Al, the tetrahedral network is negatively charged and must be balanced. Na and K ions are the most common cations, but others like Li, Cs, and Mg can also be used.[101] Recently it has been shown that the nanoporous amorphous geopolymers could be useful in non-traditional applications like catalysis and ion exchange, similar to their crystalline zeolite analogues.

Geopolymers have pores due to water evaporation during the curing process, and the pore sizes range from less than 10 nm to about 5 μm, depending on composition and curing conditions. However, the pores, especially those less than 10 nm, are usually closed and inaccessible. There have been two general approaches to introducing pores within geopolymers. The first utilizes in situ gas-forming agents like H_2O_2 or silica fume as the porogens, however such methods would create mainly closed cells.[102] This method results in pores much larger than a micron. The second is tuning the geopolymer

composition by changing the molar ratios of SiO_2/Al_2O_3, M_2O/Al_2O_3 (M = alkali metal) and H_2O/Al_2O_3.[65] Higher ratios of H_2O/Al ($10<H_2O/Al<20$) and lower ratios of Si/Al (<1.5) give reasonably porous geopolymers.[101] Recently, porosities up to 45% were achieved merely by changing the amount of water used for synthesis.[103] More recently, (as discussed in chapter 3) we reported a technique to introduce highly interconnected meso/macropore network into the geopolymer structure via a reactive emulsion templating method utilizing triglyceride oil.[95, 104]

Geopolymers are typically produced by dissolving a solid aluminosilicate precursor in a highly alkaline solution (containing sodium or potassium hydroxide/silicate) to form a viscous solution ("geopolymer resin") and subsequently curing the resin at ambient temperatures. Compositionally, the geopolymer resin (at least the purest one produced from metakaolinite) is a four component system, specifically, silicon, aluminum, sodium and/or potassium, and water. This study aims at exploring the phase space of the geopolymerization process via the newly found emulsion route and compare the pore properties of thus produced products with those prepared in a traditional way. However, plotting such a four compositional system would lead to a three dimensional quaternary phase diagram (**Figure 21**a) with a mole fraction of each of the parameters as its four vertices. Due to the complexity, such a three dimensional phase diagram could not be readily interpreted. However, if one of the four components (say water) is held constant at a given value, it can be collapsed into a simpler, two dimensional ternary phase diagram (**Figure 21b**) that could be read conveniently. Essentially, a three dimensional regular tetrahedron can be sliced into several two

dimensional equilateral triangles across which one of the four variables is held constant while the other three are varied (**Figure 21**).

Herein, five such slices or ternary diagrams are constructed by fixing the mole fraction of water at 0.58, 0.63, 0.68, 0.73 and 0.77. The three dimensions accounted by a single ternary diagram are the mole fractions of silicon, aluminum, and potassium (or hydroxide). The fourth dimension was the mole fraction of water. Metakaolin was selected as the solid aluminosilicate precursor in this investigation because metakaolin system is considered to produce the simplest geopolymer resins of all. Additionally, potassium hydroxide was carefully chosen for this exploration due to the fact that crystallization into potential zeolitic phases is less rapid in KOH/metakaolin geopolymers compared to the NaOH/metakaolin system.[41]

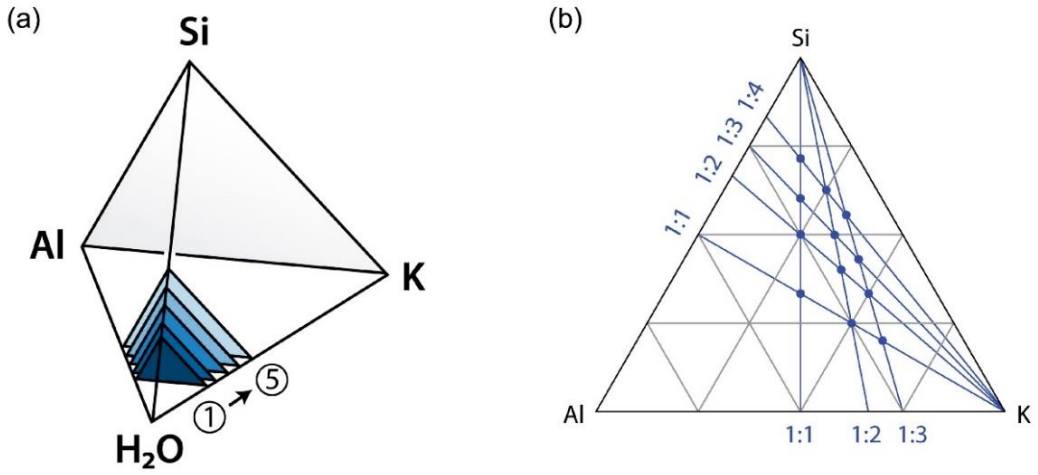

Figure 21. Regular tetrahedron illustrating a three dimensional quaternary phase diagram (a), and an equilateral triangle depicting a two dimensional ternary phase diagram (b).

4.2. Experimental

4.2.1. Synthesis

In the first step of the synthesis, a potassium hydroxide solution was prepared by dissolving an appropriate amount of KOH pellets (Sigma Aldrich) in deionized water in a polypropylene cup in a water bath. A suitable amount of commercial potassium silicate (~60.8% H_2O, 12.6% K_2O, ~26.6% SiO2; KASIL® 6, PQ Corporation)[105] was then added into the KOH solution to give a clear solution. The geopolymer resins were then prepared by adding metakaolin (MetaMax® from BASF, Lot# 10408G023)[106] into the potassium silicate solution and stirring the mixture mechanically (IKA® RW 60 digital mixer) for 30 minutes at 800 rpm to form a homogenous fluidic liquid. Various samples were prepared with different water amounts, K/Al ratios and Si/Al ratios (**Table 3**). The pH of the resins was about 14 for all the compositions. Canola oil (The J.M. Smucker Company, Crisco®) was then added to the resin at a 1:1 oil-to-water volume ratio and mixed for an additional 15 minutes to give a homogeneous but viscous emulsion. The emulsions were transferred to a polypropylene cup and cured in a laboratory oven at 60 °C for 24 h.

The cured products were then broken into small pieces (approximately 1×1×1 cm^3) and subjected to extraction with hot deionized water. By the end of the extraction, pH of the products was ~8. The resulting products (final products) free of organics were dried overnight in the lab oven maintained at 120 °C and were stored in sealed vials for further analysis. Complete removal of organics for selected representative samples was confirmed by CHN analysis and Infrared studies (data not shown). Several samples were

prepared as shown in **Table 3** in order to investigate the effect of four compositional parameters on the resulting geopolymer: mole fractions of (1) H_2O, (2) Si, (3) Al, and (4) K (or KOH). To produce "control" samples (without oil samples in **Table 3**), the same synthetic procedure was followed without adding any oil. For the ease of discussion, samples are labelled according to their compositions i.e. mole fraction of water is followed by mole ratios of K, Al and Si, respectively. For examples, 0.73-312 represents a geopolymer product prepared from the composition in which the mole fraction of water was 0.73 and K:Al:Si = 3:1:2.

4.2.2. Characterization

Powder X-ray diffraction (PXRD) patterns of the finely ground samples were collected using a Siemens D5000 diffractometer (Ni-filtered Cu Kα radiation with a wavelength of 1.5406 Å, operated at 40 kV and 40 mA, VANTEC-1 position-sensitive detector) at a scan speed of 2.0 degrees/min and a step size of 0.016 degrees 2θ. The resolution of the VANTEC-1 position-sensitive detector was $2\theta = 0.008$ degrees. Samples for scanning electron microscopy (SEM) were prepared by placing few pieces of the products on a SEM stub using a copper conducting tape. Freshly exposed virgin surfaces of the samples were then gold coated for 100 s and were studied using SEM-XL30 Environmental FEG (FEI) microscope operating at 5 kV. For transmission electron microscopic (TEM) studies, colloidal suspensions of ground samples in ethanol were dried on to copper grids and were studied using TEM/STEM 2010F (JEOL) operating at 200 kV.

Table 3. Pore properties of the products prepared with and without adding oil.

Composition X_{H_2O}-KAlSi	Morphology of final products		BET surface area (m^2/g)		Mesopore volume[a] (cm^3/g)		Mesopore width[b] (nm)	
	Without oil	With oil	Without oil	With oil	Without oil	With oil	Without oil	With oil
0.77-113	particles	particles	18	25	0.07	0.09	14	15
0.77-213	particles	particles	227	259	0.23	0.78	2	12
0.77-313	particles	particles	51	135	0.30	1.02	24	30
0.77-111	particles	powder	6	21	0.03	0.05	16	17
0.77-211	powder	powder	23	11	0.04	0.03	10	12
0.77-311	powder	powder	8	14	0.03	0.05	10	13
0.73-113	particles	particles	55	24	0.11	0.11	7	19
0.73-213	particles	particles	180	221	0.18	0.69	3	17
0.73-313	particles	particles	140	137	0.26	0.90	7	26
0.73-112	particles	particles	12	33	0.06	0.33	17	39
0.73-212	particles	particles	24	150	0.07	0.76	16	21
0.73-312	particles	particles	163	87	0.11	0.78	10	35
0.73-111	particles	powder	5	15	0.02	0.05	15	14
0.73-211	powder	powder	22	10	0.05	0.04	9	10
0.73-311	powder	powder	14	13	0.06	0.04	16	18
0.68-112	particles	particles	22	28	0.11	0.21	9	34
0.68-212	particles	particles	62	157	0.16	0.52	7	14
0.68-312	particles	particles	160	77	0.26	0.54	10	27
0.68-111	particles	particles	6	14	0.03	0.06	18	18
0.68-211	particles	particles	19	18	0.07	0.05	15	10
0.68-311	particles	particles	15	16	0.09	0.07	23	18
0.63-112	particles	particles	11	25	0.02	0.11	25	30
0.63-212	particles	particles	53	110	0.13	0.29	10	18
0.63-312	particles	particles	118	85	0.22	0.37	10	24
0.63-211	particles	particles	15	17	0.06	0.05	18	11
0.63-311	particles	particles	17	15	0.05	0.07	19	18
0.58-112	particles	particles	14	35	0.04	0.10	21	29
0.58-212	particles	particles	33	89	0.10	0.28	17	16
0.58-312	particles	particles	68	53	0.18	0.36	11	24
0.58-211	particles	particles	16	14	0.07	0.05	17	15
0.58-311	particles	particles	12	14	0.05	0.06	17	18

[a]From the pores with width no larger than 150 nm in the BJH desorption pore distribution.

[b]4(BJH desorption pore volume)/(BET surface area).

N_2 sorption isotherms were obtained with a Micrometrics ASAP 2020 volumetric adsorption analyzer at 77 K. Samples were degassed at room temperature for 10 h under

vacuum until a residual pressure of ≤10 μmHg was reached. Specific surface areas were estimated using Brunauer-Emmett-Teller (BET) equation, in the relative pressure range from 0.06 to 0.2.[98] Pore volumes were calculated from the amount of nitrogen adsorbed at a relative pressure (P/Po) of 0.99. Pore size distributions were obtained using the Barrett-Joyner-Halenda (BJH) method assuming a cylindrical pore model.[99]

4.3. Results and Discussion

4.3.1. Synthesis

In this section we discuss nanoporous geopolymer synthesis as a function of four compositional parameters: mole fractions of water, silicon, aluminum, and potassium hydroxide. Potassium was preferred as an activator to sodium because geopolymer products prepared from potassium activating solutions are known to be more homogeneous owing to the greater rate of dissolution of raw materials in potassium hydroxide solutions compared to sodium hydroxide solutions. Higher rate of dissolution is attributed to the greater basicity of potassium hydroxide combined with the lower viscosities of potassium activating solutions.[40-41] Furthermore, potassium activation is less-likely to generate crystalline phases in the resulting geopolymer products, at least within the curing duration of 24 hours employed in this investigation.[17b] In the previous chapter we demonstrated that nanopores (meso-/macropores) can be introduced into the otherwise dense geopolymeric products by preparing them in the presence of various oils (triglycerides).[104] For the sake of simplicity, canola oil was the oil of choice throughout this study and its amount was held constant at 1:1 oil-to-water volume ratio for all the compositions attempted.

Five ternary diagrams were constructed by fixing the mole fraction of water (X_{H_2O}) at 0.77, 0.73, 0.68, 0.63, and 0.58. Geopolymer resins with compositions containing $X_{H_2O} \geq 0.78$ in general were very fluidic with low viscosities and resulted in a phase separation between oil phase and aqueous based geopolymer resin phase upon mixing canola oil. On the contrary, geopolymer resins with $X_{H_2O} \leq 0.57$ in general were highly viscous which also led to a phase separation between oil phase and geopolymer resin phase. Geopolymer resin and oil formed a visually homogenous phase only in the range of $0.58 \leq X_{H_2O} \leq 0.77$. Moreover, within each of these ternary systems, Si/Al and K/Al ratios were varied. The lower limit of Si/Al of one was set by the aluminum avoidance rule (more famously known as Lowenstein's rule)[10] which states that no two ^{68} tetrahedra can be next to each other. Attempts to prepare appropriate potassium silicate solutions suitable for producing geopolymer products with Si/Al ratios greater than three resulted in precipitation of silica gel due to the large excess of SiO_2. Hence Si/Al ratio was only varied from one to three. Likewise, the lower limit of K/Al was set at one (a stoichiometric amount) due to the fact that each ^{68} tetrahedra in the fully reacted products would require an associated cation in order to achieve charge neutrality. On the other hand, since the excess potassium hydroxide present in K/Al = 3 compositions was enough to completely saponify the canola oil added to the geopolymer resins, hence K/Al ratios greater than three were not pursued. Therefore, the attempted compositional space in this study can be written as X_{H_2O}-*abc*, where '*a'* is K/Al ratio (1, 2 or 3), '*b'* is mole ratio of aluminum (set at 1), and '*c'* is Si/Al ratio (1, 2 or 3). Although geopolymers with

non-integral values of '*a'* and '*c'* are possible, they are not attempted for the sake of limiting the number of data points.

All the compositions that formed visually homogeneous emulsions upon mixing with oil are listed in **Table 1** along with the morphologies of the resultant final products and their mesopore properties. In order to appreciate the role of oil, the morphologies and mesopore properties of control geopolymer products that were prepared without mixing oil are also listed. Geopolymer resins with *c* =1, irrespective of X_{H_2O} and '*a'* values were very viscous and non-fluidic. Increasing either X_{H_2O} or '*a'* or both formed slightly less viscous resins but they were still non-fluidic. All X_{H_2O}-*abc* compositions (except X_{H_2O} of 0.63 and 0.58, and *a* = 1 in which phase separation was noticed) formed visually homogeneous emulsions with oil. However, rather surprisingly, the resulting geopolymer products lacked significant mesoporosity. Their mesopore properties are comparable to the control products meaning mixing of oil did not develop additional mesoporosity in these compositions. Incidentally, the control samples with *a* = 1 were monolithic but with severe cracks all over the products. The cracks were developed most probably due to the uncontrolled evaporation of water during the curing stage.

Resins with *c* = 2 were fairly fluidic whose viscosity decreased with increasing water (X_{H_2O}) and alkali (*a*) contents. For instance, 0.77-*ab2* resins were so fluidic that they resulted in phase separation upon mixing with oil. All other resins with *c* = 2 gave visually homogeneous emulsions with oil and the resulting geopolymer products were monolithic in nature. One common feature of these geopolymer products was that they all exhibited enhanced mesoporosity when compared to their control counterparts (**Table**

3) highlighting the important role played by the triglyceride oil. On the contrary, resins with c = 3 were very viscous with only those having X_{H_2O} = 0.73 and 0.77 forming homogenous emulsions with oil. The resultant geopolymer products were exceedingly porous compared to their control analogues.

4.3.2. Ternary Phase Diagrams

Here, we compare mesopore properties at different synthetic parameters using ternary diagrams shown in **Figure 22** and **Figure 23**, which plot the nominal mole fractions of silicon, aluminum and potassium used to synthesize geopolymer products. The hydroxide content is specified as K to emphasize the use of K^+ ions, which are introduced in equal amount as hydroxide (the activator). Each data point additionally displays the mesopore volume score representing the measure of mesopore volume and hence the mesoporosity exhibited by the corresponding geopolymer products. Mesopore volume score ranged between 0 – 10 with a higher score signifying larger mesopore volume and vice versa. Specifically, products with a mesopore volume less than 0.09 cm^3/g were given a mesopore volume score of zero and those with mesopore volume ranging between 0.10 – 0.15 cm^3/g were given a mesopore volume score of one. Beyond that, the mesopore volume score was increased in increments of one for mesopore volume incremental intervals of 0.09 cm^3/g. For example, products with mesopore volume ranging between 0.36 – 0.45 and 0.46 – 0.55 cm^3/g were given a score of four and five, respectively. All geopolymeric products produced here (60 °C curing for 24 h) whether by mixing oil or not were amorphous as determined by PXRD analysis. The common feature of all powder patterns was the distinctive amorphous hump between 27

– 29° in 2θ demonstrating the formation of geopolymeric products. It has been well recognized that the geopolymers are metastable relative to zeolites, and other aluminosilicate minerals; therefore, if given enough time geopolymers may transform to more stable crystalline structures.[107] Hence it is noteworthy that the ternary phase diagrams presented here are not thermodynamic phase diagrams but rather are kinetic phase diagrams.

The ternary diagrams in **Figure 22** and **Figure 23** show that all geopolymer products with nominal Si/Al ratio (or '*c*') = 1 along with their control analogues, without any exception, exhibited a mesopore volume score of zero meaning they all lacked mesoporosity to any notable extent. More precisely, their mesopore volume was ≤ 0.09 cm^3/g of products. Although they lack mesopores, the fact that no phase separation between oil and geopolymer resin occurred during the mixing and curing stages suggest that the possibility of these products having macropores cannot be ruled out.

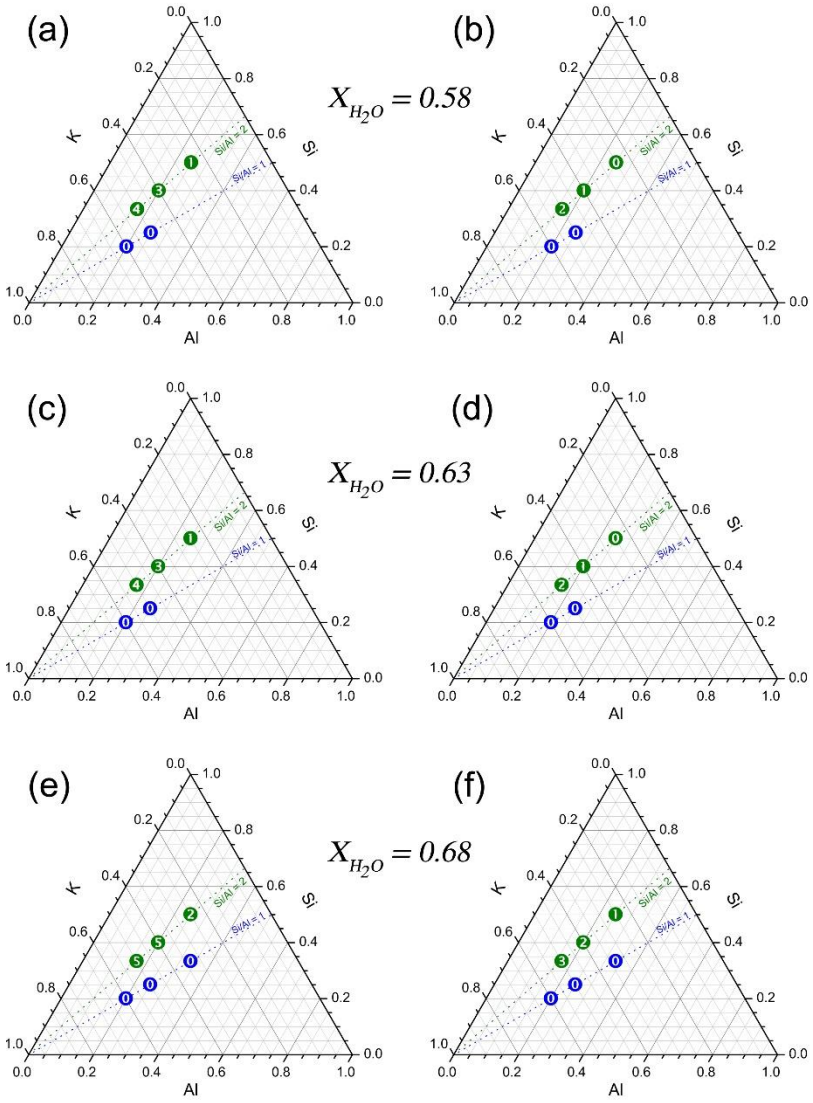

Figure 22. Ternary phase diagrams of geopolymer products showing the mesopore volume score at increasing mole fraction of water: 0.58 (a and b), 0.63 (c and d), and 0.68 (e and f). Ternary diagrams on the left (a, c and e) represent geopolymer products prepared by mixing canola oil while those on the right (b, d and f) correspond to their respective control analogues. The mesopore score of 0, 1, 2, 3, 4, and 5 corroborate to a mesopore volume ranging between 0 – 0.09, 0.10 – 0.15, 0.16 – 0.25, 0.26 – 0.35, 0.36 – 0.45, and 0.46 – 0.55 cm^3/g, respectively. The axes in the ternary phase diagram are Si, Al and K mole fractions.

On the other hand, geopolymer products obtained from compositions with nominal Si/Al ratio (or '*c*') = 2 were monolithic similar to their control analogues, except those prepared my mixing oil were much lighter indicating the enhanced porosity in them. Higher mesopore volume scores of the products prepared from emulsions compared to their control samples as presented in **Figure 22** and **Figure 23** supports the aforementioned conclusion. Furthermore, mesopore volume score increased with increasing K/Al ratio (or '*a'* value) for products prepared via emulsion route and to a lesser extent in the case of control samples as well. Such an increase is most prominent in the ternary diagrams with greater amount of water. For instance, in ternary diagram with X_{H_2O} = 0.73 (**Figure 23a**), the mesopore volume score increased greatly from 3 to 8 upon moving from '*a*' = 1 to '*a*' = 3. This increment in the mesopore volume with increasing alkali content could be a direct consequence of greater extent of saponification reaction occurring between oil and the excess alkali introduced. However, similar argument cannot be made to explain the trend seen in the control samples. Additionally, for a given value of '*a'* and '*c',* mesoporosity increased by merely increasing the water content, a trend previously reported by Jämstorp et. al.,[94] who attributed it to the increased water of syneresis at increased water contents. Syneresis is a process in which the fluid (H_2O in this investigation) is expelled from the interstices of the structure into larger pores during the structural reorganization of preformed gels.[40]

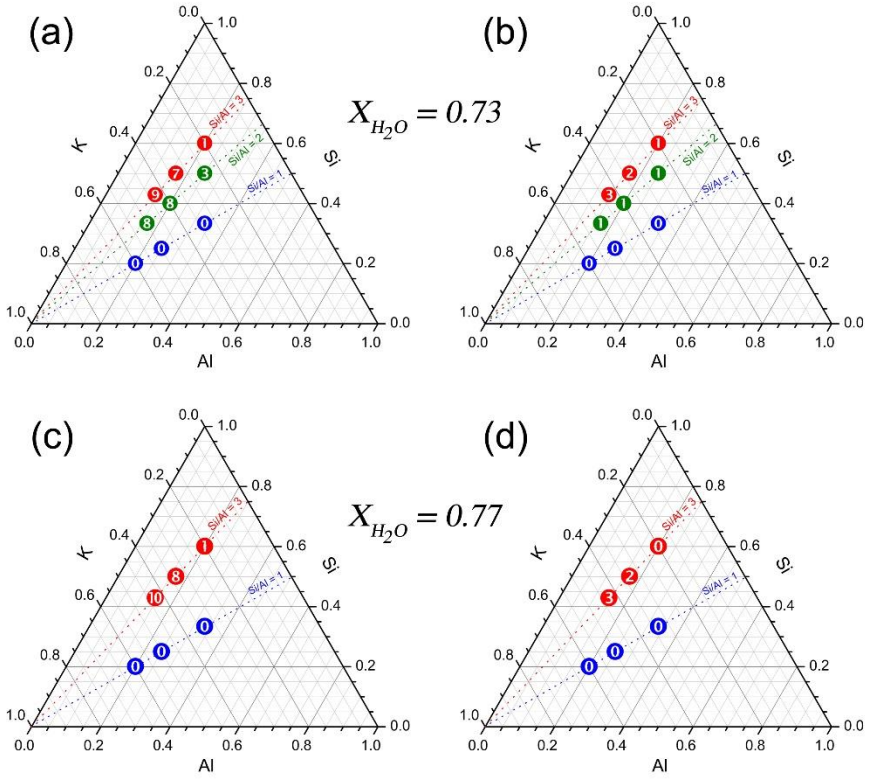

Figure 23. Ternary phase diagrams of geopolymer products showing the mesopore volume score at a water mole fraction of 0.73 (a and b) and 0.77 (c and d). Ternary diagrams on the left (a and c) represent geopolymer products prepared by mixing canola oil while those on the right (b and d) correspond to their respective control analogues. The mesopore score of 0, 1, 2, 3, 7, 8, 9, and 10 corroborate to a mesopore volume ranging between 0 – 0.09, 0.10 – 0.15, 0.16 – 0.25, 0.26 – 0.35, 0.66 – 0.75, 0.76 – 0.85, 0.86 – 0.95, and 0.96 – 1.05 cm^3/g, respectively. The axes in the ternary phase diagram are Si, Al and K mole fractions.

Lastly, the geopolymers prepared with nominal Si/Al ratio (or '*c*') = 3 were all monolithic and in general exhibited the highest mesoporosity, while following the trends similar to those with '*c*' = 2. Specifically, products obtained from emulsions are more

mesoporous than their control counterparts, and within a given ternary diagram (**Figure 23a – d**), the mesopore volume scores increased with increasing K/Al ratio (‘*a’* value). Furthermore, mesoporosity increased with increasing water content. Mesopore volumes as high as 0.90 and 1.02 cm^3/g could be achieved for the products produced from a nominal compositions of 0.73-313 and 0.77-313, respectively.

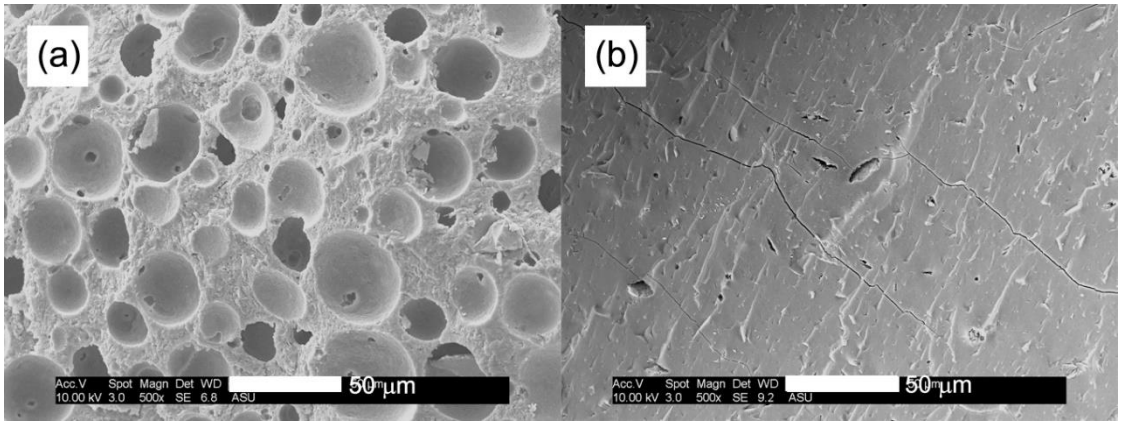

Figure 24. SEM images of representative geopolymer product prepared with oil (a) revealing evenly distributed macropores, and control product prepared without oil (b). Nominal composition was 0.77-313.

Although not shown here, N_2 sorption analysis revealed that the pore size distribution curves (BJH pore size distribution) of the products prepared via emulsion route in general exhibited a broad range covering pores within an entire mesopore region (2 – 50 nm) and in some cases even extending into the lower end of the macropore region (50 – 150 nm). Furthermore, SEM analysis (**Figure 24a**) disclosed the presence of even bigger macropores (10 – 50 μm) evenly distributed all over these products. Such a pore system would be very beneficial where diffusion of molecules in and out of the pores is desired, for example in catalytic and/or adsorption based applications. On the other hand,

control products prepared without mixing oil exhibited ill-shaped hysteresis loops in gas sorption isotherms and narrow pore size distributions when probed by N_2 sorption as previously observed for traditional geopolymers.[40] Furthermore, control samples did not reveal any notable macropores upon imaging under SEM (**Figure 24b**).

4.4. Conclusions

Here, we present phase diagrams that allows a simplistic, unambiguous identification of compositions and conditions for the formation of hierarchically porous geopolymers with specific pore properties. This is the first quantitative exploration of such diagrams for geopolymer synthesis, which could prove beneficial for identifying a parameter space for tailoring the pore properties. In this study, we constructed ternary phase diagrams for the production of geopolymers via emulsion method and compared the products produced through the traditional route. Four compositional parameters: mole fractions of Si, Al, KOH and water are judiciously considered. All geopolymers produced by activating the metakaolin with potassium silicate solutions (i.e. $Si/Al \neq 1$ products) exhibited enhanced mesoporosity when prepared via emulsion route highlighting the important role played by the triglyceride oil. Produced this way, mesopore volume as high as 1.02 cm^3/g could be achieved while still retaining the monolithic form, albeit with decrease mechanical strength. On the other hand, oil seems to have no effect on the mesoporosity of geopolymers produced by activating the metakaolin with potassium hydroxide solutions (i.e. $Si/Al = 1$ products). However, macroporosity is anticipated in all the products that are prepared from non-phase separating emulsions. It is reminded that these phase diagrams are kinetic rather than

thermodynamic, and given enough time and/or heating at higher temperatures could lead to zeolitic phases. To this end, non-compositional parameters like time and temperature are also worth considering in future investigations.

CHAPTER 5

5. IRON OXIDE−MODIFIED NANOPOROUS GEOPOLYMERS AS MEDIA FOR ARSENIC REMOVAL FROM CONTAMINATED GROUND WATER

5.1. Introduction

Arsenic is ubiquitous and ranks 20th in natural abundance, 14th in sea water, and 12th in human body.[108] It is mobilized by natural weathering reactions, biological activity, geochemical reactions, volcanic emissions and other anthropogenic activities such as mining, combustion of fossil fuels, and use of arsenic additives to pesticides, herbicides and livestock.[109] Arsenic is one of the most frequently found contaminants in many drinking water sources in small and rural communities all over the world. The largest population at risk among all the countries with known groundwater arsenic contamination is in Bangladesh, followed by the state of West Bengal in India.[110] Although arsenic is an essential element, two types of toxicity, viz., acute and sub-acute are known from long time exposure.[111] International Agency for Research and Cancer (IARC) classifies arsenic as class A carcinogen and its maximum mandated, or recommended levels in drinking water is set at 10–50 µg/L depending on a country's regulations, for example, United States Environmental Protection Agency (USEPA) set it at 10 µg/L.[78, 112] The acute toxicity of arsenic compounds in humans predominantly depends on their rate of removal from the body. Prolonged intake of arsenic contaminated drinking-water is known to cause dermal lesions such as hyper- and hypopigmentation, peripheral neuropathy, skin cancer, bladder and lung cancers and peripheral vascular disease.[113] Although arsenic can exist in −3, 0, +3 and +5 oxidation

states in the earth's crust, in natural waters, it is mostly present in +5 state (arsenate, AsO_4^{3-}), but under anaerobic conditions, it is likely to be present in +3 state (arsenite, AsO_3^{3-}).[109b, 114] Several technologies have been reported for removing arsenic from drinking water based on the principles, such as oxidation/precipitation, bioremediation, coagulation/precipitation, adsorption, ion exchange, and membrane filtration.[109b, 115] Out of these, technologies based on adsorption processes are most promising because they are cost effective, versatile and simple to set up.[116] Among several types of reported materials capable of removing arsenic, iron oxides, such as ferrihydrite, amorphous hydrous ferric oxide (HFO), hematite and goethite have excellent selectivity towards arsenic, which predominantly exist as arsenate and arsenite in ground water.[117] High adsorption capacities have been achieved by making them in porous forms, for example, granular ferric hydroxide (GFH) while keeping the high selectivity.[118] However, many of the granular iron oxide based media lack mechanical stability and break down into finer particles which pose operational problems.[115b] Furthermore, GFH suffer from very slow diffusion kinetics of arsenic species, with effective intragranular diffusion coefficients 5 to 7 orders of magnitude smaller than the diffusion coefficients of arsenic species in bulk solution.[119] Recently nanosized iron oxide loaded high surface area materials like granular activated carbons, mesoporous silicas (MCM-41, SBA-15, KIT-6) and mesoporous carbons have been developed which showed improved performance due to superior kinetics and also exhibited better mechanical properties.[120] However, due to high surface areas and poor crystallinity, mesoporous silica materials are known to undergo dissolution in water releasing soluble silica species which are known to compete with adsorption of arsenic species onto the active sites of iron oxides.[121] A number of

strategies have been developed to improve the hydrolytic stability of mesoporous silica materials, out of which incorporating Al into their framework via direct synthesis is arguably the most attractive.[122] In this study, we detail using synthetic amorphous aluminosilicate materials called geopolymers with a Si/Al ratio of 2.0 or 1.5.

Geopolymers are an emerging class of ceramic-like material that is gaining significant attention due to their unusual properties, such as high compressive strengths, good heat and chemical resistance, and low environmental impact during production. Beyond the conventional applications as building or refractory materials[123] or in immobilizing toxic wastes,[124] new research efforts are being focused towards introducing porosity into the material and utilize them in catalysis[125] and drug delivery.[94, 126] Recently, we introduced hierarchically meso/macroporous structure into the otherwise dense geopolymeric matrix following a simple and readily scalable synthetic methodology developed in our lab.[104, 127] Having hierarchical pore structure is advantageous because the smaller mesopores can be easily accessed through the larger macropores, hence improving the diffusion kinetics of fluids onto the active sites. Herein, we report using hierarchically porous geopolymer materials having high surface areas as supporting media for HFO – an active material introduced via wet impregnation for the removal of arsenic. This also opens up the ways to introduce numerous other active materials into the hierarchically porous network of geopolymer materials. To the best of our knowledge this is the first report regarding the use of geopolymer materials for arsenic removal.

5.2. Experimental

5.2.1. Synthesis of Nanoporous Geopolymer Material (Base Media)

In the first step of the synthesis, a potassium silicate solution was prepared by dissolving an appropriate amount of KOH pellets (Sigma Aldrich) in deionized water in a polypropylene cup placed in a water bath. A suitable amount of fumed silica (Cabot, CA-BO-SIL® EH-5) was then added into the KOH solution and the mixture was stirred with a Stir-Pak laboratory mixer for 30 minutes at 800 rpm to give a clear solution. The geopolymer resins were then prepared by mechanically mixing metakaolinite into the potassium silicate solution to form a homogenous fluidic liquid. The metakaolinite was produced in advance by calcining kaolinite ($Al_2Si_2O_7 \cdot H_2O$, Alfa Aesar) at 750 °C for 10 h. Eight different samples were prepared by varying the amounts of water, K/Al ratio and Si/Al ratio (**Table 4**). The pH of the resins was about 14 for all the compositions. Canola oil (The J.M. Smucker Company, Crisco®), paraffin oil (Alfa Aesar) or a mixture of both oils (**Table 4**) was then added to the resin at a 1:1 oil-to-water volume ratio and mixed for an additional 15 minutes to give a homogeneous but viscous emulsion. The emulsion was transferred to a polypropylene cup and cured in a laboratory oven at 60 °C for 24 h. The cured monolithic product was then broken into small pieces (approximately $1 \times 1 \times 1$ cm^3) and subjected to Soxhlet extraction with n-butanol as a solvent. The resulting nanoporous geopolymer (base media) pieces free of organics were dried overnight in the lab oven maintained at 120 °C. Complete removal of organics was confirmed by CHN analysis and Infrared spectroscopy (data not shown).

Table 4. Synthetic parameters of the base media.

Sample	Mole fraction of water	K:Al:Si	Oil used	Oil ratio
1	0.68	2:1:2	Canola/Paraffin	50%/50%
2	0.68	2:1:2	Paraffin	100%
3	0.73	3:1:2	Canola	100%
4	0.73	3:1:2	Canola/Paraffin	50%/50%
5	0.68	1:1:1.5	Canola	100%
6	0.68	1:1:1.5	Canola/Paraffin	50%/50%
7	0.68	1:1:1.5	Canola/Paraffin	33%/66%
8	0.68	1:1:1.5	Paraffin	100%

5.2.2. HFO Impregnation (HFO Media)

The produced pieces of base media were ground and sieved into particles of size ranging between 425 to 600 μm (US mesh 40 x 30), which was required by isotherm testing. Then the impregnation of the base media with HFO was carried out through an incipient wetness impregnation technique in the steps: (i) base media was soaked in $FeCl_3 \cdot 6H_2O$ (Alfa Aesar) dissolved in methanol (2.0 *M* solution) for 24 h; (ii) the resulting particles were filtered and were heated at 85 °C in an ammonia/moisture saturated atmosphere for 12 h in order to raise the pH within the pores and therefore induce the precipitation of Fe(III) as hydrous ferric oxide; (iii) precipitation was completed by further heating the particles in an oven maintained at 85 °C for 12 h before drying at 120 °C for 12 h; (iv) the by-products (co-precipitated KCl and NH_4Cl) were removed from the pores of the composite material by thoroughly rinsing with deionized water; (v) the resulting reddish brown particles soaked in Millipore water were ready for subsequent arsenic removal experiments.

5.2.3. Material Characterization

Powder X-ray diffraction (PXRD) patterns of the finely ground samples were collected using a Siemens D5000 diffractometer (Ni-filtered Cu Kα radiation with a wavelength of 1.5406 Å, operated at 40 kV and 40 mA, VANTEC-1 position-sensitive detector) at a scan speed of 2.0 degrees/min and a step size of 0.016 degrees 2θ. The resolution of the VANTEC-1 position-sensitive detector was $2\theta = 0.008$ degrees. Samples for scanning electron microscopy (SEM) were prepared by placing few pieces of the products on a SEM stub using a copper conducting tape. Samples were then gold coated for 100 s and were studied using SEM-XL30 Environmental FEG (FEI) microscope operating at 5 kV. For transmission electron microscopic (TEM) studies, colloidal suspensions of ground samples in ethanol were dried on to copper grids and were studied using JEOL TEM/STEM 2010F operating at 200 kV.

N_2 sorption isotherms were obtained with a Micrometrics ASAP 2020 volumetric adsorption analyzer at 77 K. Samples were degassed at room temperature for 10 h under vacuum until a residual pressure of ≤10 μmHg was reached. Specific surface areas were estimated using Brunauer-Emmett-Teller (BET) equation, in the relative pressure range from 0.06 to 0.2. Pore volumes were calculated from the amount of nitrogen adsorbed at a relative pressure (P/P_o) of 0.99. Pore size distributions were obtained using the Barrett-Joyner-Halenda (BJH) method assuming a cylindrical pore model. Total pore volume of the products was determined by pycnometry with deionized water at 23 ± 2 °C and ambient pressure, whose principle relies on the permeation of water through the open pore network of solid samples.

Fe contents of the HFO impregnated nanoporous geopolymer media were determined by using Thermo Scientific iCAP 6300 inductively coupled plasma-optical emission spectrometer (ICP-OES). Prior to the analysis, solid samples were acid-digested using a CEM MARS 6 microwave reaction system in repeated heating steps at 180 °C for 30 min with sequential addition of required reagents. Specifically, 20 – 30 mg of catalysts were heated in the reactor first with 3 mL of concentrated HCl solution (34 – 37 wt%, ACS), and second with a mixture of 3 mL concentrated HNO_3 (67 – 70 wt%, ACS) and 0.5 mL of HF solution (48 – 51 wt%, ACS). The digests were later quenched with 5 mL of 4.5 wt% H_3BO_3 solution aided by the microwave reactor.

5.2.4. Batch Experiments

The arsenic removal capabilities of the HFO media were carried out using multidimensional approach that encompasses batch reactor experiments, isotherm modeling (Freundlich isotherm model), continuous flow modeling (Pore Surface Diffusion Model (PSDM)) and laboratory scale continuous flow experiments. Preliminary screening and comparison of the maximum arsenic adsorption capacities of all the different media was conducted using batch reactor tests at pH = 7.6 ± 0.3. The pH value was adjusted by adding hydrochloric acid or sodium hydroxide at room temperature. The initial arsenic concentration in this arsenic only model water was $C_0 \approx$ 120 μg/L. The contact time was 72 hours, which was more than sufficient to establish pseudo-equilibrium. Minimum of 8 adsorbent dosages with 15% triplicates, ranging from 0.1 mg/L to 11.6 mg/L, were used to obtain data that could be fitted with the Freundlich isotherm model given by:

$$q = K \times C_e^{1/n} \qquad (9)$$

where q is the adsorption capacity (mg adsorbate/g adsorbent), K is the Freundlich adsorption capacity parameter ((mg adsorbate/g adsorbent) × (L/mg adsorbate)$^{1/n}$), C_e the equilibrium concentration of adsorbate in solution (mg adsorbate/L), and $1/n$ is the Freundlich adsorption intensity parameter (unit less). The Freundlich isotherm model was used to develop the isotherms because it allows for easy assessment of the favorability of the adsorption process and use of its parameters in the Pore Surface Diffusion Model (PSDM), which was used to assess the performance of the media in a full scale packed bed continuous flow configuration.[128] The analysis of arsenic concentration was conducted using Varian Spectra 50B-GTA 110 Graphite Furnace Atomic Absorption Spectrometer. Parameters in **Table 5** describes the water chemistry of NSF 53 Challenge water.[129] The Rapid Small-Scale Column Tests (RSSCT) were designed to mimic a scaled up packed bed reactor.[130] Characteristics of RRSCT and scaled packed bed system are presented in **Table 6**.

Table 5. NSF 53 water matrix used in the tests.

	Ion	Concentration (mg/L)	Form
1	As(V)	0.12	Na_2HAsO_4
2	ClO^{4-}	0.1	$KClO_4$
3	F^-	1.0	NaF
4	NO_3^-	2.0	$NaNO_3$
5	PO_4^{3-}	0.04	$NaH_2PO_4 \cdot H_2O$
6	Dissolved silica	20	$Na_2SiO_3 \cdot 9H_2O$
7	Ca^{2+}	40	$CaCl_2$
8	Mg^{2+}	12	$MgSO_4 \cdot 7H_2O$
9	SO_4^{2-}	50	$MgSO_4 \cdot 7H_2O$

5 m*M* $NaHCO_3$ was used to buffer the water matrix.

Table 6. RSSCT parameters and Scaled Packed Bed system used in experimental work and modeling.

Parameter	RSSCT	Packed bed system
Bed depth (cm)	6	60
Bed diameter (cm)	1.1	50
Bed mass (g)	2.73	56,400
Flow rate (mL/min)	14.6	3016
EBCT (min)	0.391	39.1
Particle radius (mm)	0.05	0.5

5.2.5. Toxicity Characteristic Leaching Procedure

The toxicity characteristic leaching procedure (TCLP) test of arsenic adsorbed solid material was carried out according to the procedure described by the U.S. Environmental Protection Agency (EPA) method 1311.[131] Here, the arsenic adsorbed dry solid material was mixed with the TCLP fluid (sodium acetate plus acetic acid buffer of pH 4.93 ± 0.05 by the 1:20 ratio and agitated (speed, 280 ± 5 rpm) for 18 h at 30 °C using a mechanical shaker. Two samples of spent media from column testing, media **3-Fe**,

were tested to provide duplicate testing validation. Leached arsenic in the filtered TCLP fluid was determined using graphite furnace atomic absorption spectroscopy.

Table 7. Pore properties of the media before and after HFO impregnation along with iron content, zeta potential and arsenic adsorption capacity values.

Sample	BET surface area (m^2/g)	Mesopore volume[a] (cm^3/g)	Mesopore width[b] (nm)	Macropore volume[c] (cm^3/g)	Bulk density[d] (g/cm^3)	Bulk porosity[d] (%)	Fe content[e] (wt %)	Zeta potential	Q100 (µg As/g dry media)	Meso/ Macro pore ratio (%)
	Base media; **HFO media**	Base media; **HFO media**	Base media; **HFO media**							
1-Fe	42; **98**	0.28; **0.24**	26; **12**	1.21	0.69	67	19.2	6.00	268	20
2-Fe	8.0; **171**	0.05; **0.18**	30; **5.0**	1.18	0.73	64	17.4	5.20	559	15
3-Fe	58; **73**	0.80; **0.22**	53; **10**	1.45	0.59	65	20.0	7.40	954	15
4-Fe	50; **298**	0.39; **0.30**	39; **5.0**	1.22	0.65	67	24.2	6.80	295	25
5-Fe	59; **75**	0.38; **0.42**	28; **20**	0.85	0.78	66	14.0	5.50	449	49
6-Fe	75; **234**	0.42; **0.35**	20; **7.0**	0.88	0.81	63	18.4	7.50	467	40
7-Fe	56; **192**	0.43; **0.29**	26; **7.0**	0.96	0.80	62	16.7	6.70	369	30
8-Fe	24; **69**	0.10; **0.11**	19; **6.0**	1.31	0.70	69	19.8	8.20	233	8.1

[a]From the pores with width no larger than 150 nm in the BJH desorption pore distribution.

[b]4(BJH desorption pore volume)/(BET surface area).

[c](Total pore volume determined by pycnometry) − (BJH desorption pore volume).

[d]From total pore volume determined by pycnometry.

[e]From ICP-OES.

5.3. Results and Discussion

5.3.1. Media Characterization

In previous chapters we demonstrated that the hierarchical pore network with co-existing distinctive mesopores and macropores can be introduced into the otherwise dense geopolymeric material by templating with triglyceride oil. We also revealed that the pore characteristics of these hierarchically porous geopolymers can be controlled by

adjusting the synthetic parameters. Briefly, templating with triglyceride oils (such as canola oil) or with oil mixtures whose at least one of the components is a triglyceride that is capable of undergoing saponification reaction with the highly alkaline geopolymer precursor mixture generates both mesopores and macropores in the final product. Whereas, templating with paraffin oil which lacks the ester functional groups to undergo saponification reaction generates only the macropores. Additionally, mesopore volume increases with increasing amount of water without altering the mesopore size. Furthermore, both mesopore volume and mesopore size increases with increasing K/Al ratio between 1.0 and 3.0. In this study, eight different nanoporous geopolymers (media **1** – **8**) were produced to generate different pore size/structure as shown in **Table 7**. Prior to HFO impregnation, the untreated nanoporous geopolymer media **3** and **5** prepared by adding canola oil, or the media **1**, **4**, **6** and **7** prepared by adding a mixture of canola oil and paraffin oil exhibited mesoporosity as well as macroporosity. Mesoporosity can be seen from the N_2 sorption isotherms (**Figure 25a & b**) and BJH desorption pore size distribution curves (**Figure 25c & d**), and the corresponding pore properties are listed in **Table 7**. Isotherms of these base media shown in **Figure 25a & b** resemble type IV isotherm typical of a material having mesopores. The fact that these isotherms do not saturate at partial pressure, $P/P_o \approx 1$ indicates the presence of macropores (pores wider than 50 nm) as well. Presence of broad range of mesopores which extend into the macropore region can be clearly seen in the BJH desorption pore size distribution curves plotted in **Figure 25c & d**. Furthermore, **Figure 26a & b** show SEM images of the base media **3** chosen as a representative example of **1**, **3**, **4**, **5**, **6** and **7**. Co-existence of mesopores and macropores is clearly evident from these SEM images.

The material exhibits discrete spherical pores whose diameter range from about 5 to 40 µm (**Figure 26a**). A closer look in **Figure 26b** revealed that the pore wall separating the spherical pores has a finer structure throughout the matrix indicating the mesoporosity confirmed by N_2 sorption analysis.

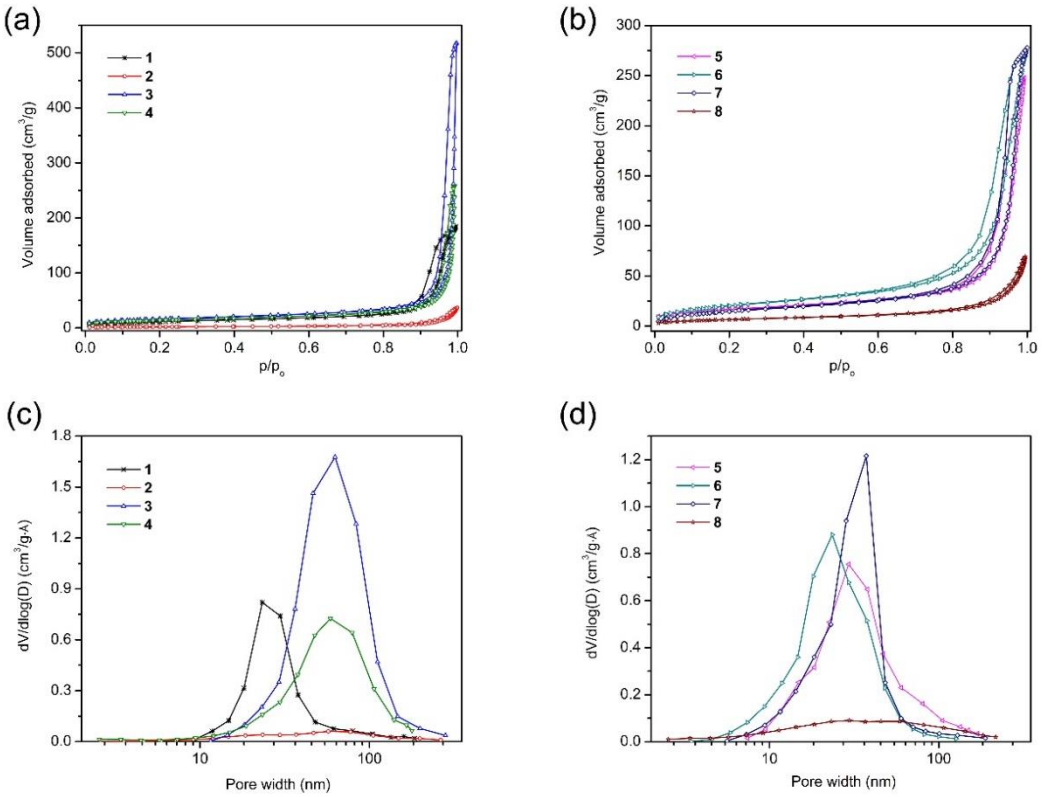

Figure 25. Nitrogen sorption isotherms (a & b) and BJH desorption pore size distribution curves (c & d), respectively, of untreated media **1** – **4** (left) and **5** – **8** (right).

On the other hand, untreated media **2** and **8** prepared by adding solitary paraffin oil exhibits only a macropore network as seen in N_2 sorption isotherm (**Figure 25a & b**) and BJH desorption pore size distribution curves (**Figure 25c & d**). **Figure 26c & d** shows SEM images of the base media **2** as a representative example. Spherical

macropores (20 to 50 µm) are clearly visible from **Figure 26c** but a closer look at the pore walls revealed additional macropores of smaller size (~2 µm) in **Figure 26d**. Transmission electron microscopy (**Figure 28a**) revealed that all the base media without any exception consisted of a gel like nanostructure of the material which is made up of nanoparticles that are strongly fused together at their necks.

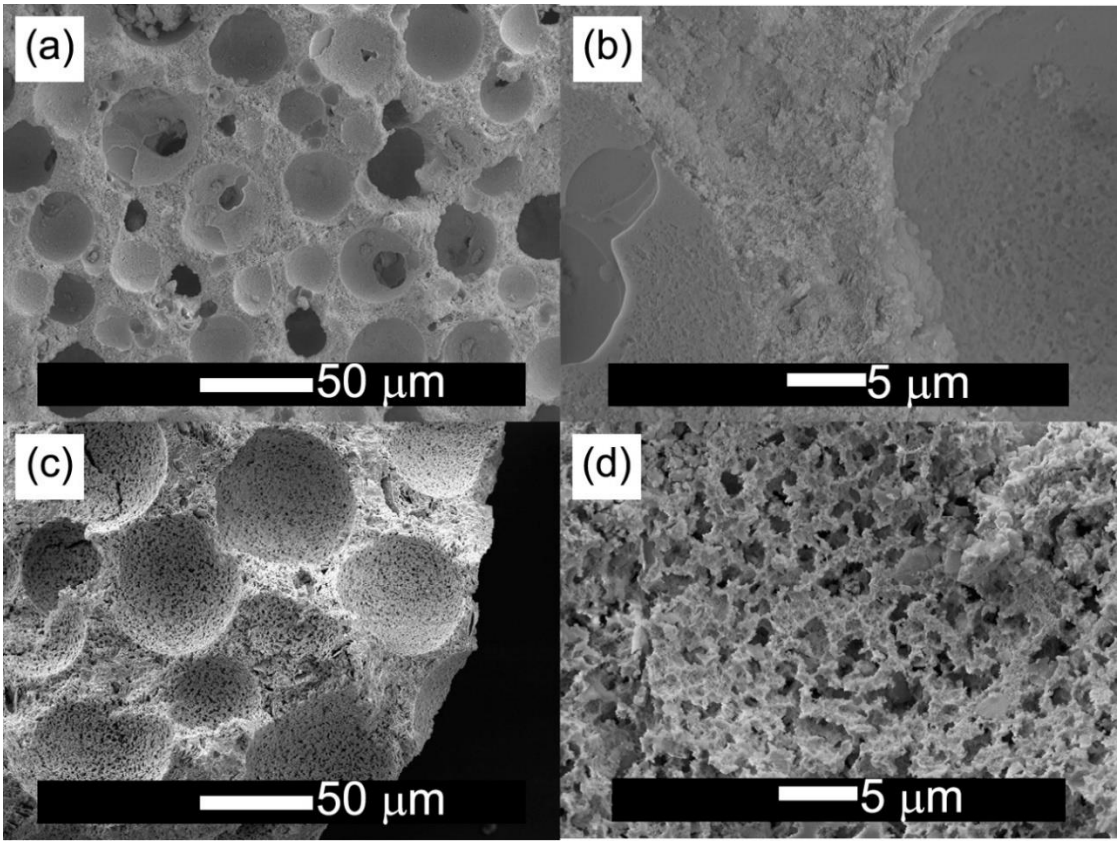

Figure 26. SEM images of untreated media **3** (a & b), and **2** (c & d) as representative examples.

After HFO impregnation, all media had uniform reddish-brown color all over the sample including internal surfaces, which indicates homogeneous impregnation of HFO. Furthermore, all samples exhibited open mesopores and macropores as confirmed by N_2

sorption (**Figure 27**) and scanning electron microscopic studies (data not shown), respectively revealing that the pores are not clogged upon impregnation. BET surface area increased and mesopore diameter decreased for all the media without any exception (**Table 7**), probably due to surface roughening of the pore walls, proving that HFO was successfully impregnated within the mesopores. A similar trend was reported by Bandyopadhyay et al. upon introducing TiO_2 nanoparticles into the pores of mesoporous MCM-48 by wet impregnation method.[132] Regarding to pore volume change after HFO impregnation, pore volume due to previously mesopores decreases but at the same time some of the macropores are reduced in size and start to contribute towards mesopore volume. Therefore, no clear trend in the mesopore volume change was observed. This was clearly noticed in media **2-Fe**, whose mesopore volume increased by more than three-fold from 0.05 cm^3/g to 0.18 cm^3/g upon HFO impregnation rather than decreasing. TEM studies of the media revealed that HFO is present as nanoparticles of approximate diameter of 4 nm (**Figure 28b**), which explains the increment in surface areas upon impregnation. However, it is worth mentioning that the presence of bigger aggregates of HFO, particularly within the larger macropores cannot be ruled out. Furthermore, elemental mapping using STEM (**Figure 28d**) with a spatial resolution of 3 nm showed homogeneously distributed of iron in media 3-Fe.

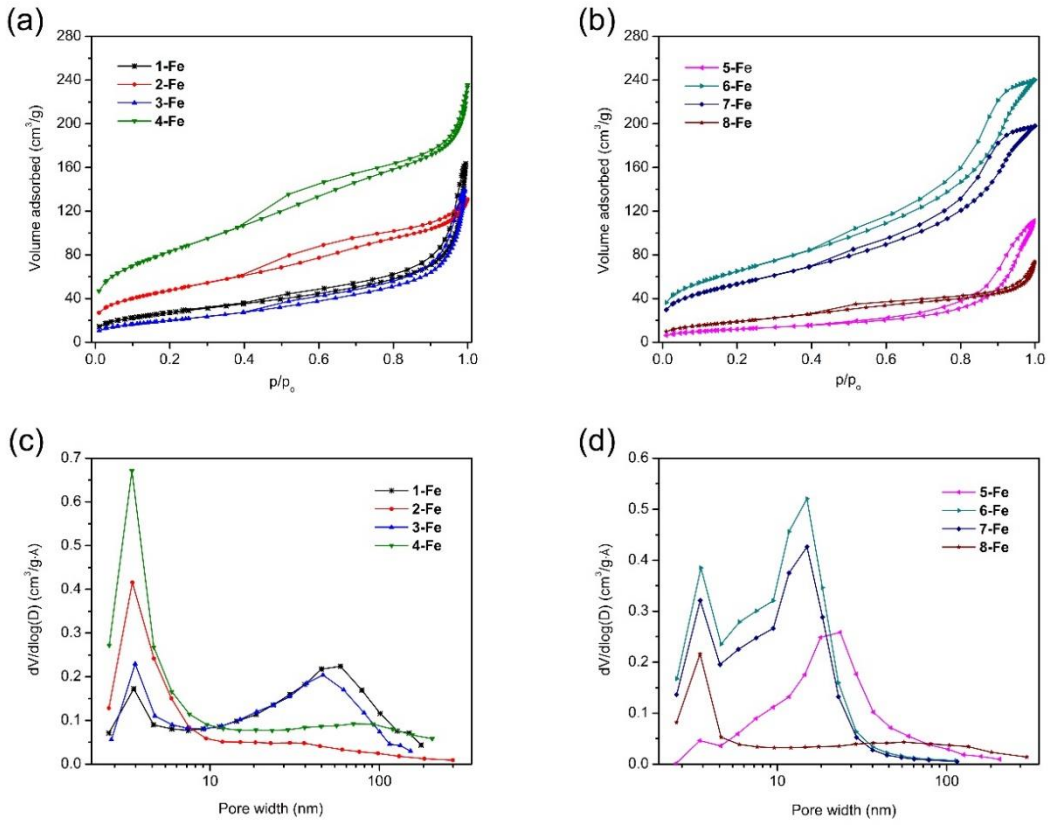

Figure 27. Nitrogen sorption isotherms (a & b) and BJH desorption pore size distribution curves (c & d) of HFO impregnated media **1-Fe** – **4-Fe** (left) and **5-Fe** – **8-Fe** (right).

Figure 29 shows the powder XRD pattern of media **3** before and after impregnation as a representative sample. Powder XRD analysis (**Figure 29**) suggested that the impregnation yielded non-crystalline ferric species (hence amorphous hydrous ferric oxide or simply HFO). The base media themselves were amorphous and the largely featureless "hump" centered at approximately 27° – 30° in 2θ seen in their powder XRD patterns is the unique feature of geopolymers.[133]

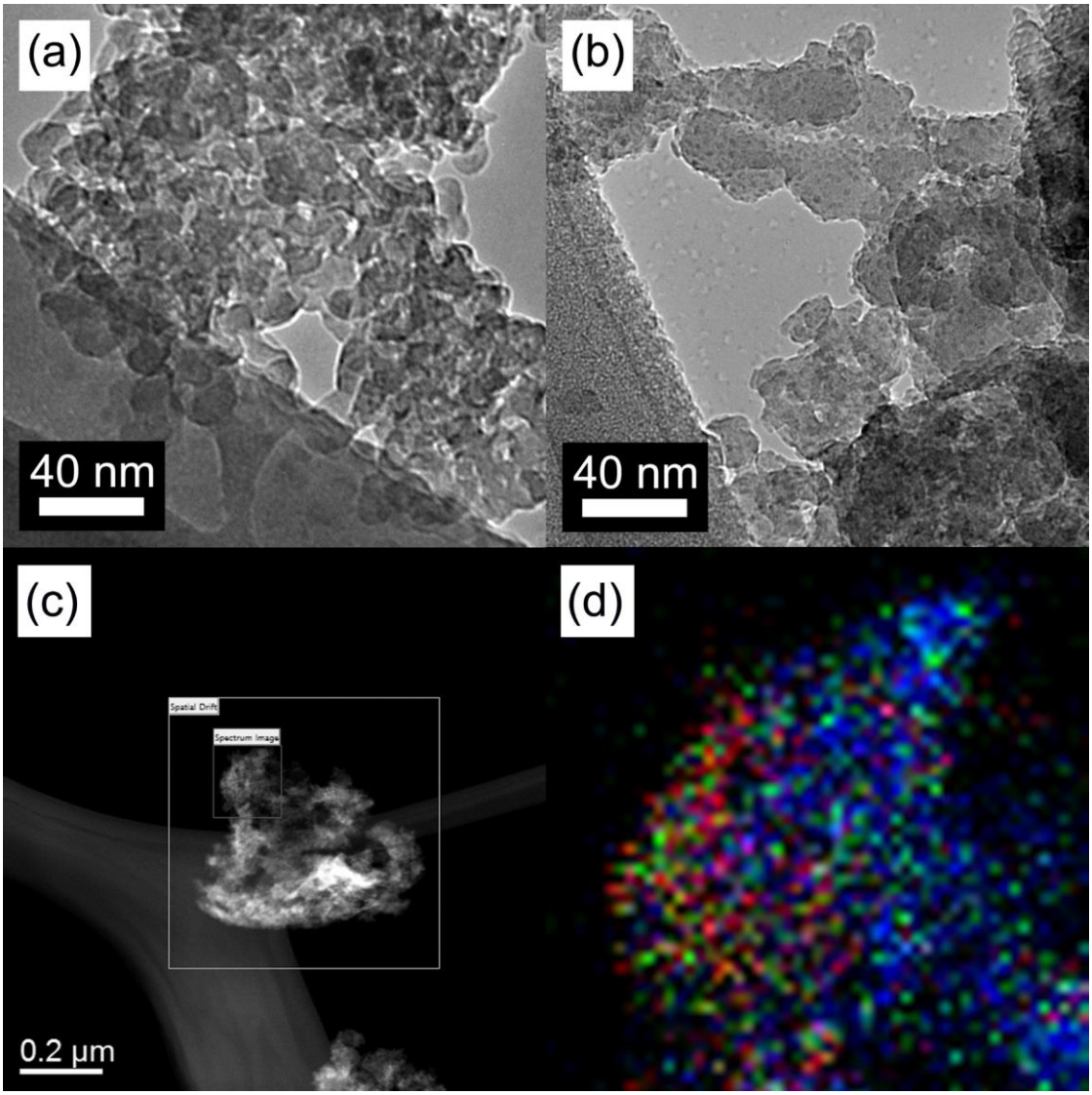

Figure 28. TEM images of untreated media **3** (a) and HFO impregnated media **3-Fe** (b), along with the dark field STEM image of media **3-Fe** (c) and the corresponding elemental mapping image (d). Red represents iron, green represents aluminum, and blue represents silicon.

5.3.2. Evaluation of HFO Media for Arsenic Removal Capabilities

Figure 30a summarizes the isotherms obtained from the batch reactor tests data in arsenic only model water. All media, with exception to SBIR-5, exhibited Freundlich isotherm intensity parameters ranging between 1.1 and 1.3, which suggests that these media may be suitable for treatment of waters exhibiting higher than typical arsenic concentrations. **3-Fe** exhibited highest adsorption capacity, followed by **2-Fe**. The PSDM predictions (**Figure 30b**), obtained at $C_{influent}$ = 120 µg As/L in arsenic only water, show the same trend. **3-Fe** was able to treat about 5 m^3 of water containing 120 µg As/L arsenic per 1 kg of media before effluent concentration of 10 µg As/L (MCL standard for As) was reached. Under the same conditions, **2-Fe** was able to treat only about 2.5 m^3 water/kg media.

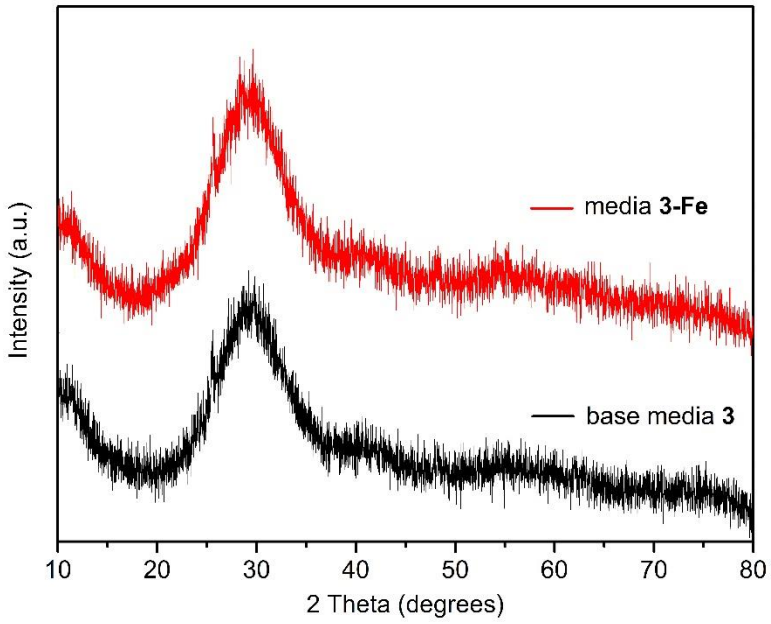

Figure 29. Powder X-ray diffraction patterns of untreated media **3** (black) and HFO impregnated media **3-Fe** (red) as representative examples.

The lower arsenic adsorption capacity of the other media resulted in rapid breakthrough of the media as the adsorption sites located on the outer surface become quickly occupied with arsenic. The gradual increase in the breakthrough curve following the rapid region was not observed for many of the low capacity media suggesting that the available adsorption sites inside the media particles may not be available for adsorption because of pore blocking or simply because their numbers were low. Such gradual breakthrough later in the run is clearly apparent for **3-Fe** as the intraparitcle mass transport becomes the limiting transport mechanism due to diffusion of arsenic ions deeper into the particle to find available and accessible adsorption sites.

Table 8. Freundlich isotherm parameters for **3-Fe**.

Water matrix	Freundlich capacity parameter (K)*	Freundlich intensity parameter (1/n)	R^2	pH
As only water	5.23	1.13	0.989	7.6 ± 0.2
NSF 53 water	3.52	1.12	0.999	7.6 ± 0.2

* $\frac{\frac{\mu g\ As}{g\ Dry\ media}}{\left(\frac{\mu g\ As}{L}\right)^{1/n}}$

Since **3-Fe** exhibited highest arsenic adsorption capacity in the arsenic only model water, it was further tested to assess its performance in NSF 53 challenge model water which is used to surrogate laboratory groundwater for assessing arsenic adsorption of media in realistic conditions. Batch experiments were conducted at the same experimental conditions, except for the change in the model water matrix, to assess the effect of the competing ions (silica and phosphate) onto the arsenic removal performance of the media. **Table 8** summarizes the adsorption isotherms coefficients for **3-Fe** under

equilibrium conditions with and without competing ions. The Freundlich intensity parameter (1/n) did not change when competing ions were introduced (1.13 versus 1.12, respectively), implying that the introduction of competing ions (silica and phosphate) did not affect the adsorption sites energy. The lower Freundlich adsorption coefficient (K) is to be expected for the NSF 53 challenge model water because of the adsorption of the competing ions, which reduce the number available sites for arsenic to adsorb.

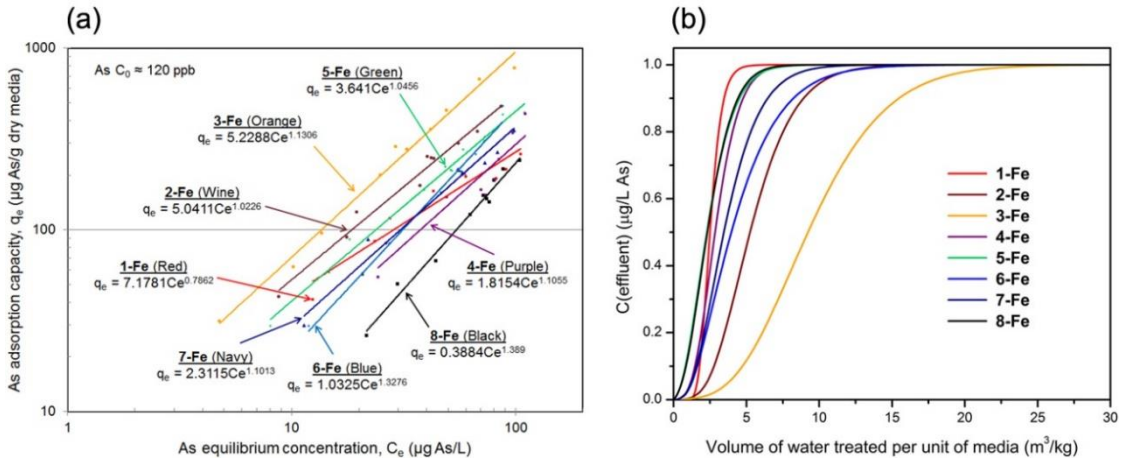

Figure 30. Experimental isotherm data summary (a) and PSDM modelled breakthrough curves (b) of HFO media with arsenic only water matrix.

The breakthrough curve for RSSCT conducted in NSF 53 challenge model water is presented in **Figure 31** together with a breakthrough curve modeled to mimic the same experimental conditions, except in arsenic only model water. The RSSCT was designed to mimic a scaled up packed bed reactor with characteristics presented in **Table 6**. The packed bed reactor provides a same breakthrough curve as the one experimentally obtained. Similarly, the modeled breakthrough curve that is presented for the RSSCT is identical to the modeled breakthrough curve for the packed bed reactor described in **Table 6**. Studies have validated the model for prediction of breakthrough curves in

model waters with no competing ions, so no continuous flow column test were necessary in the arsenic only model water.[128, 130]

Both columns reached 95% breakthrough at approximately the same bed volumes (BV); however, the overall adsorption capacity of the media is lower in NSF 53 challenge model water. In absence of arsenic competing ions, the model predicted that approximately 2,200 BV can be treated before a breakthrough of 10 μgAs/L is reached (C_e/C_0 ~ 0.085). The number of treated BV decreases by almost a factor of 3 as a result of ions with arsenic. So a packed bed reactor, as represented by the RSSCT, can treat about 700 BV before a breakthrough of 10 μg As/L is reached under realistic conditions. This difference in arsenic adsorption capacity is a direct result of the adsorption of competing ions (silica and phosphate). The high silica concentration causes rapid saturation of the available adsorption sites located near the outer layers of the media particle, which is illustrated by the rapid breakthrough in **Figure 30b**. Then, the gradual breakthrough is expected as the only available sites left for the arsenic and competing ions is deeper regions of the particle and the intraparticle mass transport is the limiting mechanism.

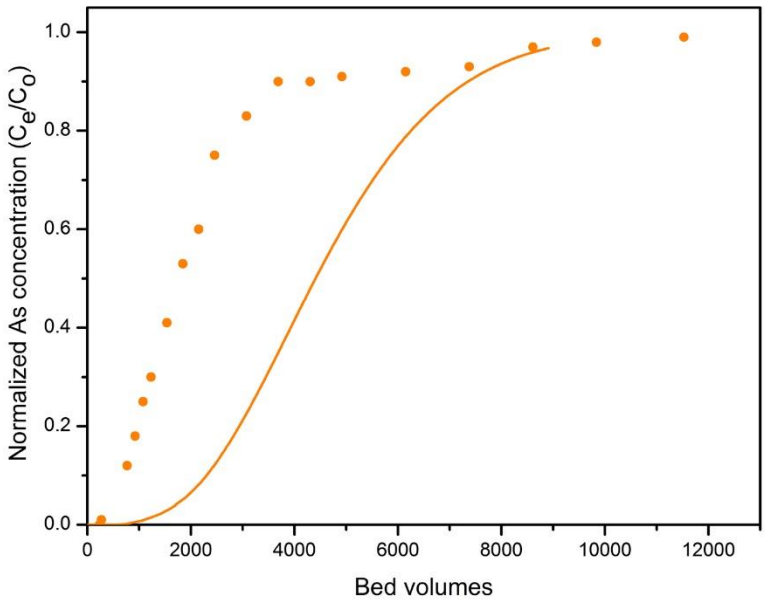

Figure 31. Breakthrough curves for RSSCT with NSF 53 challenge model water (solid circles) and modelled RSSCT with arsenic only water (line) for **3-Fe**.

5.3.3. Evaluating Stability and Disposability Options of Spent Adsorbent

Finally, the stability of the spent adsorbent (spent **3-Fe**) was evaluated and its disposal options were examined by performing a Toxicity Characteristic Leaching Procedure (TCLP). TCLP determines the propensity of the selected media to leach arsenic after landfill disposal. In order for the media not to be labeled as hazardous, as defined in 40 CFR §26.24 Table 1, the waste media must meet the definition of toxicity for waste code D004 (arsenic), exhibiting an arsenic concentration less than 5 mg As/L.[131] Two samples of spent media from column testing, **3-Fe**, were tested to provide duplicate testing validation. **Table 9** outlines the results of the TCLP tests. The arsenic concentration of the filtrate was determined to be about 44 µg As/L, 100x below the EPA limit of 5 mg As/L required to meet the toxicity characteristic. Based on the results, the

spent media does not qualify as hazardous materials and can be disposed as a solid waste. This result is expected based on strong chemical bonding formed between Arsenic species with developed media.

Table 9. Toxicity Characteristic Leaching Procedure (TCLP) results for spent **3-Fe**.

Sample	Initial pH	Final pH	As concentration (μg/L)	Standard deviation
Control	4.93	4.93	Not determined	–
3-Fe trial-1		5.36	44.4	1.49
3-Fe trial-2		5.38	43.3	1.35

TCLP As concentration = 43.9 μg/L

5.4. Conclusions

Composite materials of hierarchically porous geopolymer and HFO having high surface areas and interconnected meso/macropores were successfully developed via wet impregnation for the removal of arsenic from contaminated waters. X-ray studies indicate that HFO introduced into the pores is amorphous in nature and did not seem to alter the structure of the nanoporous geopolymers. All the media have shown arsenic removal capability with varying capacities. Specifically, **3-Fe**, the best performing media which contained ~20 wt% Fe could remove 954 μg of Arsenic per gram of dry media from Arsenic only water matric. The media could also remove Arsenic from NSF 53 challenge model water containing competing ions such as silica and phosphates, signifying that they can also perform with realistic waters. Both in the absence and presence of competing ions, Freundlich isotherm model was followed for batch reactions. The adsorption sites energy seems to remain unaltered while the arsenic removal capacity

appears to be decreased upon introducing competing ions. Moreover, results from RSSCT column testing and modelling showed that **3-Fe** can treat 2,200 bed volumes and about 700 bed volumes before a breakthrough of 10 µg As/L is reached from Arsenic only water matrix and under realistic conditions. Furthermore, TCLP studies have shown that the concentration of arsenic leached out of the spent **3-Fe** media is more than 100 times below the EPA limit of 5 mg As/L classifying it as a non-hazardous material that can be disposed as a solid waste. It is concluded that the new hierarchically porous geopolymer-based composites can be good candidates for cost-effective removal of arsenic from contaminated water under realistic conditions owing to their favourable adsorption capacity and very low leachability. Research efforts to scale-up and further reduce the cost of production processes are undergoing and will be reported elsewhere. This study also opens up the ways to introduce various active species, such as catalysts and adsorbents into the hierarchically porous network of geopolymers and designing many more novel composite materials.

CHAPTER 6

6. DISPERSIBLE GEOPOLYMER PARTICLES

6.1. Introduction

Polymers have changed the world and today they are indispensable in many branches of industry. In the commercial production of plastics, elastomers, man-made fibers, adhesives, and surface coatings, a tremendous variety of polymers are used. Global production of plastics is continuously growing for more than 50 years as a result of new technological advancements in polymer science, and in 2012 it rose to 288 M tonnes – a 2.8% increase compared to 2011.[134] Over the last two decades, particle-filled or reinforced polymer composites have become very attractive owing to their low cost and widespread industrial applications. Polymer composites are manufactured commercially for a variety of applications such as sporting goods, aerospace components, automobiles, etc.[135] Most usage of elastomers would be impractical without reinforcing them with certain fillers, such as carbon blacks (CBs) and structured silica. The reinforcement is often defined as the "improvement in abrasion, tear, cutting and rupture resistance, in stiffness and hardness of vulcanized compounds through the incorporation of finely divided (mineral) particles".[136] An array of powdered minerals can be used as fillers for elastomers but not all provide reinforcement, and essentially two classes of powdered minerals have been found to deliver significant reinforcing capabilities: CBs and high-structure silica.

Minerals used to reinforce the elastomers (i.e., rubber), may have several particle sizes and their reinforcement effect depends strongly on their particle sizes as shown

pictorially in **Figure 32**. Particles bigger than 10,000 nm are generally avoided because they can reduce the performance rather than extend or reinforce. Fillers with particles between 1000 and 10,000 nm are used primarily as diluents and mostly have no significant effect, either positive or negative, on rubber properties. Reinforcement is readily attained with particles smaller than 100 nm but particle structure appears to be a more decisive factor, while particles with intermediate sizes (between 100 – 1000 nm) are semi-reinforcing at best. Two classes of minerals have been found to offer significant reinforcing capabilities to rubber for tire applications, CBs, and silica. High-resolution electron microscopic studies have shown that the primary particles of CBs are solid spheres that are 10 – 90 nm in diameter. Depending on their initial manufacturing process, primary particles of CBs exist in various forms of aggregation. The extent to which aggregates form complex three-dimensional entities is often referred as a "structure".[137] Several of these aggregates may further form loose agglomerates linked by van der Waals interactions.

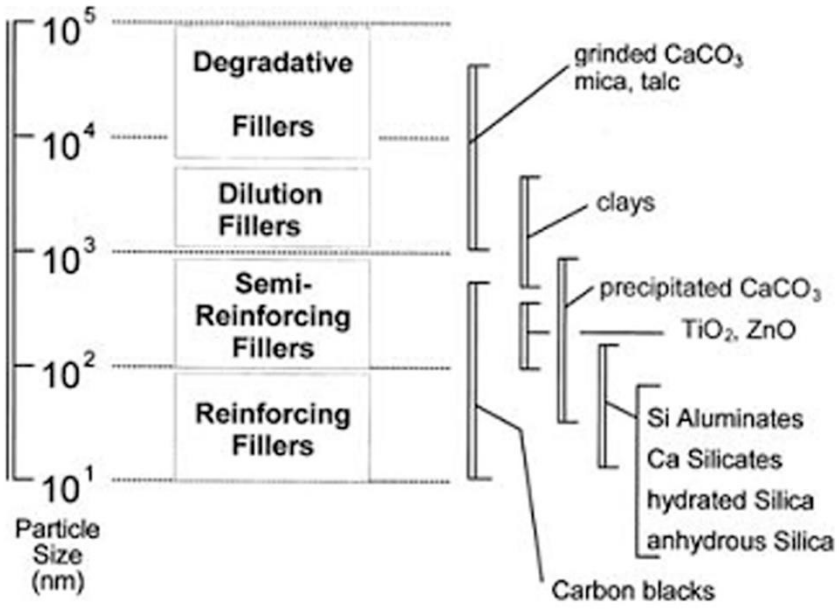

Figure 32. Classification of fillers according to their average particle size, adapted from Mostafa.[138]

A low structure CB may consist fewer than 20 primary particles per aggregate, while a high-structure one may have high number (up to 200) of particles. Reinforcing silica, either precipitated or "fumed" grades, display a similar intricate assemblies, from primary spherical particles that fuse chemically into bigger aggregates, to loose agglomerates linked by weak van der Waals forces. Precipitated silica is most widespread due to the cheaper production costs. It is produced by the controlled neutralization of sodium silicate solution by either concentrated sulfuric, hydrochloric or carbonic acids. Reaction conditions are manipulated according to the particle size requirements.[139] There is no standard classification for reinforcing silica which are in effect distinguished with respect to their specific surface area. At similar reinforcing capabilities, silica specific area are larger than for their CB equivalent, in line with the

irrespective bulk specific gravity, i.e., 2.2 g·cm^{-3} for silica, 1.8 g·cm^{-3} for CB as depicted in **Figure 33**.

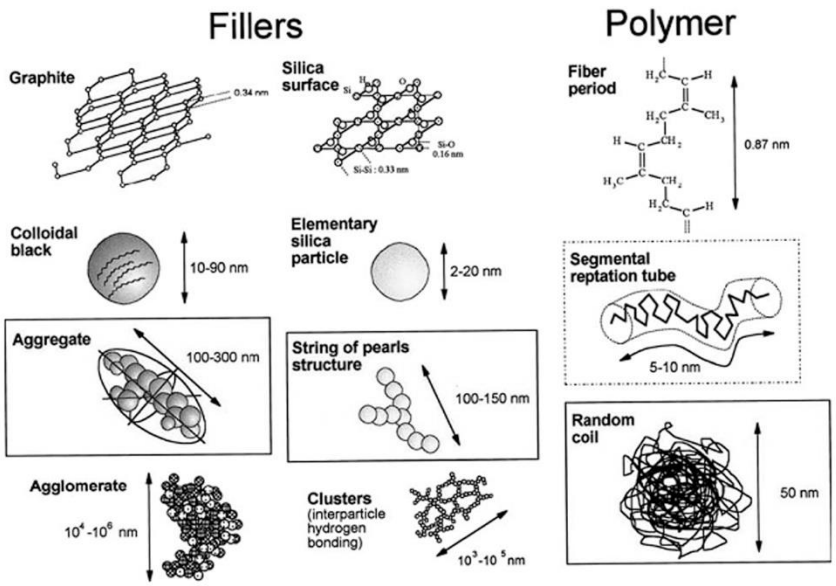

Figure 33. Relevant dimensions in elastomer-filler interactions, adapted from Mostafa.[138]

In addition to the size and structure, the third reinforcing parameter, surface activity of the particles is also an important factor. Surface activity, in the simplest terms means the affinity for and ability to bond to the rubber matrix. In a chemical sense it is correlated to the type and nature of chemical groups present on the surface of the reinforcing particle. In a physical sense, differences in surface energy define the capacity and energy of adsorption. High surface activity along with large surface area and high structure would lead to an intimate elastomer-filler contact. In the case of CBs the filler–polymer interaction is mainly of physical nature, i.e., physisorption. Silica surfaces are hydrophilic, but still react as acids due to the presence of silanol groups and are capable of forming hydrogen bonds. The affinity and activity of silica fillers in relation to

elastomers can be improved by treatment of the silica particle surface with an organosilane via a reaction called silanization. Mercaptosilane is usually the most cost-effective choice and the treatment is typically *in situ*, with the silane added to the mill after the silica and before other additives that can interfere with the silica-silane reaction. As useful as mercaptosilane may be, its odor is generally objectionable. The effective, but less efficient (requires about twice the loading), testrasulfide is the usual alternative, although it comes with other undesired glitches.[140]

CB was the first taken as a reinforcing filler in 1904, and since then carbon black has been a quintessential ingredient in automobile tires and various other rubber products.[140] Introduced in the 1992 by Michelin, silica is one of the key ingredients in energy-saving tires so-called green tires. According to Rhodia, up to now, by using the best grade silicas it is possible to reduce rolling resistance by approximately 25%, bringing about a reduction in fuel consumption and automobile CO_2 emissions by an estimated 5%. Despite the promises and proposed solutions, silica is not yet widely accepted as filler for tire to completely replace the CB as a result of its poor dispersion in rubber, and the economics of synthesizing top grade silica.[141]

In the 1950s and 1960s, amorphous synthetic aluminosilicates were used in large volumes as acid catalysts. Starting from 1970, these products were gradually replaced by more effective zeolites, and research on amorphous aluminosilicates shifted towards other applications such as, intermediates in the production of microporous and ceramic materials, and reinforcing fillers for rubber, ink and paper.[142] Silica and aluminosilicates, when compared with carbon black, offer not only improved mechanical properties as a reinforcing filler in polymer applications, but also the possibility of the reinforced

polymer being translucent or neutral in color. The substitution of Si in the SiO_2 matrix by Al as in synthetic amorphous aluminosilicate, creates a negative charge on the SiO_2 framework with an associated cation (Na^+, for example, as shown in **Figure 34**) being bound to a nearby oxygen atom to maintain the charge neutrality. These negatively charged sites can be beneficially used for surface functionalization with surfactants making aluminosilicate particles organophillic and therefore achieve better dispersion in non-polar polymeric mixtures. Surface modification with surfactant molecules can possibly be carried out in a single pot – during or after the synthesis.

Several grades of synthetic amorphous aluminosilicates have been commercialized by J. M. Huber Corporation under the trademark Zeolex® and Hydrex®. They are generally synthesized at room temperature or slightly elevated temperatures by controlled addition of aluminum sulfate (or alum) solution to a solution of sodium silicate while maintaining the pH between 9 and 12.[43a, b, 46] The precipitated aluminosilicate particles are then separated via filtration or centrifugation and purified by repeated washing. These products are currently accepted as being highly suitable for rubber compounding and paper making in the patent literature. However, one major problem that has been cited is that these products are unstable for long term storage and shipping, and tend to settle down in strata probably due to gelling of the particles. Strategies to increase their long term stability have also been proposed.[43c] Furthermore, these products are often contaminated by co-precipitated sulfates (up to 5 wt %) during the synthesis.

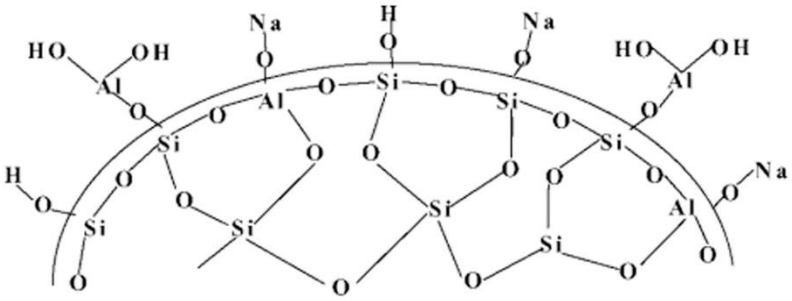

Figure 34. Surface structure of synthetic amorphous sodium aluminosilicate, adapted from Upadyay.[44]

Herein, by modifying the chemistry of geopolymerization, we report a unique synthetic approach to produce highly dispersible aluminosilicate particles – dispersible geopolymer particles or simply DGP here after. Geopolymers are synthetic amorphous aluminosilicates prepared almost all the time in monolithic form but they are innately nanomaterials with a dense xerogel-like microstructure consisting of highly fused three-dimensional network of spherical primary particles of the sizes ranging from 10 – 50 nm, which are in turn made up of disordered corner-sharing AlO_4 and SiO_4 tetrahedra.[27] The synthesis of geopolymers starts with a highly concentrated, viscous aluminosilicate precursor solution (called "geopolymer resin") with an alkali concentration over 10 *M* and a mole fraction of water less than 0.7. Heating the resin gently at an ambient conditions results in hard monolithic geopolymer materials. The amount of alkali (NaOH) used is equal in mole number to that of aluminum (i.e. Na/Al = 1) such that charge neutrality is maintained in the final products. By using excess amount of water (mole fraction of water = 0.73) and alkali (Na/Al =3) we were able to prevent the extensive fusing of primary geopolymer particles and therefore produce DGP which are structurally similar to CBs and structured silica. In this work, the structure and

dispersibility of DGP are investigated and the results are compared and contrasted with CBs, reinforcing structured-silica and commercial aluminosilicates, namely, Zeolex® and Hydrex®.

Table 10. Selected properties of dispersible geopolymer particles obtained from various synthetic conditions.

Sample	SSA_{BET}[a] (m^2/g)	SSA_{micro}[b] (m^2/g)	SSA_{ext}[c] (m^2/g)	V_{total}[d] (cm^3/g)	V_{micro}[b] (cm^3/g)	V_{meso}[e] (cm^3/g)	Average Pore Size[f] (nm)	PXRD phase	Average Particle size[h] (nm)
DGP-W									
Oven dried	53	7	46	0.22	0.003	0.22	17	Amorphous	54
Freeze dried	60	9	51	0.22	0.004	0.22	14	Amorphous	48
DGP-A									
Oven dried	101	5	96	0.37	0.001	0.37	16	Amorphous	28
Freeze dried	148	18	130	0.40	0.007	0.39	11	Amorphous	19
Z12-A (freeze dried)	340	108	231	0.58	0.05	0.53	7	Amorphous + FAU (16 %)[g]	–
Z18-A (freeze dried)	392	207	185	0.68	0.10	0.58	7	Amorphous + FAU (31 %)[g]	–
Z24-A (freeze dried)	431	236	196	0.70	0.11	0.59	7	Amorphous + FAU (36 %)[g]	–

[a]Pressure range P/Po = 0.05 – 0.20.

[b]t-plot method in the thickness range of 0.35 nm to 0.50 nm.

[c]$SSA_{BET} - SSA_{micro}$.

[d]Single point desorption nearest $P/P_o = 0.98$.

[e]$V_{total} - V_{micro}$.

[f]4(BJH desorption pore volume)/(BET surface area).

[g]Determined from the micropore surface area with respect to 13X.

[h]Average size = $6000/(SSA_{BET} \times \rho)$, where $\rho = 2.1$ g/cm^3 is the density determined by pycnometry.

6.2. Experimental

6.2.1. Synthesis of DGP (Dispersible Geopolymer Particles)

Deionized water was used throughout the synthesis and purification. In a typical synthesis, 9.114 g of NaOH pellets (Reagent grade, ≥ 98%, Sigma Aldrich, Product# S5881, Lot# SLBH8376V) and 23.411 g of water glass (~62.9 wt% H_2O, 10.6 % Na_2O, 26.5 % SiO_2; Reagent grade, Sigma Aldrich, Product# 338443, Lot# MKBH9050V) were dissolved in 16.382 g of water in a polypropylene beaker. Once cooled down, 11.467 g of metakaolin (MetaMax® from BASF, Lot# 10408G023)[106] with average particle size of 1.3 μm was slowly added into the solution while stirring. The resulting mixture was homogenized with a mechanical mixer (IKA® RW 60 digital mixer) at 800 rpm for about 40 min to obtain a visually homogeneous and free flowing resin ("geopolymer resin") with the following final molar composition:

$3.0Na_2O : 1.0Al_2O_3 : 4.0SiO_2 : 32.4H_2O$

The geopolymer resins were poured into 50 ml ultrahigh performance polypropylene centrifuge tubes leaving a headspace of 10 to 15 ml and after tightly closed with lids, the tubes were placed in a laboratory oven at 60 °C for an appropriate durations. Samples heated at 60 °C for 6, 12, 18 and 24 h are denoted as DGP, Z12, Z18 and Z24, respectively. After heating, the loosely aggregated powder products were dispersed in deionized water via homogenization at 6000 rpm (IKA® T25 Digital ULTRA-TURRAX® homogenizer) for about 10 min to give a homogeneous dispersion with a consistency close to milk. It was noticed that the products were ultrafine particles (nanoparticles) which could not be isolated via simple vacuum filtration.

For products which were purified by repeated washing with water, product dispersions in water were purified and isolated by repeated centrifugation (4000 rpm or 2156 RCF for 10 min) and redispersion in water until the pH decreased to about 8. For the products those were purified with an acid wash, ~2 *M* hydrochloric acid (34 – 37 wt%, ACS grade, BDH) solution was added in a drop wise manner while stirring with a magnetic stirrer until the pH of the dispersions decreased to about 8. As the pH approached close to 8, solid particles started to precipitate. The solid particles were then isolated via centrifugation (4000 rpm or 2156 RCF for 5 min) and were washed thrice with repeated centrifugation and redispersion in fresh deionized water to get rid of any inorganic salts present, NaCl, for example. Water washed and acid washed samples are labelled with their three letter codes as described in previous section followed by –W and –A, respectively. For example, DGP-W represents a samples prepared by heating at 60 °C for 6 h and purified via water washing, and Z12-A denotes a sample prepared by heating at 60 °C for 12 h and purified via acid washing. The product precipitates were either (1) stored wet at room temperature in tightly sealed polypropylene tubes with added water so that the surface of the products do not dry out upon storing for long periods of time, or (2) oven dried in a laboratory oven at 95 °C overnight, or 3) freeze dried over two days – and were stored in sealed glass vials at room temperature for further analysis.

6.2.2. Materials Characterization

Powder X-ray diffraction (PXRD) patterns of the finely ground samples were collected using a Siemens D5000 X-ray Diffractometer (Ni-filtered Cu Kα radiation with a wavelength of 1.5406 Å, operated at 40 kV and 30 mA, VANTEC-1 position-sensitive

detector) at a scan speed of 2.0 degrees/min and a step size of 0.016 degrees 2θ. The resolution of the VANTEC-1 position-sensitive detector was $2\theta = 0.008$ degrees.

Scanning Electron Microscopy (SEM) imaging of powdered samples was performed with a SEM-XL30 Environmental FEG (FEI) microscope. The analysis was performed with 15 kV acceleration voltage and a spot size of 3. For SEM, finely ground dried sample powders were sprinkled on to the SEM stub affixed with copper conducting tape and the samples were then gold coated for 75 s right before imaging.

Transmission Electron Microscopy (TEM) imaging was performed on a JEOL TEM/STEM 2010F (Schottky Field Emission source, accelerating voltage 200 kV). For TEM the dried powders were quickly sprinkled on to the copper grid covered with a holey carbon film right before sample loading.

Brunauer-Emmett-Teller (BET) surface areas were estimated with a Micrometrics ASAP 2020 volumetric adsorption analyzer with nitrogen as the adsorbate at 77 K. Prior to the analysis, samples (about 500 mg) were degassed at 250 °C for at least 12 h under vacuum until a residual pressure of ≤10 μmHg was reached. The specific area (SSA_{BET}) was calculated according to the BET equation, using nitrogen adsorption isotherms in the relative pressure range from 0.01 to 0.2.[143] Specific surface area of micropores (SSA_{micro}) and the micropore volume (V_{micro}) are calculated by applying t-plot method in the thickness range of 0.35 nm to 0.50 nm and, Harkins and Jura thickness equation. External surface area (SSA_{ext}) is estimated as the difference between specific surface areas obtained from BET equation and t-plot method. For the calculation of mesopore size distribution, desorption branch was considered and the total pore volume (V_{total}) was obtained from the amount of nitrogen adsorbed at a relative pressure (P/P_o) of 0.99,

assuming complete pore saturation. Mesopore size distributions were obtained using the Barrett-Joyner-Halenda (BJH) method assuming a cylindrical pore model.[144]

Bulk densities of samples were measured by means of pycnometry using water as a solvent. The load and temperature effect on the pore properties of selected products were measured on circular pellets. The pellets for the measurements were prepared by pressing about 0.2 g of powdered samples in a 10 mm die using a hydraulic press under a pressure of 90,000 psi or 620 MPa. The circular pellets were then heated in air at desired temperature for 6 h.

Elemental compositions and atomic ratios of silicon to aluminum (Si/Al) of the dried products were determined by using Thermo Scientific iCAP 6300 inductively coupled plasma-optical emission spectrometer (ICP-OES). Prior to the analysis, solid samples were acid-digested using a CEM MARS 6 microwave reaction system in repeated heating steps at 180 °C for 30 min with sequential addition of required reagents. Specifically, 20 – 30 mg of catalysts were heated in the reactor first with 3 mL of concentrated HCl solution (34 – 37 wt%, ACS), and second with a mixture of 3 mL concentrated HNO_3 (67 – 70 wt%, ACS) and 0.5 mL of HF solution (48 – 51 wt%, ACS). The digests were later quenched with 5 mL of 4.5 wt% H_3BO_3 solution aided by the microwave reactor.

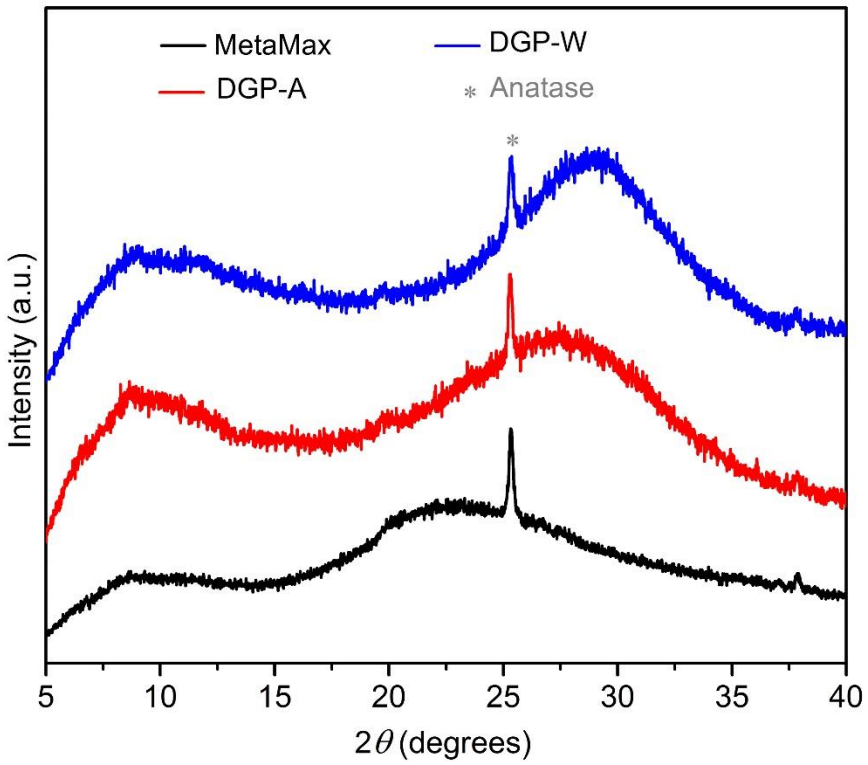

Figure 35. Stacked powder X-ray diffraction patterns of MetaMax® (black) compared with samples DGP-A (red) and DGP-W (blue). Small impurity of anatase (*) (TiO_2 at ~25.3 degrees 2θ; PDF card # 00-021-1272) is present in all three samples.

Dynamic Light Scattering (DLS) and zeta potential measurements of the sample dispersions in deionized water at 25 °C were performed on Malvern Nano-ZS instrument equipped with a multi-purpose titrator (MPT-2). The wavelength of the laser was 633 nm and the refractive index of the material was chosen to be 1.47. DLS measurements were performed after diluting the products to ~50 ppm with water. Before measurement, sample dispersions were prepared by hand shaking for 10 sec followed by ultrasonicating for 5 min. Titrations were performed on ~50 ppm sample dispersions between a pH ranges of ~12.0 to ~3.5 – lower than which the aluminosilicate particles may dissolve.

Freshly prepared solutions of NaOH (0.01 *M*) and HCl (0.01 *M*) were fed into the MPT-2 titrator which adjusted the pH accurately.

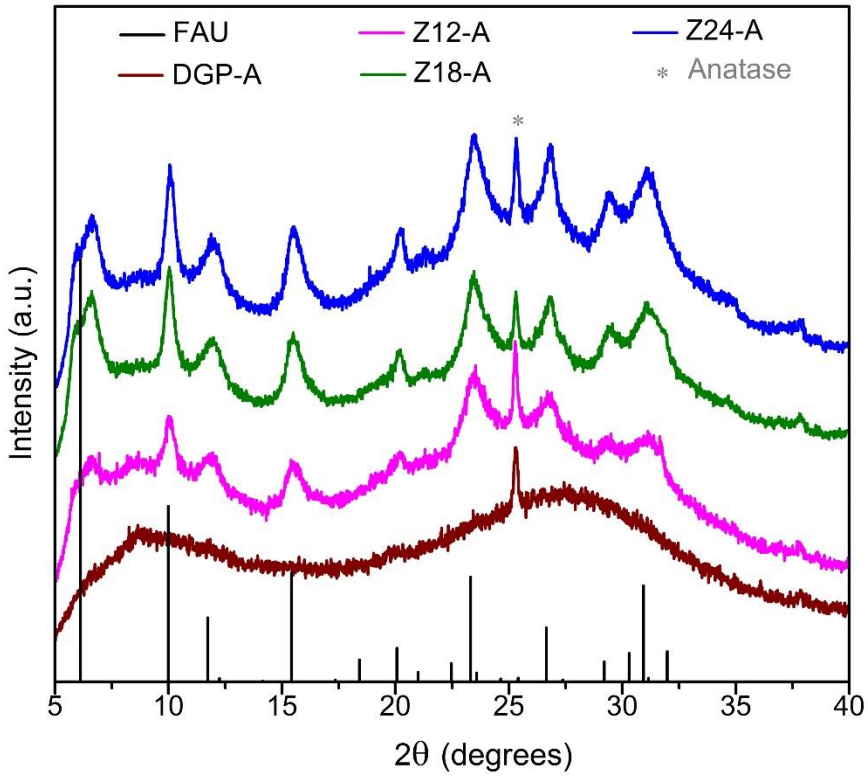

Figure 36. Stacked powder X-ray diffraction patterns of samples DGP-A, Z12-A, Z18-A and Z24-A (bottom to top) compared with the simulated powder pattern of NaX zeolite with faujasite (FAU) structure and (*) anatase (TiO_2 at ~25.3 degrees 2θ; PDF card # 00-021-1272).

6.3. Results and Discussion

Powder X-ray diffraction analysis (**Figure 35**) confirmed that MetaMax®, the precursor used in the synthesis is amorphous with a small crystalline peak at ~25.3 degrees 2θ corresponding to TiO_2 (anatase; PDF card # 00-021-1272) which is present as a small impurity. As seen in **Figure 35**, the amorphous hallow of MetaMax® centered at

~22 degrees 2θ is replaced by a new amorphous hump centered at 28 – 30 degrees 2θ upon activating with NaOH and sodium silicate, and heating at 60 °C for 6 hours in the case of samples DGP-W and DGP-A. This new amorphous hump is a signature of a powder X-ray pattern of geopolymeric sample. It is clear from the powder X-ray analysis of DGP-W and DGP-A samples that different methods of purification (water wash versus acid wash) had no effect on the crystallinity of the final products. Upon increasing the heating time to 12 hours, crystalline peaks corresponding to zeolite with FAU (faujasite) structure started to appear (**Figure 36**) demonstrating that the onset of FAU crystallization occurred between 6 and 12 hours of heating. The percent crystallinity determined from the micropore surface area with respect to 13X (a commercial FAU obtained from Sigma-Aldrich) was 16% after 12 hours. Further increase in the heating time to 18 and 24 hours caused increment in the crystallinity to 31 and 36%, respectively at the expense of some of the amorphous material. The FAU peaks seen in **Figure 36** are rather broad signifying the presence of nanocrystals. Beyond 24 hours the crystallinity corresponding to FAU did not increase, however a competing SOD (sodalite) phase started to appear. Heating durations at 60 °C beyond 24 hours is outside the scope of the current chapter but will be discussed in depth in the following chapter. Separately, in an attempt to reduce the synthesis period, heating at 90 °C was attempted but crystalline zeolitic phases such as SOD (sodalite), LTA (Linde Type A) and FAU (Faujasite) appeared as early as one hour. From these initial studies it was clear that heating temperature of 60 °C and heating duration of 6 hours are appropriate to produce amorphous geopolymer particles i.e. DGP. Since the main focus of this chapter is

amorphous geopolymer particles, samples DGP-W and DGP-A were further analyzed for their morphologies, dispersibility, and fragility under external pressure.

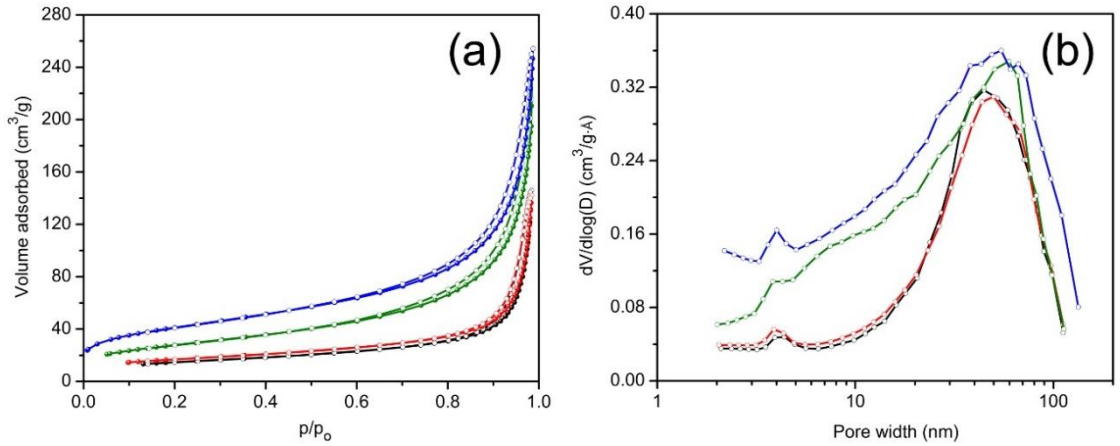

Figure 37. N_2 sorption isotherms (a) and BJH pore size distributions (b) of the samples prepared from geopolymer resin heated for 6 h at 60 °C, namely, DGP-A-freeze dried (blue), DGP-A-oven dried (olive), DGP-W-freeze dried (red) and DGP-A-oven dried (black). For all samples, solid spheres and open circles represent adsorption and desorption branches, respectively.

Figure 37a shows the nitrogen sorption isotherms of samples prepared at 60 °C, namely, DGP-W and DGP-A after both oven drying and freeze drying. All samples exhibited type IV isotherms, typical of materials having mesopores. Insufficient N_2 uptake at low partial pressures ruled out the presence of any micropores or zeolitic phases in other words, which is consistent with PXRD analysis. Isotherms did not show any signs of saturation at a partial pressure, $P/P_o \approx 1.0$, indicating the presence of macropores as well, in addition to mesopores. Furthermore, presence of type H1 hysteresis at high relative pressures ($P/P_o \geq 0.6$) and absence of saturation at a partial pressure, $P/P_o \approx 1$, likewise represented the presence of mesopores and macropores, respectively.[145]

Presence of a range of mesopores which extend into the macropore region is clearly seen from their BJH desorption pore size distribution curves shown in **Figure 37b**. BET surface areas of these samples (listed in **Table 10**) ranged from 53 to 148 m^2/g indicating that they are nanoparticulate. TEM analysis (**Figure 38**) revealed that the primary particles smaller than 100 nm are aggregated to form bigger grape-like bundled particles that are several hundreds of nanometers. Morphologically these grape-like bundles are similar to carbon blacks with high structure.[146] Furthermore, the spaces between the primary particles seen in TEM correspond well with the pore sizes determined by BJH analysis making it clear that the meso/macro-pores revealed by N_2 sorption analysis are inter-particle voids rather than intra-particulate pores. Inter-particle void volume ranging from 0.22 – 0.39 cm^3/g was observed while the bulk density was determined to be 2.1 g/cm^3. This means that ~46 – 82% of the aggregate volume is empty space, i.e. the solid fraction of the primary aggregates is quite small (~0.54 – 0.18). Relatively big pores (>10 nm) coupled with large void volumes exhibited by the primary aggregates makes these ideally suited as nano-fillers for polymers and paper industry as well as reinforcing rubber. The SEM analysis (**Figure 39a & b**) showed that the aggregates are further condensed into bigger micron-sized agglomerates when samples are dried into powders. It is noteworthy that the size of these agglomerates is much smaller in comparison to those observed in the case of Hydrex® (**Figure 39c**), an aluminosilicate commercialized by J. M. Huber Corporation.[147]

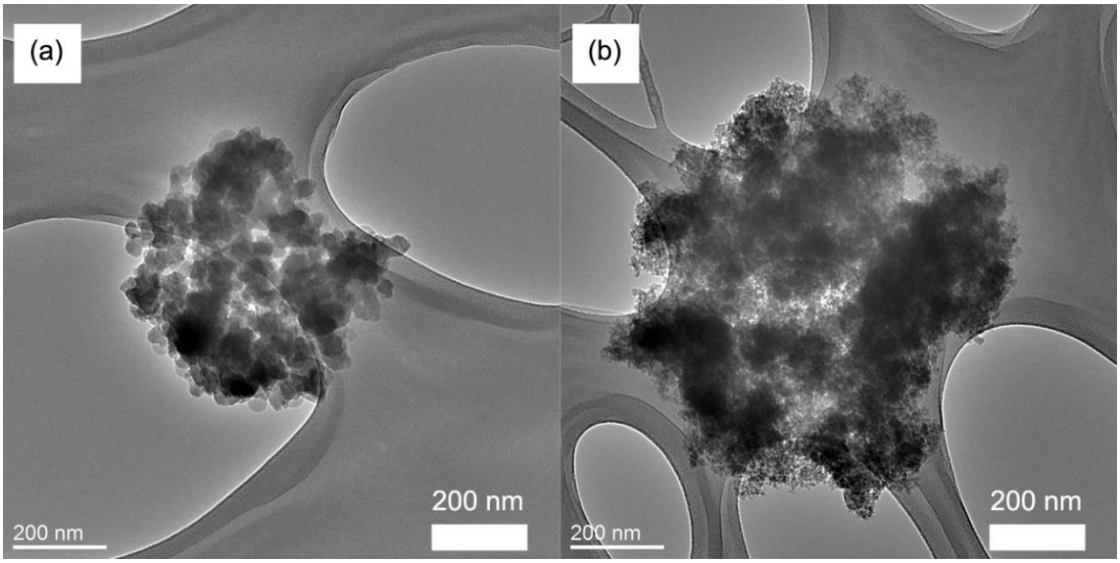

Figure 38. TEM images of amorphous aluminosilicate samples prepared at 60 °C for 6 hours, 6h-W (a) and 6h-A (b).

Additionally, it can be seen from **Table 10** that the BET surface areas, and to a lesser extent BJH pore volumes of oven dried samples of both DGP-W and DGP-A are smaller than freeze dried samples because aggregation/agglomeration/particle-fusion is more severe when liquid water is driven off via evaporation at high temperatures in a conventional oven as opposed to removal of frozen water by sublimation and desorption under vacuum in the case of freeze drying. Although two to three times more expensive than traditional drying processes, freeze drying is an industrial process used for drying biomolecules, food, drugs, nanoparticles, etc., where minimal structural distortion upon drying is desired.[148]

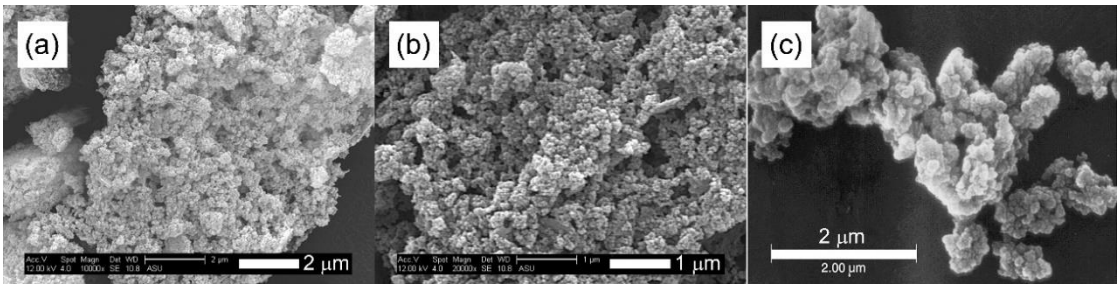

Figure 39. SEM micrographs of DGP-A (a & b), and commercial aluminosilicate, Hydrex® (c), modified from Laine.[147]

Moreover, the average particle sizes of DGP-W calculated from BET surface areas (listed in **Table 10**) is in good agreement with those revealed by TEM imaging (**Figure 40a, c & e**). Whereas, there is a disagreement between the particle sizes obtained from BET and TEM for DGP-A. Closer look at the TEM images of DGP-A shown in **Figure 40b, d & f** revealed that the grape-like aggregates consisted of primary particles with two different size ranges, i.e. ~50 – 60 nm sized bigger particles along with ~15 – 20 nm sized smaller particles. For such an inhomogeneous samples discrepancy between BET and TEM is expected since BET provides the average size of all the particles put together. Reasonably, particle size obtained from BET (19 nm) is in between the bigger and smaller particles. Elemental analysis of both DGP-W and DGP-A using ICP-AES determined their Si/Al ratio to be very close to unity confirming the successful removal of excess Na^+ ions upon purification. On the other hand, Si/Al ratio of water washed DGP-W and acid washed DGP-A samples was 1.33 and 1.75, respectively, both lower than the nominal ratio of 2.0. It is speculated here that only ~2/3rd of the nominal silica gets incorporated into the geopolymer primary particles and the rest is present most likely in the form of dissolved silicate and gets washed away

gradually during the repeated water washing owing to the very high alkalinity of the mother liquors. Since geopolymers are stable in basic solutions, it is presumed that geopolymer particles resist dissolution during purification and only unincorporated silica is preferentially dissolved and washed away. On the contrary, in the case of DGP-A, pH of the dispersion was first dropped to ~8, at which point unreacted silicates would precipitate out possibly as precipitated silica,[149] before repeated washing with water was performed. At pH < 10, solubility of silica is known to be drastically reduced, which probably led to inefficient removal of unincorporated silica.[150] It is also reminded that commercial precipitated silica is produced by the controlled neutralization of sodium silicate solution by either concentrated sulfuric, hydrochloric or carbonic acids. Therefore, due to the higher Si/Al ratio and presence of additional smaller ~15 – 20 nm sized particles in DGP-A when compared with 6h-W, it can be speculated that the smaller (~15 – 20 nm) particles are precipitated silica. Although not performed, Electron Energy Loss Spectroscopy (EELS) in conjugation with imaging in the Scanning Tunneling Electron Microscopy (STEM) would be one appropriate analytical technique to validate this hypothesis.

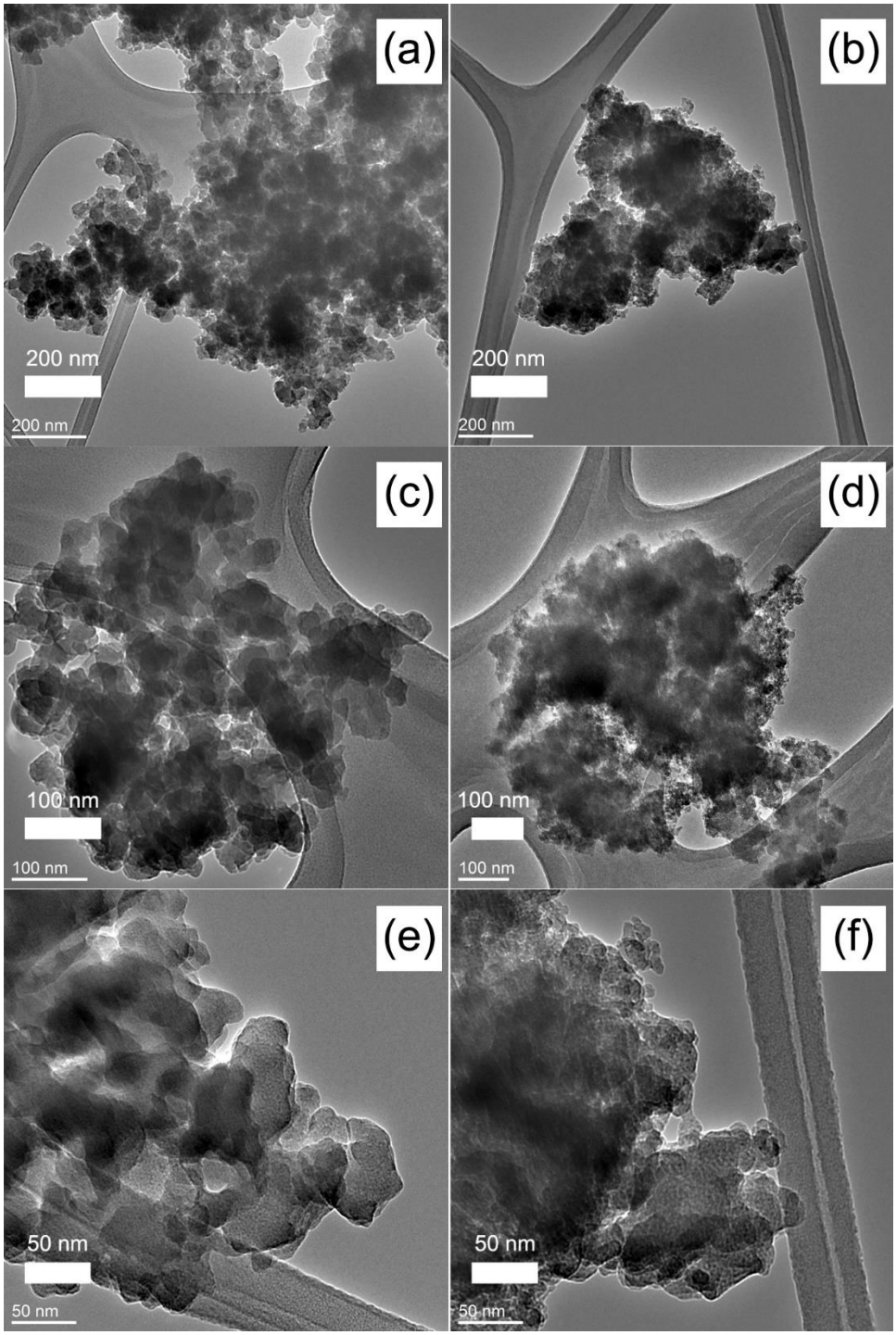

Figure 40. TEM images of freeze dried samples DGP-W (a, c & e) and DGP-A (b, d & f) with increasing magnification from top to bottom.

The solid content of the paste like, non-fluidic products (DGP-W and DGP-A) obtained upon purification and centrifugation was ~22 wt% with rest being water. Even after long term storage, samples could be readily re-dispersed into fluidic dispersions upon dilution with deionized water (say 10 wt%) and stirring by hand with a metal spatula for approximately 20 – 35 sec, followed by manual agitation for further 15 sec. This observation demonstrates that DGP particles are stable with long shelf-life and do not gel upon long term storage, unlike Zeolex® and Hydrex® aluminosilicate particles.[43c] **Figure 41** shows the particle size distribution of ~50 ppm dispersion of DGP-W after 10 min of ultrasonication to break up the loose agglomerates. Single peaks with rather narrow distributions were observed. In addition, resemblance of size distribution curves by intensity (**Figure 41a**) and by volume (**Figure 41b**) strongly indicate that the bigger particles (seen under SEM) do not exist even in scarcity. This is because size distribution by volume is much more sensitive to the presence of even a few bigger particles than does the size distribution by number. The average particle size from the peaks was calculated to be 399 ± 59 nm with a FWHM (full-width at half maxima) of 142 ± 33 nm. Average particle size calculated from DLS measurements corresponds very well with the sizes of grape-like bundles observed under TEM (**Figure 40b**). SEM, TEM and DLS results strongly suggest that micron-sized particles that exist in the powder form are loose agglomerates that readily break-up into finer aggregates (100's of nm) upon dispersing the powders in water. The aggregates are in turn made-up of strongly glued primary particles (50 – 60 nm) that could not be broken even after ultrasonication.

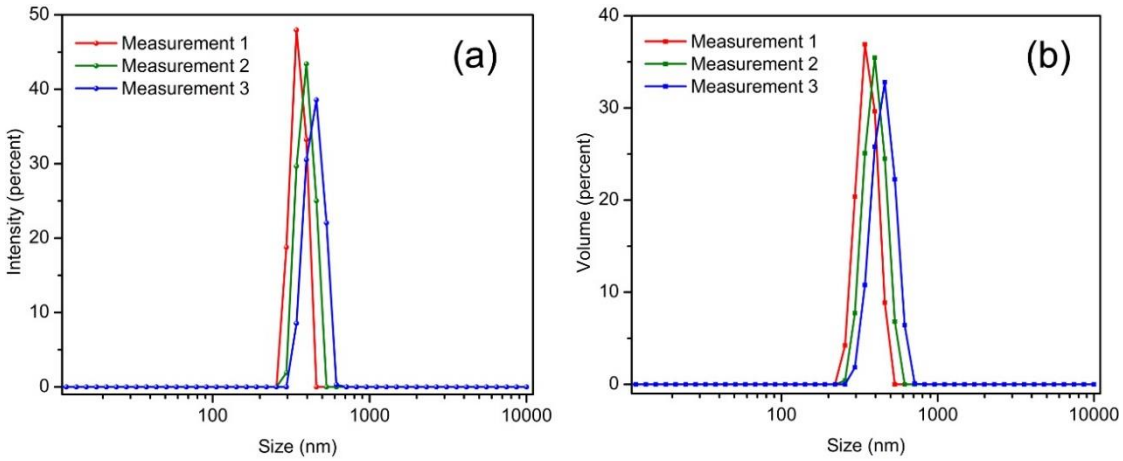

Figure 41. Particle size distribution curves of DGP-W sample by intensity (a) and volume (b). Measurements were repeated 3 times in succession.

In addition to exhibiting good dispersibility with a narrow particle size distribution at near neutral conditions, it is also very important for the particles to be stable under acidic and basic conditions. In order to evaluate the behavior of DGP particles under acidic and basic conditions, both zeta potential and particle sizes of DGP-W sample were monitored as a function of pH, as shown in **Figure 42a**. Zeta potential of DGP-W remained highly negative (absolute value > 40 mV) and the particle sizes remained unaffected (320 ± 31 nm) between the pH range of 12.0 – 5.7 demonstrating that the particles are stable in this pH region and do not undergo aggregation and/or agglomeration. The gradual decrement in the zeta potential down to a pH value of 4.0 which is also accompanied by a steady increase in the particle size to a maximum of 1091 ± 81 nm at pH = 4.0 suggests aggregation/agglomeration in this region. Unusual trend in both zeta potential and particle sizes below pH 4.0 could be due to the fact that aluminosilicates are known to undergo dissolution under exceedingly acidic conditions. A similar, if not exact trend in zeta potential values is observed for aluminosilicate

modified silica sols as well.[151] On the other hand, zeta potential of silica progressively decreases in the entire pH region of 10.0 to 3.0 signifying their instability compared to aluminosilicates (**Figure 42b**).

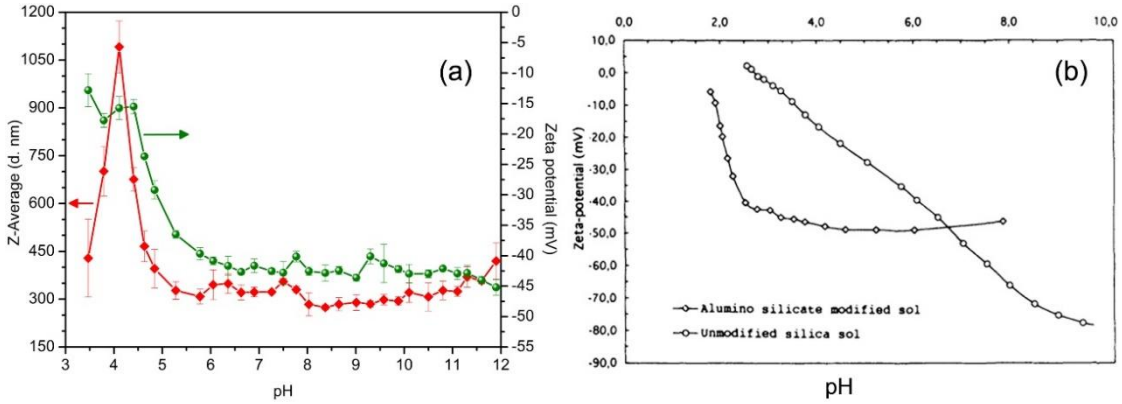

Figure 42. Particle size (red solid diamonds) and zeta potential (green solid spheres) of DGP-W as a function of pH, from this study (a), and zeta potential of unmodified (black open circles) and aluminosilicate modified silica sol (black open diamonds) as a function of pH (b), modified from Otterstedt.[151]

Since the compounding of fillers with polymer melt (rubber for tire, for example) is done under a high pressure, it is essential for the nanoparticulate fillers to withstand high pressures. To test the tolerance of our products to high pressures, both oven and freeze dried DGP-A samples were pressed into circular pellets at 90,000 psi or 620 MPa and their pore properties were measured employing N_2 sorption analysis. Specific surface areas, pore volumes and average pore widths before and after pressing pellets are compared in **Table 11**. Although the surface area and pore volume, and average pore size to a lesser extent decreased for both the samples upon pelletizing as one would expect, more than 60 % of the porosity in these samples is retained indicating that the

samples do not crumble completely under the extreme pressure of 620 MPa. It is worth mentioning that the typical industrial standard procedure (ASTM D3493) of measuring a materials resistance to pore collapsing is performed under a pressure of only 165 MPa,[152] which is 3.75 times smaller than the pressure used in this study. Sintering properties of the materials were also evaluated by subjecting the pressed pellets to heat treatment at several different temperatures and measuring their pore properties after each subsequent heating step as summarized in **Table 11**. Upon heating, all the pellets without any exception appeared shiny to a naked eye but also exhibited cracks which were noticeable under an optical microscope. The surface area of both freeze dried and oven dried samples decreased from 82 m^2/g to 4.9 m^2/g and from 54 m^2/g to 15 m^2/g, respectively, upon heating at 700 °C, as expected due to the sintering of nanoparticles and therefore pore collapsing at elevated temperatures. The pore collapse with increasing temperature is also seen by following the gradual decrease in the pore volume in all samples but freeze dried DGP-A, where the pore volume increased slightly from 0.21 cm^3/g to 0.25 cm^3/g after heating at 400 °C for 6 h. This unusual increment can be understood on the basis that as the particles get sintered, pores get wider and the slight increase in pore volume might be because of the presence of the wider pores. In any case, a clear trend of increasing average pore widths is seen with increasing temperature for both freeze dried and oven dried DGP-A samples confirming the pore collapse. This heat treatment study demonstrated that DGP is suitable for high temperature applications as well. Although not shown here, even after heating at 700 °C for 6 h, samples were still amorphous with no hint of crystallization or structural change observed by powder X-ray diffraction

(PXRD) measurements. This observation is in line with literature i.e. geopolymers do not crystallize below 1000 °C.[153]

Table 11. Pore characteristics of selected sample pellets subjected to various heat treatments.

Sample	Sample Form	Temperature (°C)	BET Surface Area[a] (m^2/g)	Pore Volume[b] (cm^3/g)	Average Pore Size[c] (nm)	Average Particle size[d] (nm)
DGP-A (freeze dried)	Powder	25	148	0.39	11	22
	Pellet	25	82	0.21	10	35
	Pellet	400	72	0.25	14	40
	Pellet	500	63	0.23	15	48
	Pellet	600	32	0.22	28	102
	Pellet	700	4.9	0.05	41	752
DGP-A (oven dried)	Powder	25	101	0.37	16	30
	Pellet	25	54	0.30	15	57
	Pellet	400	52	0.29	22	58
	Pellet	500	47	0.25	23	65
	Pellet	600	39	0.23	25	75
	Pellet	700	15	0.11	34	204

[a]Pressure range P/Po = 0.05–0.20.

[b]Single point desorption nearest $P/P_o = 0.99$.

[c]4(BJH desorption pore volume)/(BET surface area).

[d]Average size = $6000/(SSA_{BET} \times \rho)$, where $\rho = 2.1$ g/cm^3 is the density determined by pycnometry.

6.4. Conclusions

We have demonstrated that it is possible to synthesize highly dispersible geopolymer/ amorphous-aluminosilicate particles by a simple modification of the

geopolymerization process. The simplicity of the modified geopolymerization process bodes well for the large volume production of DGP. By means of N_2 sorption, SEM and TEM we characterized the morphology of DGP to be grape-like bundles similar to high structure CBs and reinforcing structured-silica. As a result of large surface area and high structure, DGP possesses tremendous reinforcing potential. Moreover, highly negatively charged surface of the DGP brings in excellent surface activity making it an ideal candidate for surface modification in order to increase filler-matrix compatibility, and therefore further enhance the reinforcing potential. The translucent or color neutral property of DGP can only expand its potential as a reinforcing agent in polymeric applications, as well as a pigment in paper industry, for instance. Remarkably, unlike commercial aluminosilicates such as Zeolex® and Hydrex®, pastes and dispersions of DGP do not undergo gelation upon long term storage. We also demonstrated that DGP are stable in a rather wide pH range of 12.0 – 5.7 below which gradual agglomeration was noted. Like CBs and reinforcing silica, grape-like bundles of DGP are fused into loosely held agglomerates when dried into powders as revealed by SEM and DLS studies. Additionally, DGP powders are shown to survive large external pressures indicating that the pressures used during compounding to make composites would not be problematic. Further studies are desired to design a better purification process than time and energy intensive centrifugation reported here.

CHAPTER 7

7. EXCEPTIONAL CARBON DIOXIDE SORPTION PROPERTIES OF HIERARCHICAL FAUJASITE ZEOLITES HAVING A HIGH CRYSTALLINITY

7.1. Introduction

The 2014 United Nation's report on climate change urges global action before 2020 to curb global warming driven by increasing emissions − 80 percent of them from the burning of fossil fuels.[154] Carbon capture and storage, or sequestration (CCS) from large point sources like power plants and other large industrial sites, such as cement kilns, steel mills, refineries, ethanol fermenters, and fertilizer manufacturing is widely considered as a near-term option for reducing anthropogenic CO_2 emissions.[155] Nonetheless, these CCS applications are proving to be quite slow to develop on a scale that fits all coal and gas power plants. Climate change predictions suggest that CO_2 reduction technologies must be operating by 2020. Mainstream economic estimations state that CCS is a medium-term, low-cost option that needs to be equipped now and that even a decade of delay in tackling climate change will be economically severe.[73]

Despite the most urgent call for action ever in recent years, CCS technology that exists today is very expensive and energy intensive.[156] Among a variety of separation technologies including membrane separation, absorption, cryogenic distillation, and others, adsorption with solid sorbents appears to be one of the most promising CO_2 capture strategies.[157] Development of low-cost regenerable sorbents that have high selectivity for CO_2 over N_2, high adsorption capacity for CO_2 and require lower

regeneration energy is critical for the success of the more affordable technologies such as vacuum, pressure or temperature swing adsorption (VSA/PSA/TSA) process.[158] Zeolites such as NaX, NaY and zeolite A are inexpensive and yet offer high CO_2 uptake and reasonable selectivity due to the high electrical field gradients in their micropores which is induced by the negatively charged framework and the charge balancing cations.[159] Unfortunately, adsorption of CO_2 in zeolites is not easily reversible and the zeolite adsorbents can be fully regenerated only by heating the adsorbent (around 623 K) in high vacuum, which is too energy-demanding to apply in practice.[160] Control of micropore window by partial ion exchange has been effective in increasing the selectivity, but at the expense of uptake rate.[161] Significant progresses are required to advance zeolites as ideal CO_2 adsorbents.

Herein, we report synthesis of hierarchical Faujasite zeolites that possess a high crystallinity and their exceptional CO_2 sorption properties. Hierarchical zeolites exhibiting additional meso-/macroporosity in general provide an important opportunity, as realistic applications of rapid VSA/PSA/TSA processes demand rapid diffusion rates of CO_2. Ideally, intracrystalline diffusion time decreases quadratically with decreasing the particle size,[162] and yet such predicted improvement has not been seen in previous works, which may be attributed to imperfection of crystallinity and/or the presence of amorphous surface layers.[161a] By achieving a high crystallinity, we demonstrate that hierarchical zeolites not only show faster molecular diffusion but also can have higher capacities, much more improved CO_2-over-N_2 and CO_2-over-CH_4 selectivities, and a negligible capacity loss during regeneration under vacuum, which makes them an ideal adsorbent for practical VSA/PSA/TSA processes.

The synthesis of the hierarchical FAU (Faujasite) zeolites was carried out using a new reactive emulsion method in which geopolymer synthetic chemistry is combined with the principle of soap making reactions (saponification).[104, 163] Geopolymers are an emerging class of amorphous alkali aluminosilicates which are traditionally viewed as high compressive strength construction materials and as a green replacement of Portland cement due to the less CO_2 emission during production.[19a, 164] The synthesis of geopolymers starts with a highly concentrated, viscous aluminosilicate precursor solution (called "geopolymer resin") with an alkali concentration over 10 *M* and a mole fraction of water less than 0.7. Heating the resin gently at an ambient conditions results in hard monolithic geopolymer materials. The compositions of the geopolymer resin correspond to the amorphous gel region in the reaction composition diagrams of zeolite synthesis.[165] Indeed, the resulting geopolymer monoliths exhibit a dense xerogel-like microstructure consisting of highly fused three-dimensional network of roundly-shaped nanoparticles of the sizes ranging from 10 to 50 nm, which are in turn made up of disordered corner-sharing AlO_4 and SiO_4 tetrahedra.[166] Previous studies have shown that applying hydrothermal conditions to such geopolymer resins leads to sodalite (SOD) or zeolite A (LTA) with large crystal sizes.[167] While the synthetic method is advantageous for a high production yield, it has not been extensively used in zeolite synthesis because it does not generally allow a high crystallinity and good control of the particle sizes as well as synthetic flexibilities attainable in other synthetic methods.

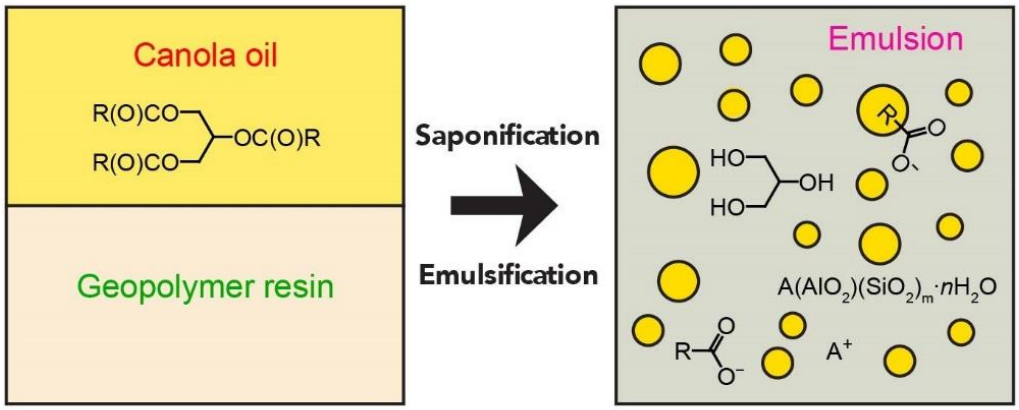

Figure 43. Scheme for the reactive emulsion templating of geopolymer with vegetable oil. A = alkali metal.

7.2. Experimental

7.2.1. Synthesis of Hierarchical FAU Zeolite

Deionized water was used throughout the synthesis and purification. In a typical synthesis, 9.114 g of NaOH pellets (Sigma Aldrich) and 23.411 g of water glass (Sigma Aldrich) were dissolved in 16.382 g of water in a polypropylene beaker. Once cooling down, 11.467 g of metakaolin (MetaMax® from BASF) was slowly added into the solution while stirring. The resulting mixture was homogenized with a mechanical mixer (IKA® RW 60 digital mixer) at 800 rpm for about 40 min to obtain a visually homogeneous and free flowing resin ("geopolymer resin") with the following final molar composition:

$3.0Na_2O : 1.0Al_2O_3 : 4.0SiO_2 : 32.4H_2O$

For those samples prepared by the addition of canola oil, 30 mL of canola oil (The J.M. Smucker Company, Crisco®) was added to the geopolymer resin and the mechanical

stirring at 800 rpm was continued for additional 10 min to give a homogeneous “resin-oil blend”.

The geopolymer resins or resin-oil blends were poured into 50 ml polypropylene tubes and after tightly closed with lids, the tubes were placed in a laboratory oven at 60 °C or 90 °C for an appropriate period of heating time. After the heating, the products, having a consistency of pastes, were taken out from the tubes and washed first with hot water (90 °C) multiples times. The final products were collected via vacuum filtration using a filter paper (Whatman™ Grade 1; particle retention of 11 μm) and washed with cold water until the pH of the filtrates was about 8. They were then dried in a laboratory oven at 110 °C overnight and were stored in sealed glass vials at room temperature for further analysis.

For the products prepared without adding oil, it was noticed that the products were ultrafine particles (nanoparticles) which could not be isolated via simple vacuum filtration. Therefore, the product pastes were first dispersed in water and purified by repeated centrifugation (6000 rpm for 10 min) and redispersion in water until the pH decreased to a constant value (about 8). The precipitates were then dried in a laboratory oven at 110 °C overnight and were stored in sealed glass vials at room temperature for further analysis.

7.2.2. Characterization Methods

Powder X-ray diffraction (PXRD) patterns of the dried samples were collected on Bruker D8 specialized powder X-ray diffractometer (Ni-filtered Cu Kα radiation with a wavelength of 1.5406 Å, operated at 40 kV and 40 mA, VANTEC-1 position-sensitive detector) at a scan speed of 2.0 degrees/min and a step size of 0.016 degrees 2θ. The

resolution of the VANTEC-1 position-sensitive detector was 2θ = 0.008 degrees. Scherrer's equation was applied to [111], [133] and [246] diffraction peaks (2θ = ~6, ~16 and ~27°, respectively) to estimate the average crystallite size of the FAU zeolites.[58b, 168]

Scanning Electron Microscopy (SEM) imaging of powdered samples was performed with a SEM-XL30 Environmental FEG (FEI) microscope. The analysis was performed with 15 kV acceleration voltage and a spot size of 3. For SEM, finely ground dried sample powders were sprinkled on to the SEM stub affixed with copper conducting tape and the samples were then gold coated for 75 s right before imaging.

Transmission Electron Microscopy (TEM) imaging was performed on a JEOL TEM/STEM 2010F (Schottky Field Emission source, accelerating voltage 200 kV). For TEM studies, sample powders were first dried at 250 °C for at least 12 h under vacuum until a residual pressure of ≤10 μmHg was reached. The dried powders were then quickly sprinkled on to the copper grid covered with a holey carbon film right before sample loading.

Brunauer-Emmett-Teller (BET) surface areas were estimated with a Micrometrics ASAP 2020 volumetric adsorption analyzer with nitrogen as the adsorbate at 77 K. Prior to the analysis, samples (about 300 mg) were degassed at 250 °C for at least 12 h under vacuum until a residual pressure of ≤10 μmHg was reached. The specific surface area (SSA_{BET}) was calculated according to the BET equation, using nitrogen adsorption isotherms in the relative pressure range from 0.01 to 0.2.[98] Specific surface area of micropores (SSA_{micro}) and the micropore volume (V_{micro}) are calculated by applying t-plot method in the thickness range of 0.35 nm to 0.50 nm and, Harkins and Jura thickness equation. External surface area (SSA_{ext}) is estimated as the difference between specific

surface areas obtained from BET equation and t-plot method. For the calculation of mesopore size distribution, desorption branch was considered and the total pore volume (V_{total}) was obtained from the amount of nitrogen adsorbed at a relative pressure (P/P_o) of 0.99, assuming complete pore saturation. Mesopore size distributions were obtained using the Barrett-Joyner-Halenda (BJH) method assuming a cylindrical pore model.[99]

Elemental compositions and atomic ratios of silicon to aluminum (Si/Al) of the zeolite samples were determined by inductively coupled plasma-optical emission spectrometry (ICP-OES) using Thermo Scientific iCAP 6300 spectrometer. Prior to the analysis, solid samples were acid-digested using a CEM MARS 6 microwave reaction system in repeated heating steps at 180 °C for 30 min with sequential addition of required reagents. Specifically, 20 – 30 mg of samples were heated in the reactor first with 3 mL of concentrated HCl solution (34 – 37 wt%, ACS), and second with a mixture of 3 mL concentrated HNO_3 (67 – 70 wt%, ACS) and 0.5 mL of HF solution (48 – 51 wt%, ACS). The digests were later quenched with 5 mL of 4.5 wt% H_3BO_3 solution aided by the microwave reactor.

Free hydroxide ion concentration in the reaction mixtures was measured after ultrasonicating the samples that were in the form of thick pastes for five minutes in deionized water (24 times by volume) to give a final pH value between 11 and about 13. The pH values were measured with a HACH® H160 pH meter equipped with a HACH® non-glass ISFET pH stainless steel probe. The pH meter was calibrated with at least 3 standard buffers before every measurement and all measurements were made in triplicates of samples. The pH of the initial samples were calculated by using a dilution factor of 25.

7.2.3. Evaluation of Sorption Properties

CO_2 adsorption measurements were obtained volumetrically using an ASAP 2020 analyzer (Micromeritics). Prior to measurements, samples were degassed at 300 °C for 10 h before measurement. Measurements were performed at 0, 10, 20, 30, 40 and 60 °C within a relative pressure region of 0.0004 – 0.99 P/P_o. Temperatures were controlled by a CF31 cryo-compact circulator (Julabo Labortechnik GmbH, Seelbach, Germany) during the measurement. The equilibrium adsorption−desorption cycles were measured in the CO_2 pressure regime of 0.011 to 100 kPa. The kinetics of adsorption of CO_2 on the micron-sized and hierarchical zeolite X samples were investigated by a thermogravimetric analyzer (TGA) using a Setaram TAG 24 instrument (SETARAM Instrumentation, Caluire, France).

7.3. Results and Discussion

Figure 43 shows schematic diagrams for the *reactive* emulsion process employed in this work. When a geopolymer resin is mixed with vegetable oil in a high shear mixer, the triglycerides, the major component in the oil,[97] saponify in the highly alkaline geopolymer resin to generate carboxylate surfactants (soap molecules) *in situ*. The soap and glyceride generated from the saponification are water-soluble and are incorporated into the geopolymer gel matrix. Any excess oil forms oil droplets which become embedded in the geopolymer resin. Notably, it has been found in our work that the oil in the droplets continues to saponify to completion during heating (usually no higher than 90 °C). All the soap and glyceride molecules can be easily extracted from the product with water. While the precise role of the organic molecules is not clear yet, the presence

of the surfactants has allowed formation of hierarchical meso-/macroporous geopolymer.[104, 163]

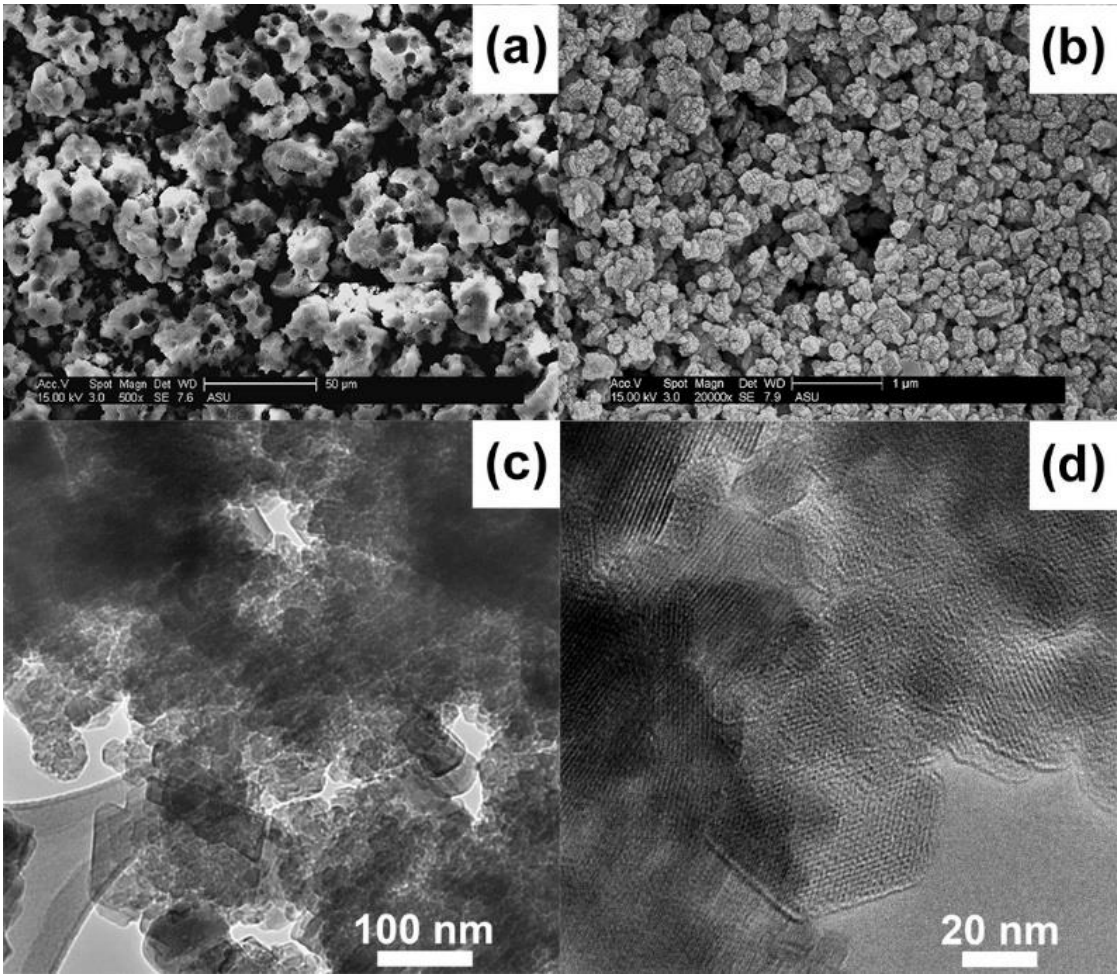

Figure 44. SEM (a & b) and TEM (c & d) images of the sample from geopolymer resin with canola oil heated at 60 °C for 54 hours. The scale bars in (a) and (b) are 50 and 1 μm, respectively.

Remarkably, it was discovered in this work that when using NaOH, hierarchical FAU zeolites could be synthesized with a high degree of crystallinity/microporosity, without significantly modifying the original reactive emulsion synthetic condition.

Figure 44 shows SEM and TEM images of the product produced from the geopolymer resin with the molar composition of $3Na_2O : 1Al_2O_3 : 4SiO_2 : 32H_2O$, mixed with canola oil (50/50 water/oil) that was heated at 60 °C for 54 hours. The product exhibits discrete, roundly-shaped macropores (10 – 200 μm in diameter), the reminiscent of the oil droplets, dotting a matrix of highly nanostructured aggregates in nature (**Figure 44a & b**). The TEM images indicate that the aggregates consist of nano-sized plate-like crystallites showing well-developed lattice fringes (**Figure 44c & d**). Textural pores in the ranges of mesopores are clearly seen among the nanocrystallites. The XRD pattern of the sample matches well with a FAU structure (**Figure 46**) and the elemental analysis results show Si/Al = 1.7 (**Table 12**).

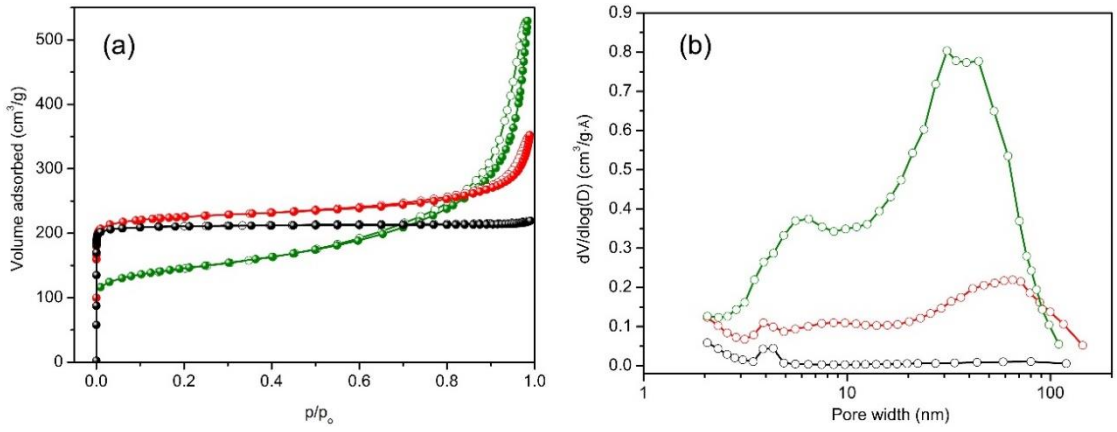

Figure 45. Nitrogen sorption isotherms (a), and BJH desorption pore distributions (b) of the samples prepared from geopolymer resin with (red) and without (green) canola oil heated at 60 °C, with commercial 13X reference zeolite (black).

The observed nanostructures are consistent with the N_2 sorption behavior of the product (**Figure 45a**), exhibiting an isotherm that is a combination of types I and IV, as typical of a material having both micropores and mesopores. While the type H1

hysteresis at high relative pressures ($P/P_o \geq 0.6$) is a signature of mesopore presence,[169] the gas intake does not saturate at partial pressure, $P/P_o = 1$, indicating the presence of macropores.[145] Presence of broad range of mesopores which extend into the macropore region can be clearly seen in the BJH desorption pore size distribution curve plotted in **Figure 45b**. The commercial 13X zeolite exhibits a type I nitrogen sorption isotherm that is typical of a sample having micropores only. A small sharp peak centered at 4 nm observed for both samples in **Figure 45b** but not seen in the BJH adsorption pore size distribution curves (data not shown) could be an artifact arising from the inapplicability of Kelvin equation (basis of BJH model) in the microporous region, i.e. for pores < 2 nm in width.[170] Cavitation and capillary desorption effects can be ruled out because of the absence of sudden closure of the hysteresis loop in the isotherms at a partial pressure of 0.4 – 0.5.[171] The hierarchical FAU showed a mesopore volume of 0.22 cm^3/g and a surface area of 121 m^2/g. The calculated micropore volume and surface area were 0.30 cm^3/g and 635 m^2/g, respectively, while 0.31 cm^3/g and 663 m^2/g were found for the 13X. The estimated crystallinity of the sample from the microporosity was 96% with respect to the 13X.

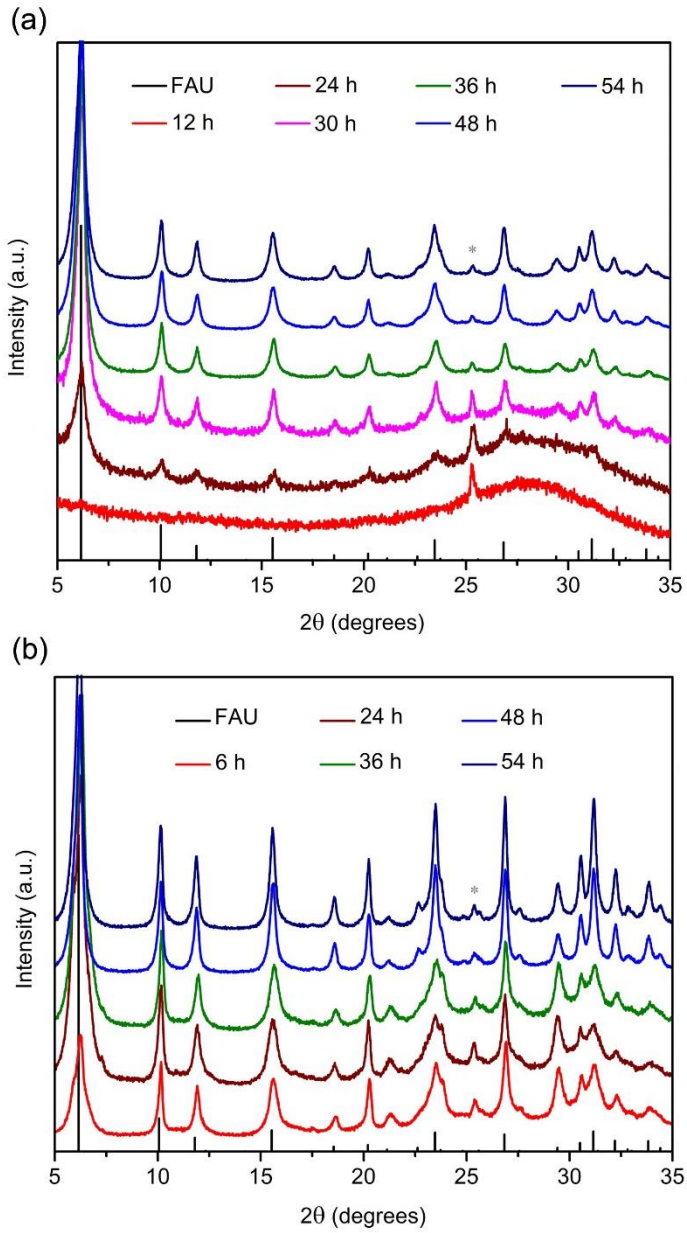

Figure 46. XRD patterns of samples (3.0 Na_2O : Al_2O_3 : 4.0 SiO_2 : 32.4 H_2O and canola oil/H_2O (v/v) = 1.0) heated at 60 °C for 12, 24, 30, 36, 48 and 54 hours, with the simulated patterns of FAU (Si/Al = 1.7) (a), and 90 °C for 12, 24, 30, 36, 48 and 54 hours, with the simulated patterns of FAU (Si/Al = 1.6) (b), along with (*) anatase (PDF#00-021-1272).

We examined the conversion of the geopolymer gel into the hierarchical FAU for a total period of 54 hours, by quenching a sample at different times of heating. In **Figure 46a**, the XRD pattern of the sample heated at 60 °C for 12 hours shows a broad amorphous peak centered around 28°, typical of geopolymer also seen at pre-crystallization stages of zeolite synthesis, in addition to a small peak at 25.3° assigned to anatase (TiO_2) present as a minor impurity in the metakaolin (Metamax®). The FAU reflection peaks start to appear after 24 hours of heating and as the heating continues, their intensities increase at the expense of the broad amorphous peak. After 48 hours, the amorphous peak becomes negligible and the XRD pattern no longer changes, indicating the ending of crystallization. The corresponding TEM images (**Figure 47**) corroborate these findings, in that at first the product exhibits a typical geopolymer gel structure with roundly-shaped, fused gel particles of 20 to 50 nm in diameter (but with a large textural porosity)[104] and that upon continuous heating, they gradually turn into nanostructured crystals with well-defined edges and lattice fringes to completion. Unlike in typical crystallization process, however, the TEM images indicate that the particles do not grow in size during the heating, and in fact the particles appear to keep the original volume while developing angular structures. The average crystallite sizes from Scherrer's equation are ~20 nm from all the XRD patterns, showing no crystal growth during heating, despite the increased crystallinity (**Table 12**). The gradual increase in the crystallinity can be seen also in the trend of the micropore surface area and volume. Similar results were found from the synthesis at a higher temperature (90 °C), only with a faster crystallization and better crystallinity (**Figure 46** and **Table 12**).

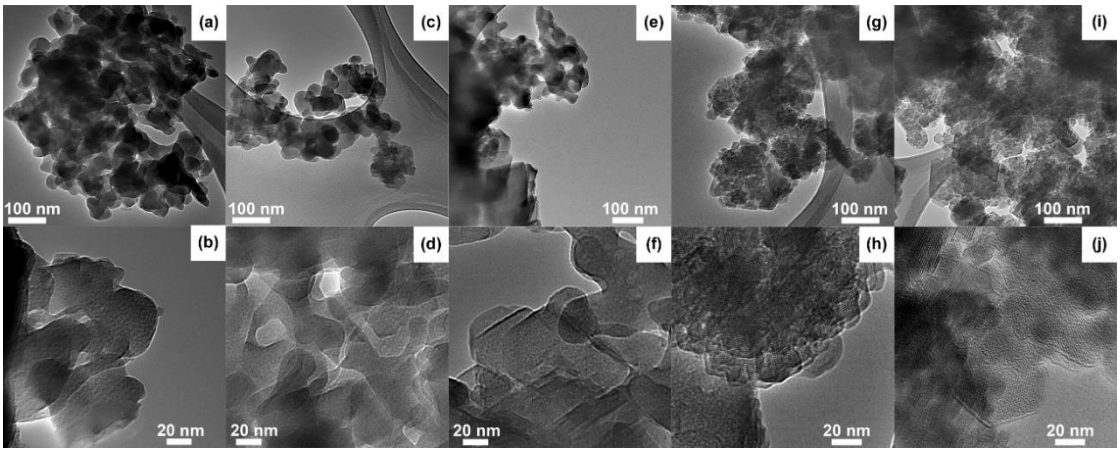

Figure 47. TEM images of the samples in **Figure 46a** prepared by heating at 60 °C for 12 hours (a and b), 24 hours (c and d), 36 hours (e and f), 48 hours (g and h), and 54 hours (i and j).

Interestingly, when canola oil is not mixed in the geopolymer resin, the same synthetic procedure results in a product that is highly mesoporous but with a limited microporosity with a FAU structure, as deduced from the XRD patterns (**Figure 48**) and N_2 sorption isotherm and BJH curve for the product (**Figure 45**). The calculated micropore volume and surface area were 0.13 cm^3/g and 279 m^2/g, respectively, with a mesopore volume of 0.71 cm^3/g and an external surface area of 218 m^2/g. The estimated crystallinity from the microporosity was 42% with respect to the 13X. The microporosity was not improved even after 20 days of heating but instead a competing SOD phase started to appear after 10 days, whose presence became more prominent afterwards. Upon increasing the heating temperature to 90 °C, mixed phases of FAU and LTA were obtained along with a small amount of SOD even at very early stages (within 2 hours). After 3 days of heating, highly crystalline SOD was the only phase observed, which is consistent with previous studies.[167]

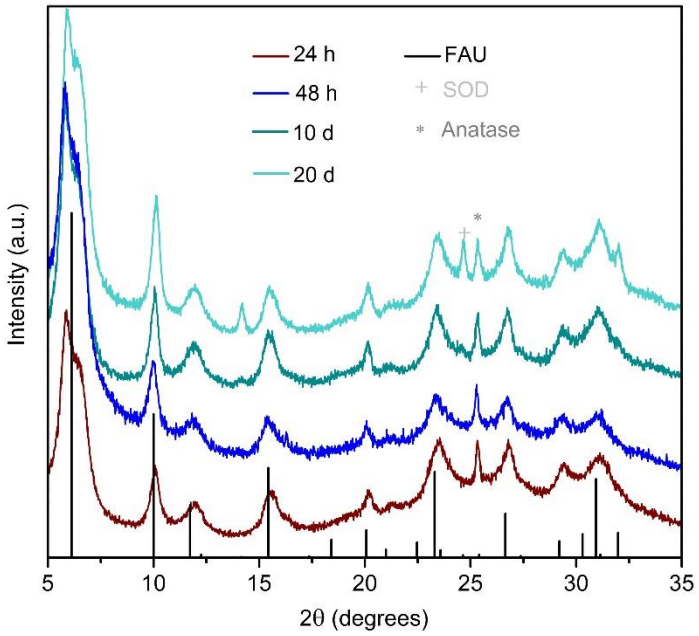

Figure 48. XRD patterns of samples (3.0 Na_2O : Al_2O_3 : 4.0 SiO_2 : 32.4 H_2O) heated without oil at 60 °C for 1, 2, 10 and 20 days, with the simulated patterns of FAU (Si/Al = 1.3), (+) SOD (PDF#00-046-0866) and (*) anatase (PDF#00-021-1272).

The detailed role of the canola oil is not clear in achieving the observed high microporosity. We have found that the saponification reaction of the canola oil reduces the free OH^- ion concentration to about 1 *M* within six hours during the heating (**Figure 49**). In the absence of the oil, however, the concentration in the geopolymer resin decreases initially to 3.5 *M* but increases back to 6 *M* in six hours. It has been well established that the initial concentrations of the reactants as expressed conversely by the water content in the mixture are critical in determining the species produced and that FAU crystallizes in a rather narrow range of pH values, values between 12.3 and 13.8 with low pH values enabling formation of high silica FAU (NaY) and high pH values assisting the formation of low silica FAU (NaX).[172] While the high pH condition is still

important for nucleation, however, our results indicate that it hinders achieving a high degree of microporosity of FAU at 60 °C, let alone the problem of the phase instability of FAU at higher temperatures, in our synthetic procedure. In contrast, the pH decrease by saponification delays the crystallization at first but helps gradual improvement of the crystallinity without increasing the crystal sizes. It also stabilizes the FAU phase even at higher temperatures during crystallization without increasing particle sizes.

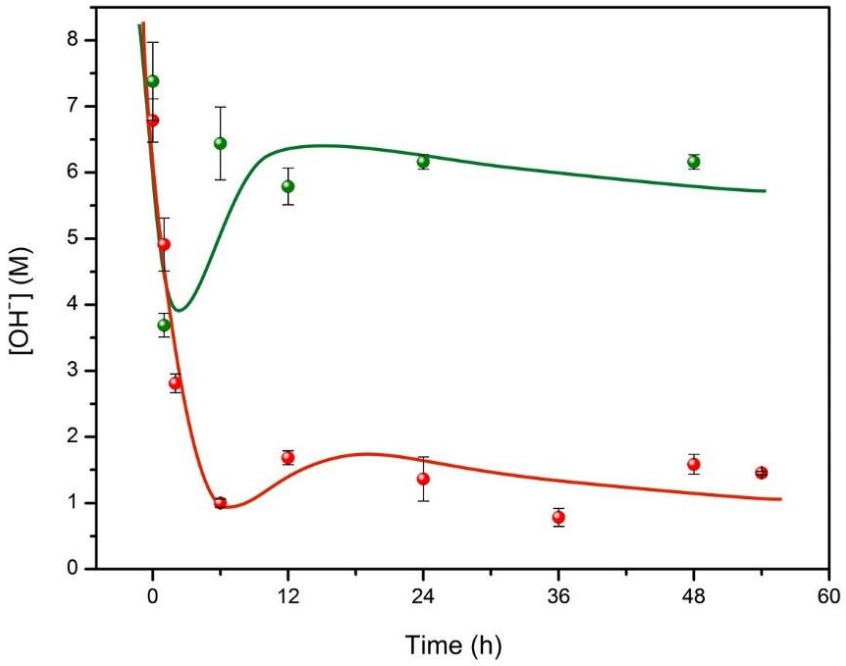

Figure 49. Free hydroxide ion concentration (*M*) versus heating time (hours) for the samples heated at 60 °C without (green) and with (red) canola oil.

Table 12. Pore properties along with their Si/Al ratio and crystallite size of hierarchical zeolites obtained from various synthetic conditions.

Sample	SSA_{BET} (m^2/g)	SSA_{micro} (m^2/g)	SSA_{ext} (m^2/g)	V_{total} (cm^3/g)	V_{micro} (cm^3/g)	V_{meso} (cm^3/g)	Si/Al[a]	Crystallinity[b] (%)	Crystallite size[c] (nm)
13X (Sigma-Aldrich)	694	663	31	0.34	0.31	0.03	1.42	—	2000 – 5000
60 °C									
12h	38	0.04	38	0.18	0.001	0.18	1.84	0	—
24h	90	52	38	0.21	0.02	0.19	1.80	8	20 (7)
36h	205	159	45	0.24	0.07	0.17	1.81	24	22 (5)
48h	729	599	130	0.53	0.28	0.25	1.75	90	21 (6)
54h	756	635	121	0.52	0.30	0.22	1.74	96	21 (5)
90 °C									
6h	666	555	112	0.47	0.26	0.22	1.56	84	20 (8)
24h	703	600	103	0.47	0.28	0.19	1.57	90	22 (7)
36h	760	663	97	0.52	0.31	0.21	1.62	100	25 (6)
48h	709	616	93	0.49	0.29	0.20	1.64	93	25 (6)
54h	734	643	91	0.50	0.30	0.20	1.64	97	27 (3)
No oil, 60 °C 1 day	496	279	218	0.82	0.13	0.71	1.33	42	—

[a]Determined by ICP-AES.

[b]Determined from the micropore surface area with respect to 13X.

[c]Average size (standard deviation in parenthesis) determined by applying Scherrer's equation to [111], [133] and [246] reflection peaks.

Zeolite NaX is one of the most promising and widely studied sorbents for carbon capture with high CO_2 adsorption capacity.[159b, 173] Herein, commercial micron-sized (3-5 μm) NaX zeolite crystals, namely 13X were used as a benchmark for comparisons of CO_2, N_2 and CH_4 adsorption capacity, CO_2-over-N_2 and CO_2-over-CH_4 selectivities, and

CO_2 uptake kinetics with highly crystalline hierarchical faujasite sample, 60°C-54h prepared in this study. CO_2 adsorption isotherms measured at various temperatures (**Figure 50)** demonstrate that hierarchical zeolite 60°C-54h exhibits high CO_2 uptake capacity. The steady decrease in the uptake capacity with increasing temperature is expected for zeolite sorbents and is consistent with other reports.[161b, 174] At 20 °C, 60°C-54h adsorbs 5.9 mmol/g of CO_2. N_2 and CH_4 adsorption capacities are much lower than CO_2 at 20 °C for both 60°C-54h (**Figure 51a**) and 13X zeolite (**Figure 51b**). This is mainly due to stronger interaction of CO_2 molecules of larger polarizability and quadrupole moment with the surfaces of the ionic faujasite cages.[161c, 175] Moreover, CO_2 uptake capacity of 60°C-54h is comparable to that of 13X (**Figure 51b**) and coincides well with their BET surface areas. The high CO_2 adsorption capacity compared to N_2 and CH_4 suggest that hierarchical zeolite 60°C-54h can offer high CO_2-over-N_2 and CO_2-over-CH_4 selectivity from various CO_2-N_2 and CO_2-CH_4 gas mixtures.

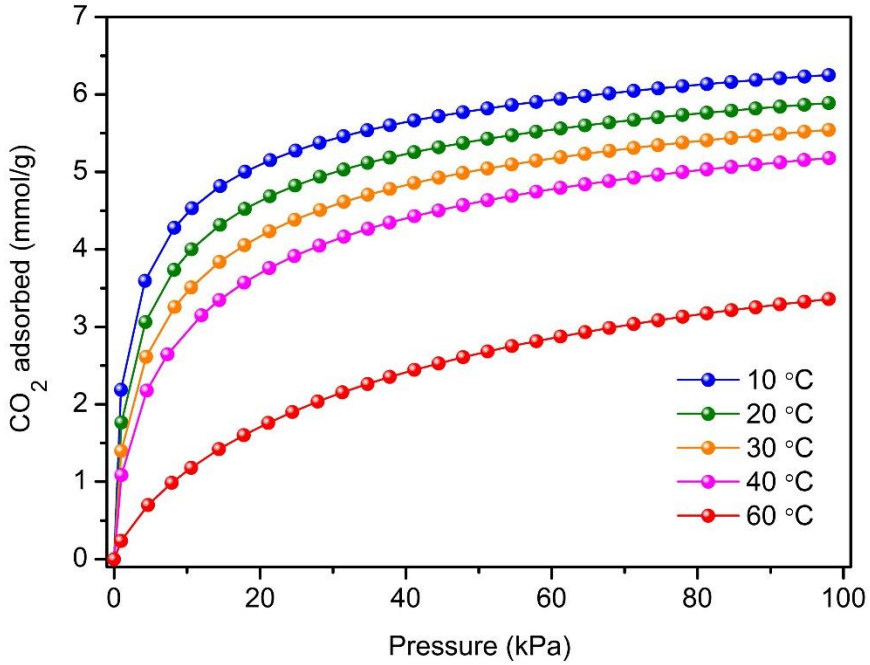

Figure 50. Pure component CO_2 adsorption isotherms for hierarchical zeolite 60°C-54h at 10, 20, 30, 40 and 60 °C.

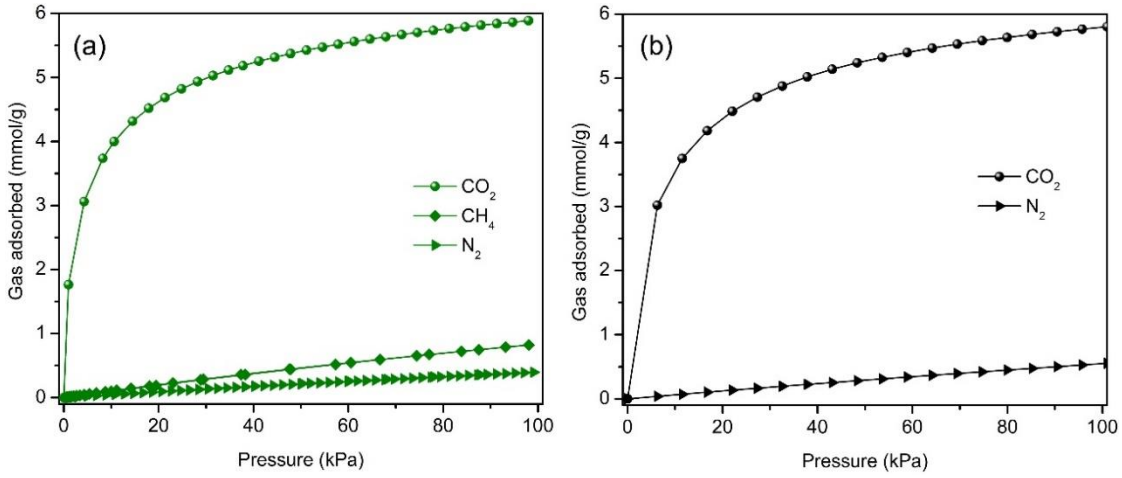

Figure 51. Pure component adsorption isotherms of CO_2 (solid spheres), CH_4 (diamonds) and N_2 (side-facing triangles) on hierarchical zeolite 60°C-54h (a), and commercial 13X reference zeolite (b). All isotherms were measured at 20 °C.

Selectivity of a sorbent towards one versus the other can be defined in many ways. The simplest is the ideal CO_2-over-N_2 selectivity (S_{CO_2/N_2}) which can be estimated for a gas mixture of 15 mol % CO_2 and 85 mol % N_2, a typical composition of power-plant flue gas burning coal,[176] as the ratio of equilibrium mole fraction of CO_2 adsorbed at 15 kPa ($x_{CO_2}^{15}$) over the equilibrium mole fraction of N_2 adsorbed at 85 kPa ($y_{N_2}^{15}$):

$$S_{CO_2/N_2} = \frac{x_{CO_2}^{15} \cdot 85}{y_{N_2}^{15} \cdot 15} \qquad (10)$$

Similarly CO_2-over-CH_4 selectivity ($S_{CO_2/CH_4} = \frac{x_{CO_2}^{50}}{y_{CH_4}^{50}}$) can be estimated in a gas mixture that contains 50 mol% CO_2 and 50 mol% CH_4. Such an estimate is applicable in the context of biogas upgrading, for example. Defined in this way, the CO_2-over-N_2 and CO_2-over-CH_4 selectivities for 60°C-54h are 72 and 12, respectively. More physically correct estimates of the selectivity, from one component adsorption data, make use of Ideal Adsorbed Solution Theory (IAST) developed by Myers and Prausnitz.[177] IAST has been used to predict the gas adsorption from CO_2–N_2 and CO_2–CH_4 gas mixtures on zeolites and metal organic frameworks (MOFs) and estimate the CO_2-over-N_2 and CO_2-over-CH_4 selectivities.[178] In this work, the description of the experimental data to the theory at the pressures and temperatures of interest are suitably small, ~5% of the experimental error that is considered negligible. The gas-gas and gas-substrate interactions are assumed to be ideal at low pressure used in the calculation to justify using ideal adsorbed solution theory to predict CO_2-over-N_2 and CO_2-over-CH_4 selectivities. Using IAST, it is possible to define a two phase model selectivity as the

ratio of mole fraction of CO_2 in the adsorbed state (x_{CO_2}) over the mole fraction of CO_2 (y_{CO_2}) in the gas phase divided by the same relative fractions for N_2 (x_{N_2}, y_{N_2}) or CH_4 (x_{CH_4}, y_{CH_4}).

$$S_{CO_2/N2} = \frac{x_{CO_2} \cdot y_{N_2}}{x_{N_2} \cdot y_{CO_2}} \qquad (11)$$

$$S_{CO_2/N2} = \frac{x_{CO_2} \cdot y_{CH_4}}{x_{CH_4} \cdot y_{CO_2}} \qquad (12)$$

IAST Selectivities, S_{CO_2/N_2} and S_{CO_2/CH_4}, for hierarchical sorbent 60°C-54h shown in **Figure 52a & b** are 790 and 230, at 20 °C and 100 kPa pressure with a capacity to adsorb ~5.4 $mmolg^{-1}$ and ~5 $mmolg^{-1}$ of CO_2, respectively. This excellent selectivity for CO_2 from binary mixtures would result in very high purity for the captured CO_2 in the desorbed enriched product stream. A review of the literature revealed that CO_2-over-N_2 and CO_2-over-CH_4 IAST selectivities are the highest yet reported in the context of zeolites[159c] (for example, CO_2-over-N_2 selectivities of 530 and 660 for CaA[179] and NaKA (17% K^+),[180] respectively).

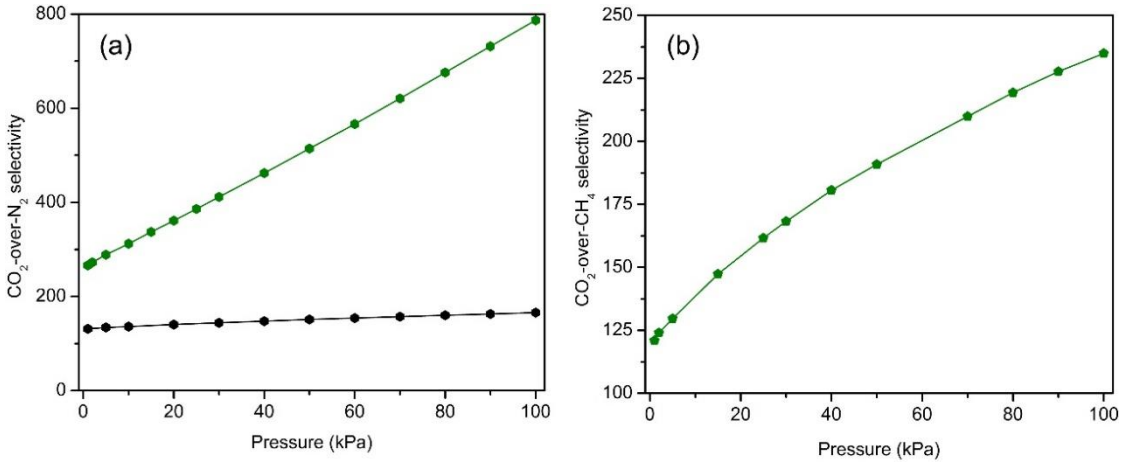

Figure 52. Adsorption selectivity as calculated using IAST at 20 °C of CO_2-over-N_2 : 15:85 for hierarchical zeolite 60°C-54h (olive hexagons) and commercial 13X reference zeolite (black hexagons) (a), and CO_2-over-CH_4 : 50:50 for hierarchical zeolite 60°C-54h (olive pentagons) (b).

IAST predicts that the major adsorbed molecules are of CO_2 on 60°C-54h (**Figure 52**) at all pressures from a gas mixture of 15 mole % CO_2 and 85 mole % N_2. The IAST estimates that the uptake capacity for CO_2 is reduced only slightly from 5.9 mmol/g to 5.4 mmol/g in the presence on N_2, but uptake capacity for N_2 is reduced significantly by the presence of comparatively small amounts of CO_2 in the gas mixture and increasing the CO_2-over-N_2 selectivity to ~800 at 100 kPa. Binary adsorption of CO_2 and N_2 from a gas mixture of 15 mole % CO_2 and 85 mole % N_2 has been determined experimentally on commercial 13X zeolite and preferential CO_2 adsorption from binary mixture of CO_2 and N_2 has been observed.[112b, 173d, 181] Grand canonical Monte Carlo simulations (GCMC) for binary adsorption of CO_2 and N_2 on silicalite-1, ITQ 3 and ITQ 7 materials showed an enhanced competitive adsorption of CO_2 as compared with the single component adsorption predictions as CO_2 displace less strongly adsorbed N_2. The GCMC simulation

results were comparable to IAST prediction.[182] In the case of 60°C-54h, the reduced uptake of N_2 in the presence of CO_2 gas can be attributed to stronger CO_2 interaction with the surfaces of the ionic cages than N_2, due to its larger electric quadrupole moment[183] (-14.3×10^{-40} C m^2) than N_2 (-4.7×10^{-40} C m^2). The comparison of IAST estimates of CO_2 and N_2 uptake with commercial 13X powder (**Figure 52a & b**) confirms that zeolite 60°C-54h with hierarchical structure shows superior CO_2-over-N_2 and CO_2-over-CH_4 selectivity.

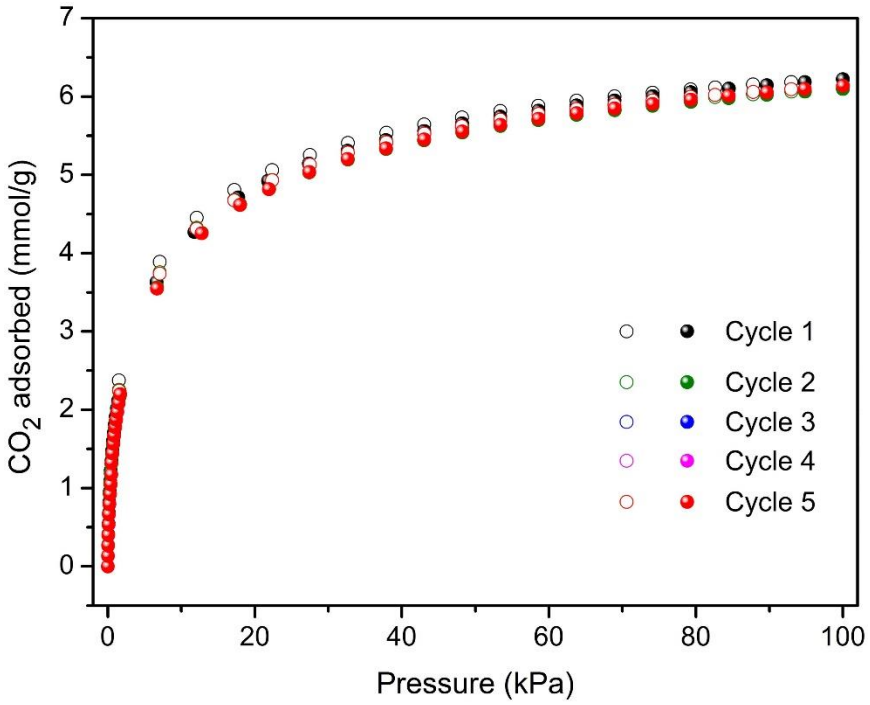

Figure 53. Five cycles of CO_2 adsorption (solid spheres) and desorption (open spheres) on hierarchical zeolite 60°C-54h using vacuum swing regeneration mode from pure component at 273 K.

Whereas the hierarchical faujasite sorbent reported here exhibit very good performance with respect to CO_2 selectivity, its amenability to recycling and conditions

suitable for regeneration must also be addressed. The former was validated via cyclic adsorption–desorption experiments conducted at 20 °C. 60°C-54h sorbent could be regenerated by simple evacuation without the need for applying heat. **Figure 53** shows the cyclic CO_2 sorption capacity of hierarchical zeolite for five cycles. Extraordinarily, the capacity of CO_2 adsorption of 60°C-54h did not diminish irreversibly after the first cycle, which is typically a 15% decrement for 13X and other zeolites after first cycle.[161c, 184] The reduction in CO_2 uptake after first cycle is typically associated with chemisorption of CO_2 on zeolites and cannot be overcome without regeneration via prolonged heating at temperatures above 300 °C.[160, 185] However, 60°C-54h sorbent can be regenerated without heating by simply subjecting it to near vacuum conditions. As a related consequence, we found that the heat of CO_2 adsorption of 60°C-54h is ~35 kJ/mole which is lower than that reported for zeolites and lies in the range of physisorption process. Furthermore, the heat of CO_2 adsorption of 35 kJ/mol for hierarchical zeolite sorbent 60°C-54h calculated from variable temperature isotherms is consistent with the steepness of the CO_2 adsorption isotherms. The relatively constant heat of adsorption (data not shown) indicates homogeneous binding sites over the full range of CO_2 loading. The lower heat of CO_2 adsorption on 60°C-54h compared to 13X could be a consequence of its higher Si/Al ratio (1.74 compared to 1.42 for 13X; **Table 12**). Zeolites with higher Si/Al ratio are less hydrophilic and are known to exhibit both lower CO_2 adsorption energy and lower overall uptake.[159b] Incredibly, 60°C-54h with higher Si/Al ratio uptakes comparable amount of CO_2 to that of 13X, if not slightly higher. In any case, the low value of heat of adsorption suggests that most of the CO_2 molecules are physisorbed which favor efficient, reversible adsorption–desorption

processes – that is, strong but still reversible sorption. To put this in perspective, Maring and Webley estimated the optimal heat of adsorption of CO_2 for PSA applications to be between 35 and 45 kJ/mol regardless of N_2 heat of adsorption.[159a]

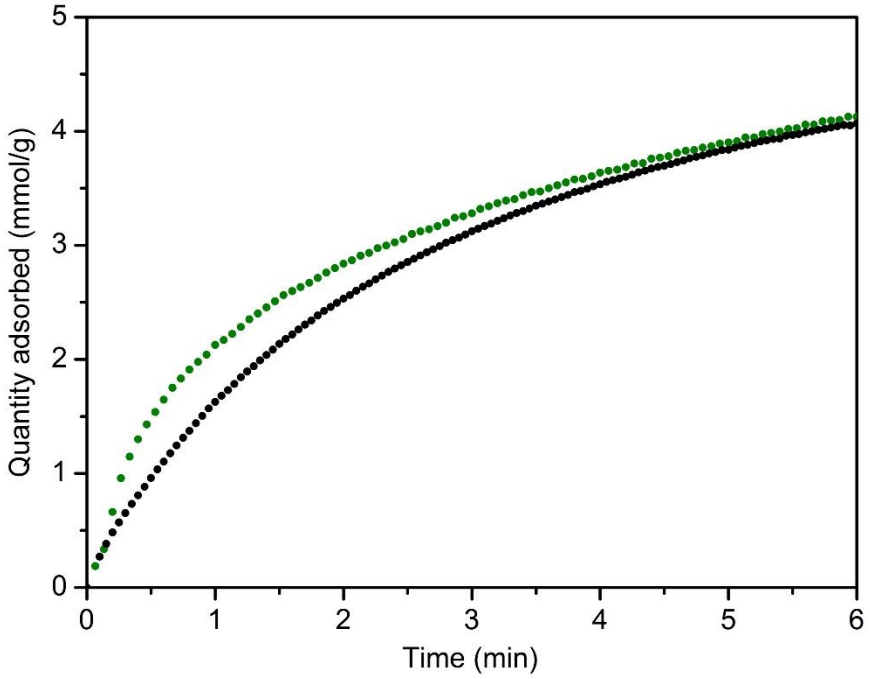

Figure 54. Kinetics of adsorption of CO_2 from pure component by hierarchical zeolite 60°C-54h (olive circles) and commercial 13X reference zeolite (black circles) measured at 298 K and 100 kPa.

The kinetics of CO_2 measured using thermogravimetric data (**Figure 54)** showed that the initial uptake of CO_2 is rapid and it took about a minute for hierarchical faujasite sorbent 60°C-54h to attain 40% (~2.1 $mmolg^{-1}$) of its maximum CO_2 uptake capacity. On the other hand, micron-sized 13X crystals realized 40% of its CO_2 uptake capacity in twice as much time (~two minute) displaying slower kinetics. This could be the consequence of not only the reduced diffusion path lengths in the case of zeolite 60°C-

54h with hierarchical structure owing to the presence of nanocrystals, but most importantly due to their high crystallinity which is not often the case with zeolites exhibiting such nanostructures. However, the reduction of adsorption kinetics beyond 40% of the capacity could be due to thermal effects, where an increase in temperature influences the adsorption kinetics. The role of thermal effects have been discussed in several zeolitic system.[186]

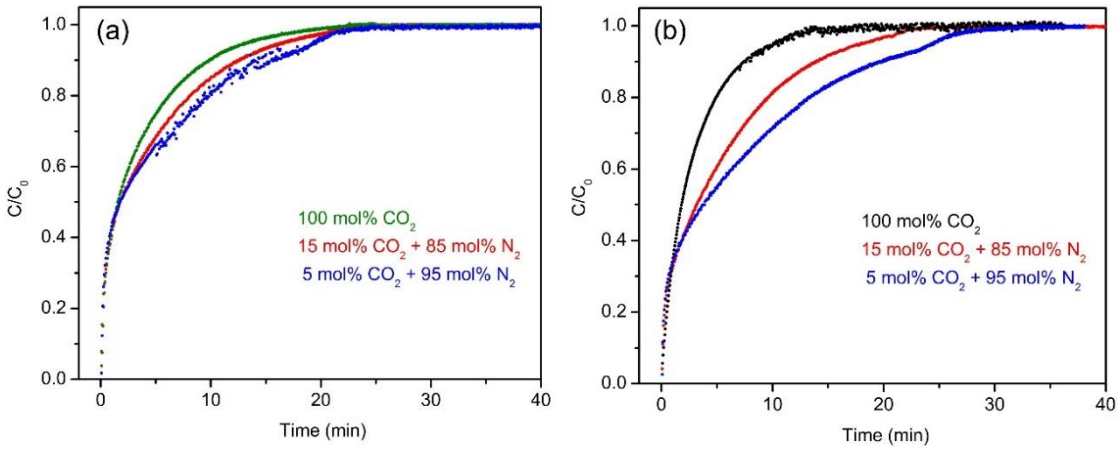

Figure 55. Kinetics of adsorption of CO_2 measured at 25 °C and 100 kPa from binary components on hierarchical zeolite 60°C-54h (a), and commercial 13X reference zeolite (b).

To confirm the synergistic nature of the thermodynamics and kinetics for CO_2 capture, competitive adsorption kinetic studies from gas mixtures were conducted and are presented in **Figure 55**. We note that the CO_2 non-equilibrium uptake at equal times from mixtures of CO_2 and N_2 gas, most notably mixture containing only 5 mol% of CO_2, follows the behavior obtained from pure CO_2 fairly well. In addition, at equilibrium the total CO_2 uptake from the CO_2-containing gas mixtures agrees perfectly with the equilibrium uptake for pure CO_2. These distinctive findings show that when 60°C-54h is

contacted with CO_2-containing gas mixtures, CO_2 adsorbs more strongly and faster than N_2, thus occupying all the available space and sorption sites and consequently excluding other gas molecules. Most importantly, 60°C-54h meets the demanding attributes required for economical and efficient CO_2 post-combustion separation better than any commercial or reported zeolites. Furthermore, rapid and preferential adsorption of CO_2 molecules from gas mixtures containing small fraction of CO_2 (5 mol% CO_2) presents our hierarchical faujasite as a potential sorbent for natural gas upgrading as well.

7.4. Conclusions

We have demonstrated a new synthetic route to produce hierarchical faujasites by coupling geopolymer chemistry with a saponification reaction. For the first time ever, we disclosed that it is possible to crystallize highly crystalline zeolites from geopolymeric compositions. In addition to comparable microporosity and therefore crystallinity to the micron sized zeolite 13X (~2 μm), the produced hierarchical faujasites exhibited large external surface areas arising from accompanying intercrystalline meso and macropores. We also demonstrated that the hierarchical faujasite 60°C-54h could adsorb CO_2 with exceptional selectivity and recyclability in the context of several industrially relevant CO_2 separation applications, such as post-combustion (flue gas, CO_2/N_2) and natural gas upgrading (natural gas clean-up, CO_2/CH_4). At 20 °C and 100 kPa, hierarchical zeolite 60°C-54h had high capacity for CO_2 adsorption from pure component (~5.9 mmol/g) as well as binary mixtures of CO_2/N_2 (~5.4 mmol/g) and CO_2/CH_4 (~5.0 mmol/g), and very high CO_2-over-N_2 and CO_2-over-CH_4 selectivities of 790 and 230, respectively. Extraordinarily, unlike any other zeolites reported to date, the cyclic CO_2 capacity of

60°C-54h was retained completely even after 5 cycles without regeneration by heat in between (vacuum only). The rate of adsorption of CO_2 by 60°C-54h from pure component as well as mixed-gases is also faster than that observed for 13X. The structural features and exceptional mixed-gas sorption properties of the hierarchical faujasites reported here show that it is now possible to completely recycle zeolite without applying heat to facilitate effective rapid CO_2 separation and capture.

CHAPTER 8

8. CONCLUSIONS AND RECOMMENDATIONS

The main outcome of this thesis has been expanding the geopolymerization chemistry and therefore produce three new nanostructured aluminosilicate materials – geopolymers with hierarchically meso-/macroporous structures, dispersible geopolymer particles, and hierarchical faujasite zeolites with a high crystallinity. The synthetic techniques developed in this study are all simple modifications of geopolymerization process while being scalable and remaining cost-effective. Although these materials have superior properties to the equivalent commercially available and currently reported materials, they are still a work in progress and there is much room for improvement. This chapter will summarize the conclusions drawn throughout this thesis and make recommendations for future work.

Chapter 3 demonstrated that synthesis of hierarchically porous geopolymers is possible by employing a simple emulsion templating with triglyceride oil. By extensive characterization, these products were shown to have coexisting distinctive mesopores and macropores. Chapters 3 and 4 showed that the pore properties of these products can be controlled by changing the compositional parameters such as oil type, and Si, Al, alkali and water contents in the precursor solution. Further studies are necessary to clarify the precise role of those compositional parameters. However, the phase diagrams constructed in chapter 4 allows a simplistic, unambiguous identification of compositions for the formation of hierarchically porous geopolymers with specific pore properties. It is

recommended for the future investigations to include non-compositional parameters such as time and temperature of curing.

In Chapter 5, hierarchically meso-/macroporous geopolymers prepared in chapters 3 and 4 were modified with amorphous hydrous ferric oxide (HFO). These geopolymer composites were shown to be effective media for the removal of arsenic from contaminated water under realistic conditions. Additionally, the spent media was classified as a non-hazardous material that can be disposed as a solid waste. This study, as an example of adsorption based applications, verified the structural integrity of hierarchically porous geopolymers under characteristic physical and chemical stresses of such processes. We therefore recommend these materials as supports for adsorption and catalytic applications, and many others.

Chapter 6 described another modification of the geopolymerization process by which it is possible to synthesize highly dispersible geopolymer particles (DGP). DGP were shown to exist as grape-like bundles, a morphology similar to high structure carbon blacks (CBs) and structured-silica, thereby emphasizing their tremendous potential in polymer reinforcing. This is further highlighted by the fact that DGP were able to survive external pressures larger than what is typically used during polymer/rubber compounding. Furthermore, DGP were also shown to exhibit superior stability compared to commercial aluminosilicates such as Zeolex® and Hydrex® towards long term storage. It is worth mentioning that although the synthesis is straightforward, further studies are desired to design a better purification process than relatively time and energy intensive centrifugation presented here. Future investigations should further target

surface functionalization of DGP by taking advantage of its highly negatively charged surface, and thereby broaden its compatibility with organic solvents and matrices.

Chapter 7 demonstrated yet another synthetic modification of geopolymerization process, which made it possible to produce highly crystalline hierarchical faujasite zeolites for the first time ever. The produced hierarchical zeolites exhibited superior pore properties than commercially available 13X in that, hierarchical zeolites displayed large mesoporosity in addition to the microporosity comparable to 13X. Moreover, these hierarchical zeolites were superior to commercially available 13X in the context of CO_2 separation from industrially important gas mixtures – in terms of capacity, selectivity, recyclability and kinetics. However, the low Si/Al ratio of these faujasite zeolites mean they are not suitable for catalytic applications such as cracking and isomerization of hydrocarbons – two leading industrial processes for which faujasites are known to be the best. To this end, future efforts are highly recommended to increase the Si/Al ratio to an appropriate value.

In summary, it can be concluded that the geopolymerization is a process that is extensively studied for many applications but with a rather limited flexibility in terms of synthetic variations. By attempting initial exploration of synthetic variations, we opened up the opportunities for future researchers to develop many other new materials from geopolymer chemistry.

REFERENCES

1. Navrotsky, A., *Trans. Am. Crystallogr. Assoc.* **1993,** *27*, 1-12.

2. Swaddle, T. W.; Salerno, J.; Tregloan, P. A., *Chemical Society Reviews* **1994,** *23* (5), 319-325.

3. Cejka, J.; vanBekkum, H., *Zeolite and Ordered Mesoporous Materials: Progress and Prospects*. Elsevier B.V.: Amsterdam, 2005.

4. Armbruster, T. In *Natural zeolites: mineralogy and applications*, A. A. Balkema: 2000; pp 13-16.

5. Baerlocher, C.; McCusker, L. B., Database of Zeolite Structures. http://www.iza-structure.org/databases/: Nov 30, 2014.

6. Baerlocher, C.; Meier, W. M.; Olson, D. H., *Atlas of Zeolite Framework Types*. 5th ed.; Elsevier: Amsterdam, 2001.

7. Meier, W. M. In *Molecular Sieves*, London, Society of Chemical Industry: London, 1968; p 10.

8. Barrer, R. M., *Pure Appl. Chem* **1979,** *51*, 1091.

9. Holmes, A. Synthetic and Atomic Force Microscopy Studies of Offretite/Erionite Family Zeolites. Ph.D. Thesis, The University of Manchester, Manchester, England, 2011.

10. Loewenstein, W., *Am. Mineral.* **1954,** *39*, 92-6.

11. Breck, D. W., *Zeolite Molecular Sieves: Struture, Chemistry, and Use*. Wiley-Interscience: New York, 1974.

12. Colella, C.; Gualtieri, A. F., *Microporous and Mesoporous Materials* **2007,** *105* (3), 213-221.

13. Xu, R.; Pang, W.; Yu, J.; Huo, Q.; Chen, J., *Chemistry of Zeolites and Related Porous Materials: Synthesis and Structure*. John Wiley & Sons (Asia) Pte Ltd: Singapore, 2007.

14. Breck, D. W. Crystalline zeolite Y,. U.S. Patent 3130007, Apr 1964.

15. Pavol, H., FCC Catalyst - Key Element in Refinery Technology. In *45th International Petroleum Conference*, Bratislava, Slovak Republic, 2011.

16. Rowles, M. R.; Hanna, J. V.; Pike, K. J.; Smith, M. E.; O'Connor, B. H., *Appl. Magn. Reson.* **2007,** *32*, 663-689.

17. (a) Bell, J. L.; Sarin, P.; Provis, J. L.; Haggerty, R. P.; Driemeyer, P. E.; Chupas, P. J.; van Deventer, J. S. J.; Kriven, W. M., *Chem. Mater.* **2008,** *20*, 4768-4776; (b) Provis, J. L.; Lukey, G. C.; Van Deventer, J. S. J., *Chem. Mater.* **2005,** *17*, 3075-3085.

18. Fletcher, R. A.; MacKenzie, K. J. D.; Nicholson, C. L.; Shimada, S., *J. Eur. Ceram. Soc.* **2005,** *25*, 1471-1477.

19. (a) Kriven, W. M., *Am. Ceram. Soc. Bull.* **2010,** *89*, 31-34; (b) Provis, J. L.; Deventer, J. S. J. v., *Geopolymers: Structure, Processing, Properties and Industrial Applications*. Woodhead Publishing Limited: New York, 2009.

20. Davidovits, J., *Geopolymer: Chemistry & Applications*. Institut Geopolymere: Saint-Quentin, France, 2008.

21. Davidovits, J. Mineral polymers and methods of making them. US4349386 A, Sep 4, 1979.

22. (a) Palomo, A.; Glasser, F. P., *Br. Ceram. Trans. J.* **1992,** *91*, 107-12; (b) Rahier, H.; Van Mele, B.; Biesemans, M.; Wastiels, J.; Wu, X., *J. Mater. Sci.* **1996,** *31*, 71-9; (c) Rahier, H.; Denayer, J. F.; Van Mele, B., *J. Mater. Sci.* **2003,** *38*, 3131-3136.

23. (a) Kalina, L.; Koplik, J.; Soukal, F.; Masilko, J.; Jaskowiecova, L., *Environ. Eng. Manage. J.* **2012,** *11*, 579-584; (b) Van Jaarsveld, J. G. S.; Van Deventer, J. S. J.; Lorenzen, L., *Miner. Eng.* **1997,** *10*, 659-669.

24. Hos, J. P.; McCormick, P. G.; Byrne, L. T., *J. Mater. Sci.* **2002,** *37*, 2311-2316.

25. Xu, H.; Van Deventer, J. S. J., *Int. J. Miner. Process.* **2000,** *59*, 247-266.

26. Xu, H.; van Deventer, J. S. J.; Lukey, G. C., *Ind. Eng. Chem. Res.* **2001,** *40*, 3749-3756.

27. Kriven, W. M.; Bell, J. L.; Gordon, M., *Ceram. Trans.* **2003,** *153*, 227-250.

28. Khosravanihaghighi, A.; Paks, M., *Adv. Mater. Res. (Durnten-Zurich, Switz.)* **2013,** *685*, 76-80, 6 pp.

29. Lyon, R. E.; Sorathia, U.; Balaguru, P. N.; Foden, A.; Davidovits, J.; Davidovits, M. In *Fire response of GEOPOLYMER structural composites*, University of Arizona, Engineering Professional Development: 1996; pp 972-981.

30. Musil, S. S.; Keane, P. F.; Kriven, W. M., *Ceram. Eng. Sci. Proc.* **2014,** *34*, 123-133.

31. Teixeira-Pinto, A.; Varela, B.; Shrotri, K.; Panandiker, R. S. P.; Lawson, J., *Ceram. Eng. Sci. Proc.* **2008,** *28*, 337-345.

32. Mohd Salahuddin, M. B.; Norkhairunnisa, M.; Mustapha, F., *Ceram. Int.* **2015,** *41*, 4273-4281.

33. Provis, J. L.; Bernal, S. A., *Annu. Rev. Mater. Res.* **2014,** *44*, 299-327.

34. Kriven, W. M.; Bell, J.; Gordon, M., *Ceram. Eng. Sci. Proc.* **2004,** *25*, 57-79.

35. Suezuek, K. G.; Telle, R.; Hohmann, M.; Seiffarth, T.; Kaps, C.; Vicent, M.; Monzo, M.; Korc, G.; Kara, A.; Kara, F., *Interceram* **2012,** *61*, 350-353.

36. Davidovits, J., *Ceram. Trans.* **1993,** *37*, 165-82.

37. Provis, J. L. In *Immobilisation of toxic wastes in geopolymers*, Woodhead Publishing Ltd.: 2009; pp 421-440.

38. Boxley, C.; Nair, B.; Balaguru, P., *Ceram. Eng. Sci. Proc.* **2008,** *28*, 321-336.

39. Provis, J. L. Modelling the Formation of Geopolymers. Ph.D. Thesis, The University of Melbourne, Melbourne, Mar 2006.

40. Duxson, P.; Lukey, G. C.; Separovic, F.; Van Deventer, J. S. J., *Ind. Eng. Chem. Res.* **2005,** *44*, 832-839.

41. Duxson, P.; Mallicoat, S. W.; Lukey, G. C.; Kriven, W. M.; van Deventer, J. S. J., *Colloids Surf., A* **2007,** *292*, 8-20.

42. De Silva, P.; Sagoe-Crenstil, K., *Cement and Concrete Research* **2008,** *38* (6), 870-876.

43. (a) Bertorelli, O. L. Zeolitic pigments. U. S. Patent 2,848,346, Aug 19, 1958; (b) Bertorelli, O. L. White silicate pigments. U. S. Patent 2,739,073, Mar 20, 1956; (c) Shurling, B. E., Millman, Nathan Stabilized pigment slurries. U. S. Patent 3,291,626 A, Dec 13, 1966.

44. Upadhyay, R. D.; Kale, D. D., *Polymer International* **2001,** *50* (11), 1209-1213.

45. Upadhyay, R. D.; Kale, D. D., *J. Appl. Polym. Sci.* **2001,** *81*, 2297-2303.

46. Hackbarth, L. E. C., Joseph T. Alkali metal alumino silicates,methods for their production and compositions thereof. U.S. Patent 3,582,379 A, Jun 1, 1971.

47. Rowles, M. R. The Structural Nature of Aluminosilicate Inorganic Polymers: A Macro to Nanoscale Study. Ph.D. Thesis, Curtin University of Technology, Oct 2004.

48. Bell., J. L.; ., P. S.; Kriven., W. M., *Microscopy and Microanalysis* **2006,** *12* (Supp 2), 738.

49. Barrer, R. M.; Mainwaring, D. E., *J. Chem. Soc., Dalton Trans.* **1972**, 2534-46.

50. Duxson, P.; Fernandez-Jimenez, A.; Provis, J. L.; Lukey, G. C.; Palomo, A.; Deventer, J. S. J., *J. Mater. Sci.* **2007,** *42*, 2917-2933.

51. Kriven., W. M.; Gorodn., M.; Bell, J. L., *Microscopy and Microanalysis* **2004,** *10* (Suppl 2), 404.

52. Bauer, A.; Velde, B.; Berger, G., *Appl. Geochem.* **1998,** *13*, 619-629.

53. Everett, D. H., *Pure Appl. Chem* **1972,** *31* (4), 577.

54. (a) Vermeiren, W.; Gilson, J. P., *Top. Catal.* **2009,** *52* (9), 1131-1161; (b) Kulprathipanja, S. Zeolites in industrial separation and catalysis; (c) Cejka., J.; Herman vanBekkum; Corma., A. Introduction to Zeolite Molecular Sieves. http://public.eblib.com/EBLPublic/PublicView.do?ptiID=311426.

55. Mintova, S.; Gilson, J.-P.; Valtchev, V., *Nanoscale* **2013,** *5*, 6693-6703.

56. Perez-Ramirez, J.; Christensen, C. H.; Egeblad, K.; Christensen, C. H.; Groen, J. C., *Chemical Society Reviews* **2008,** *37* (11), 2530-2542.

57. (a) Jacobsen, C. J. H.; Madsen, C.; Houzvicka, J.; Schmidt, I.; Carlsson, A., *Journal of the American Chemical Society* **2000,** *122* (29), 7116-7117; (b) Zhu, H.; Liu, Z.; Wang, Y.; Kong, D.; Yuan, X.; Xie, Z., *Chemistry of Materials* **2007,** *20* (3), 1134-1139.

58. (a) Larsen, S. C., *The Journal of Physical Chemistry C* **2007,** *111* (50), 18464-18474; (b) Zhan, B.-Z.; White, M. A.; Robertson, K. N.; Cameron, T. S.; Gharghouri, M., *Chemical Communications* **2001,** (13), 1176-1177.

59. Valtchev, V.; Majano, G.; Mintova, S.; Perez-Ramirez, J., *Chemical Society Reviews* **2013,** *42* (1), 263-290.

60. (a) Verboekend, D.; Perez-Ramirez, J., *Catalysis Science & Technology* **2011,** *1* (6), 879-890; (b) Verboekend, D.; Vilé, G.; Pérez-Ramírez, J., *Advanced Functional Materials* **2012,** *22* (5), 916-928.

61. Verboekend, D.; Keller, T. C.; Mitchell, S.; Pérez-Ramírez, J., *Advanced Functional Materials* **2013,** *23* (15), 1923-1934.

62. Forsgren, J.; Pedersen, C.; Stromme, M.; Engqvist, H., *PLoS One* **2011,** *6*, e17759.

63. Jamstorp, E.; Stromme, M.; Frenning, G., *J Pharm Sci* **2011,** *100*, 4338-48.

64. Cai, B.; Mellgren, T.; Bredenberg, S.; Engqvist, H., *Ceram. Eng. Sci. Proc.* **2014,** *34*, 49-56.

65. Okada, K.; Ooyama, A.; Isobe, T.; Kameshima, Y.; Nakajima, A.; MacKenzie, K. J. D., *J. Eur. Ceram. Soc.* **2009,** *29*, 1917-1923.

66. O'Connor, S. J.; MacKenzie, K. J. D.; Smith, M. E.; Hanna, J. V., *Journal of Materials Chemistry* **2010,** *20* (45), 10234-10240.

67. Skorina, T., *Appl. Clay Sci.* **2014,** *87*, 205-211.

68. Sazama, P.; Bortnovsky, O.; Dedecek, J.; Tvaruzkova, Z.; Sobalik, Z., *Catal. Today* **2011,** *164*, 92-99.

69. (a) Gasca-Tirado, J. R.; Manzano-Ramirez, A.; Vazquez-Landaverde, P. A.; Herrera-Diaz, E. I.; Rodriguez-Ugarte, M. E.; Rubio-Avalos, J. C.; Amigo-Borras, V.; Chavez-Paez, M., *Mater. Lett.* **2014,** *134*, 222-224; (b) Masliana, M.; Kenneth, J. D. M.; Meor, Y. M. S.; Wilfred, S. P.; Nur, A. S., *Solid State Sci. Technol.* **2013,** *21*, 23-30.

70. Sharma., S.; Medpelli., D.; Seo, D. K. *Calcium-Modified Hierarchically Porous Aluminosilicate Geopolymer as a Highly Efficient Regenerable Catalyst for Biodiesel Production*; *RSC Advances.*, submitted for publication, 2015.

71. Cullity, B. D., In *Elements of x-ray diffraction*, Addison-Wesley Pub. Co.: Reading, Massachusetts, 1978.

72. Bragg, W. L., *Proc. Cambridge Philos. Soc.* **1912,** *17*, 43-57.

73. Arthur W. Chester, E. G. D., *Zeolite Characterization and Catalysis*. Springer Science & Business Media: London, 2009.

74. Monshi, A.; Foroughi, M. R.; Monshi, M. R., *World J. Nano Sci. Eng.* **2012,** *2*, 154-160, 7 pp.

75. Patterson, A. L., *Physical Review* **1939,** *56* (10), 978-982.

76. Rowles, M.; O'Connor, B., *Journal of Materials Chemistry* **2003,** *13* (5), 1161-1165.

77. Yang, S.; Navrotsky, A.; Phillips, B. L., *The Journal of Physical Chemistry B* **2000,** *104* (25), 6071-6080.

78. Zhan, B.-Z.; White, M. A.; Lumsden, M.; Mueller-Neuhaus, J.; Robertson, K. N.; Cameron, T. S.; Gharghouri, M., *Chemistry of Materials* **2002,** *14* (9), 3636-3642.

79. Sing, K. S. W.; Everett, D. H.; Haul, R. A. W.; Moscou, L.; Pierotti, R. A.; Rouquerol, J.; Siemieniewska, T., *Pure Appl. Chem.* **1985,** *57*, 603-19.

80. Lippens, B. C.; de Boer, J. H., *Journal of Catalysis* **1965,** *4* (3), 319-323.

81. William, D. B.; Carter, C. B., *Transmission electron microscopy – A textbook for materials science.* 2nd ed.; Springer: New York, 2009.

82. Terasaki, O.; Ohsuna, T., *Catal. Today* **1995,** *23*, 201-18.

83. Bursill, L. A.; Thomas, J. M.; Rao, K. J., *Nature* **1981,** *289* (5794), 157-158.

84. Bursill, L. A.; Lodge, E. A.; Thomas, J. M., *Nature (London)* **1980,** *286*, 111-13.

85. Csencsits, R.; Gronsky, R., *Ultramicroscopy* **1987,** *23* (3–4), 421-431.

86. Anderson, M. W.; Agger, J. R.; Thornton, J. T.; Forsyth, N., *Angewandte Chemie International Edition in English* **1996,** *35* (11), 1210-1213.

87. Cao, A., *Anal. Lett.* **2003,** *36* (15), 3185-3225.

88. . *Zetasizer APS User Manual* December 2008. http://www.malvern.com/en/.

89. . *Dynamic Light Scattering Training: Achieving reliable nano particle sizing* 2012. http://www.atascientific.com.au/.

90. . *Zeta sizer nano series technical note* 2010. www.malvern.co.uk.

91. Freire, J. M.; Domingues, M. M.; Matos, J.; Melo, M. N.; Veiga, A. S.; Santos, N. C.; Castanho, M. A. R. B., *Eur. Biophys. J.* **2011,** *40*, 481-487.

92. Evans, D. F.; Wennerstrom, H., *The Colloidal Domain: Where Physics, Chemistry, Biology, and Technology Meet* 2nd ed.; Wiley-VCH: New York, 1999.

93. (a) Davidovits, J., *J. Therm. Anal.* **1991,** *37*, 1633-56; (b) J. L. Provis, J. S. J. v. D., Introduction to Geopolymers. In *Introduction to Geopolymers*, L. Provis, G. C. L., J. S. J. van Deventer, Ed. Woodhead Publishing: Cambridge, UK, 2009; pp 16-26.

94. Jaemstorp, E.; Stromme, M.; Frenning, G., *J. Pharm. Sci.* **2011,** *100*, 4338-4348.

95. Seo, D.; Medpelli, D.; Seo, J. Porous geopolymer materials. U.S. Patent No. US20130055924 A1, Mar 7, 2013.

96. Tadros, T. F. In *Emulsion science and technology: A general introduction*, Wiley-VCH Verlag GmbH & Co. KGaA: 2009; pp 1-56.

97. Gunstone, F. D., *The Chemistry of Oils and Fats: Sources, Composition, Properties, and Uses*. Blackwell Publishing: Oxford, UK, 2004, 2004.

98. Brunauer, S.; Emmett, P. H.; Teller, E., *Journal of the American Chemical Society* **1938,** *60* (2), 309-319.

99. Barrett, E. P.; Joyner, L. G.; Halenda, P. P., *Journal of the American Chemical Society* **1951,** *73* (1), 373-380.

100. Condon, J. B., *Surface Area and Porosity Determinations by Physisorption: Measurements and Theory*. Elsevier Science: Amsterdam, The Netherlands, 2006.

101. Duxson, P.; Provis, J. L.; Lukey, G. C.; Mallicoat, S. W.; Kriven, W. M.; van Deventer, J. S. J., *Colloids and Surfaces A: Physicochemical and Engineering Aspects* **2005,** *269* (1‑3), 47-58.

102. Cilla, M. S.; Morelli, M. R.; Colombo, P., *Journal of the European Ceramic Society* **2014,** *34* (12), 3133-3137.

103. Jaemstorp, E.; Stromme, M.; Frenning, G., *J. Pharm. Sci.* **2011,** *100* (10), 4338-4348.

104. Medpelli, D.; Seo, J.-M.; Seo, D.-K., *J. Am. Ceram. Soc.* **2014,** *97*, 70-73.

105. KASIL® 6, PQ Corporation. http://www.pqcorp.com/Portals/1/docs/KASIL_6.pdf, accessed November 2012.

106. MetaMax PA Technical Bulletin, BASF. http://kaolin.basf.com/products/application/metamax, accessed November 2012.

107. Kriven, W. M.; Gordon, M.; Bell, J. L., *Microscopy and Microanalysis* **2004,** *10* (SupplementS02), 404-405.

108. Mandal, B. K.; Suzuki, K. T., *Talanta* **2002,** *58* (1), 201-235.

109. (a) Mackenzie, F.; Lantzy, R.; Paterson, V., *Mathematical Geology* **1979,** *11* (2), 99-142; (b) Mohan, D.; Pittman Jr, C. U., *Journal of Hazardous Materials* **2007,** *142* (1‑2), 1-53.

110. (a) Karim, M. M., *Water Research* **2000,** *34* (1), 304-310; (b) Da, D.; Chatterjee, A.; Mandal, B. K.; Samanta, G.; Chakraborti, D.; Chanda, B., *Analyst (Cambridge, U. K.)* **1995,** *120*, 917-24; (c) Chaterjee, A.; Das, D.; Mandal, B. K.; Chowdhury, T. R.; Samanta, G.; Chakraborti, D., *Analyst (Cambridge, U. K.)* **1995,** *120*, 643-50.

111. Jain, C. K.; Ali, I., *Water Research* **2000,** *34* (17), 4304-4312.

112. (a) *Arsenic*. Agency for Toxic Substances & Disease Registry: 2011; (b) Mulgundmath, V. P.; Tezel, F. H.; Saatcioglu, T.; Golden, T. C., *Can. J. Chem. Eng.* **2012,** *90*, 730-738.

113. *WHO (Press), Guidelines for Drinking-water Quality, 3rd ed.* World Health Organization: Geneva, 2008.

114. Dutta, P. K.; Ray, A. K.; Sharma, V. K.; Millero, F. J., *Journal of Colloid and Interface Science* **2004,** *278* (2), 270-275.

115. (a) Jain, C. K.; Singh, R. D., *Journal of Environmental Management* **2012,** *107* (0), 1-18; (b) Sylvester, P.; Westerhoff, P.; Moeller, T.; Badruzzaman, M.; Boyd, O., *Environ. Eng. Sci.* **2007,** *24*, 104-112; (c) Gallegos-Garcia, M.; Ramirez-Muniz, K.; Song, S., *Miner. Process. Extr. Metall. Rev.* **2012,** *33*, 301-315.

116. Jang, M.; Min, S.-H.; Kim, T.-H.; Park, J. K., *Environmental Science & Technology* **2006,** *40* (5), 1636-1643.

117. (a) Lenoble, V.; Bouras, O.; Deluchat, V.; Serpaud, B.; Bollinger, J.-C., *J. Colloid Interface Sci.* **2002,** *255*, 52-58; (b) Singh, D. B.; Prasad, G.; Rupainwar, D. C., *Colloids Surf., A* **1996,** *111*, 49-56.

118. Driehaus, W.; Jekel, M.; Hildebrandt, U., *Aqua (Oxford)* **1998,** *47*, 30-35.

119. Badruzzaman, M.; Westerhoff, P.; Knappe, D. R. U., *Water Res.* **2004,** *38*, 4002-4012.

120. (a) Gu, Z.; Fang, J.; Deng, B., *Environmental Science & Technology* **2005,** *39* (10), 3833-3843; (b) Gu, Z.; Deng, B., *Environ. Eng. Sci.* **2007,** *24*, 113-121; (c) Guo, X.; Chen, F., *Environmental Science & Technology* **2005,** *39* (17), 6808-6818; (d) Chen, X.; Lam, K. F.; Zhang, Q.; Pan, B.; Arruebo, M.; Yeung, K. L., *J. Phys. Chem. C* **2009,** *113*, 9804-9813.

121. Pham, A. L.-T.; Sedlak, D. L.; Doyle, F. M., *Appl. Catal., B* **2012,** *126*, 258-264.

122. (a) Dunphy, D. R.; Singer, S.; Cook, A. W.; Smarsly, B.; Doshi, D. A.; Brinker, C. J., *Langmuir* **2003,** *19*, 10403-10408; (b) Glasspoole, B. W.; Webb, J. D.; Crudden, C. M., *J. Catal.* **2009,** *265*, 148-154; (c) Xia, Y.; Mokaya, R., *J. Phys. Chem. B* **2003,** *107*, 6954-6960.

123. Duxson, P.; Provis, J. L.; Lukey, G. C.; van Deventer, J. S. J., *Cem. Concr. Res.* **2007,** *37*, 1590-1597.

124. Komnitsas, K.; Zaharaki, D., *Miner. Eng.* **2007,** *20*, 1261-1277.

125. Sazama, P.; Bortnovsky, O.; Dědeček, J.; Tvarůžková, Z.; Sobalík, Z., *Catalysis Today* **2011,** *164* (1), 92-99.

126. Jaemstorp, E.; Forsgren, J.; Bredenberg, S.; Engqvist, H.; Stroemme, M., *J. Controlled Release* **2010,** *146*, 370-377.

127. Seo, D.; Medpelli, D.; Seo, J. Porous geopolymer materials. U. S. Patent 20130055924 A1, Mar 7, 2013.

128. Hristovski, K. D.; Westerhoff, P. K.; Crittenden, J. C.; Olson, L. W., *Separation Science and Technology* **2008,** *43* (11-12), 3154-3167.

129. Hristovski, K.; Westerhoff, P.; Möller, T.; Sylvester, P.; Condit, W.; Mash, H., *Journal of Hazardous Materials* **2008,** *152* (1), 397-406.

130. Westerhoff, P.; Highfield, D.; Badruzzaman, M.; Yoon, Y., *Journal of Environmental Engineering* **2005,** *131* (2), 262-271.

131. *Toxicity Characteristic Leaching Procedure, 40 Codes of Regulations*. U.S. Environmental Protection Agency: Washington, DC, 1992; Part 261, p 31: 1992.

132. Bandyopadhyay, M.; Birkner, A.; van den Berg, M. W. E.; Klementiev, K. V.; Schmidt, W.; Grünert, W.; Gies, H., *Chemistry of Materials* **2005,** *17* (15), 3820-3829.

133. Davidovits, J., *Journal of Thermal Analysis and Calorimetry* **1991,** *37* (8), 1633-1656.

134. Plastics-Europe, *Plastics - The Facts 2013*. Association of Plastics Manufacturers: Brussels, Belgium, 2013.

135. Hussain, F.; Hojjati, M.; Okamoto, M.; Gorga, R. E., *Journal of Composite Materials* **2006,** *40* (17), 1511-1575.

136. Pukanszky, B., *Composites (Guildford, U. K.)* **1990,** *21*, 255-62.

137. Fröhlich, J.; Niedermeier, W.; Luginsland, H. D., *Composites Part A: Applied Science and Manufacturing* **2005,** *36* (4), 449-460.

138. Mostafa, A.; Abouel-Kasem, A.; Bayoumi, M. R.; El-Sebaie, M. G., *J. Test. Eval.* **2010,** *38*, 347-359.

139. (a) Schaefer, D. W., Chen, C., Yang, A.J.M. Partially neutralizing silicate solution with acid to form silica primary particles, heating silicate solution, providing silicic acid solution having reduced ionic strength by passing diluted silicate solution through ion-exchange resin, adding to silicate to agglomerate silica particles. 2010; (b) Majumdar, S., *Rubber India* **2005,** *57*, 21-25.

140. Thomas, S., Stephen, R., *Rubber Nanocomposites: Preparation, Properties, and Applications*. John Wiley & Sons (Asia) Pte Ltd: Singapore, 2010.

141. (a) Hilonga, A.; Kim, J.-K.; Sarawade, P.; Quang, D.; Shao, G.; Elineema, G.; Kim, H., *Korean J. Chem. Eng.* **2012,** *29* (11), 1643-1646; (b) Hilonga, A.; Kim, J.-K.; Sarawade, P. B.; Quang, D. V.; Shao, G. N.; Elineema, G.; Kim, H. T., *Journal of Industrial and Engineering Chemistry* **2012,** *18* (5), 1841-1844.

142. De Witte, B. M.; Uytterhoeven, J. B., *Journal of Colloid and Interface Science* **1996,** *181* (1), 200-207.

143. Brunauer, S.; Emmett, P. H.; Teller, E., *J. Am. Chem. Soc.* **1938,** *60*, 309-19.

144. Barrett, E. P.; Joyner, L. G.; Halenda, P. P., *J. Am. Chem. Soc.* **1951,** *73*, 373-80.

145. Rouquerol, J.; Avnir, D.; Fairbridge, C. W.; Everett, D. H.; Haynes, J. M.; Pernicone, N.; Ramsay, J. D. F.; Sing, K. S. W.; Unger, K. K., *Pure and Applied Chemistry* **1994,** *66* (8), 1739.

146. Vilgis, T. A. H., G. and Kluppel, M., *Reinforcement of Polymer Nano-Composites: Theory, Experiments and Applications*. Cambridge University Press: New York, 2009; p 204.

147. Laine, J. Utilisation of nanotechnology in forest products technology. https://noppa.aalto.fi/noppa/kurssi/puu-19.4020/luennot/Puu-19_4020_utilization_of_nanotechnology.pdf.

148. Abdelwahed, W.; Degobert, G.; Stainmesse, S.; Fessi, H., *Advanced Drug Delivery Reviews* **2006,** *58* (15), 1688-1713.

149. Iler, R. K., *The Chemistry of Silica*. John Wiley & Sons: New York, 1979.

150. Schweitzer, G. K., Pesterfield, L. L., *The Aqueous Chemistry of the Elements*. Oxford University Press: New York, 2010; p 434.

151. Otterstedt, J. E. a. B., D. A., *Small Particle Technology*. Plenum Press: New York, 1998; p 524.

152. George A. Joyce, W. M. H., Anthony W. Thornton, John C. Hodgin, Carbon black intra-aggregate void volume from dynamic compression measurements. *Rubber World* Sep, 2011.

153. Davidovits, J., *Geopolymer Chemistry and Applications*. 3rd ed.; Institut Géopolymère: Saint-Quentin, France, 2011.

154. *United States Climate Action Report*; U.S. Department of State: Washington, 2014.

155. Haszeldine, R. S., *Science (Washington, DC, U. S.)* **2009,** *325*, 1647-1652.

156. (a) Li, B.; Duan, Y.; Luebke, D.; Morreale, B., *Appl. Energy* **2013,** *102*, 1439-1447; (b) Lee, S.-Y.; Park, S.-J., *Journal of Industrial and Engineering Chemistry*.

157. Choi, S.; Drese, J. H.; Jones, C. W., *ChemSusChem* **2009,** *2* (9), 796-854.

158. (a) Webley, P., *Adsorption* **2014,** *20* (2-3), 225-231; (b) Ho, M. T.; Allinson, G. W.; Wiley, D. E., *Ind. Eng. Chem. Res.* **2008,** *47*, 4883-4890.

159. (a) Maring, B. J.; Webley, P. A., *International Journal of Greenhouse Gas Control* **2013,** *15* (0), 16-31; (b) Harlick, P. J. E.; Tezel, F. H., *Microporous Mesoporous Mater.* **2004,** *76*, 71-79; (c) Cheung, O.; Hedin, N., *RSC Advances* **2014,** *4* (28), 14480-14494.

160. Buelow, M., *Adsorption* **2002,** *8*, 9-14.

161. (a) Cheung, O.; Bacsik, Z.; Liu, Q.; Mace, A.; Hedin, N., *Applied Energy* **2013,** *112*, 1326-1336; (b) Cheung, O.; Bacsik, Z.; Krokidas, P.; Mace, A.; Laaksonen, A.; Hedin, N., *Langmuir* **2014,** *30* (32), 9682-9690; (c) Akhtar, F.; Liu, Q.; Hedin, N.; Bergstroem, L., *Energy Environ. Sci.* **2012,** *5*, 7664-7673.

162. Gueudre, L.; Milina, M.; Mitchell, S.; Perez-Ramirez, J., *Adv. Funct. Mater.* **2014,** *24*, 174.

163. (a) Seo, D.-K.; Seo, J.; Medpelli, D. Porous nanostructured geopolymer materials. WO2011068830A2, 2011; (b) Seo, D.-K.; Medpelli, D.; Ladd, D.; Mesgar, M. Geopolymer resin materials, geopolymer materials, and materials produced thereby. WO2013044016A2, 2013.

164. (a) Provis, J. L.; van, D. J. S. J.; Editors, *Geopolymers: Structure, Processing, Properties and Industrial Applications*. Woodhead Publishing Ltd.: 2009; p 454 pp; (b) Rowles, M.; O'Connor, B., *J. Mater. Chem.* **2003,** *13*, 1161-1165.

165. Cundy, C. S.; Cox, P. A., *Chemical Reviews* **2003,** *103* (3), 663-702.

166. Kriven, W. M.; Bell, J. L.; Gordon, M., Microstructure and Microchemistry of Fully-Reacted Geopolymers and Geopolymer Matrix Composites. In *Advances in Ceramic Matrix Composites IX*, John Wiley & Sons, Inc.: 2006; pp 227-250.

167. Walton, R. I.; Millange, F.; O'Hare, D.; Davies, A. T.; Sankar, G.; Catlow, C. R. A., *J. Phys. Chem. B* **2001,** *105*, 83-90.

168. Huang, Y.; Wang, K.; Dong, D.; Li, D.; Hill, M. R.; Hill, A. J.; Wang, H., *Microporous and Mesoporous Materials* **2010,** *127* (3), 167-175.

169. (a) Condon, J. B., Chapter 1 - An Overview of Physisorption. In *Surface Area and Porosity Determinations by Physisorption*, Condon, J. B., Ed. Elsevier Science: Amsterdam, 2006; pp 1-27; (b) Sing, K. S. W.; Everett, D. H.; Haul, R. A. W.; Moscou, L.; Pierotti, R. A.; Rouquerol, J.; Siemieniewsk, T., *Pure Appl. Chem.* **1985,** *57* (4), 603-619.

170. (a) Storck, S.; Bretinger, H.; Maier, W. F., *Appl. Catal., A* **1998,** *174*, 137-146; (b) Malvadkar, N. A.; Sekeroglu, K.; Dressick, W. J.; Demirel, M. C., *J. Power Sources* **2011,** *196*, 8553-8560.

171. (a) Groen, J. C. Mesoporus Zeolites Obtained by Desilication. Technische Universiteit Delft, 2007; (b) Jiri Cejka, A. C., Stacey Zones, *Zeolites and Catalysis: Synthesis, Reactions and Applications*. WILEY-VCH Verlag GmbH & Co. KGaA: Weinheim, 2010.

172. Robson, H.; Editor, *Verified Synthesis of Zeolitic Materials, Second Edition*. Elsevier: 2001; p 272 pp.

173. (a) Akhtar, F.; Andersson, L.; Ogunwumi, S.; Hedin, N.; Bergstroem, L., *J. Eur. Ceram. Soc.* **2014,** *34*, 1643-1666; (b) Li, G.; Xiao, P.; Webley, P.; Zhang, J.; Singh, R.; Marshall, M., *Adsorption* **2008,** *14*, 415-422; (c) D'Alessandro, D. M.; Smit, B.; Long, J. R., *Angew. Chem., Int. Ed.* **2010,** *49*, 6058-6082; (d) Siriwardane, R. V.; Shen, M.-S.; Fisher, E. P.; Losch, J., *Energy Fuels* **2005,** *19*, 1153-1159.

174. Cavenati, S.; Grande, C. A.; Rodrigues, A. E., *Journal of Chemical & Engineering Data* **2004,** *49* (4), 1095-1101.

175. Harlick, P. J. E.; Tezel, F. H., *Adsorption* **2000,** *6*, 293-309.

176. Xu, X.; Song, C.; Wincek, R.; Andresen, J. M.; Miller, B. G.; Scaroni, A. W., *Prepr. Symp. - Am. Chem. Soc., Div. Fuel Chem.* **2003,** *48*, 162-163.

177. (a) Myers, A. L.; Prausnitz, J. M., *AIChE J.* **1965,** *11*, 121-7; (b) Yang, R. T.; Editor, *Gas Separation by Adsorption Processes*. World Sci: 1997; p 360.

178. (a) Nugent, P.; Belmabkhout, Y.; Burd, S. D.; Cairns, A. J.; Luebke, R.; Forrest, K.; Pham, T.; Ma, S.; Space, B.; Wojtas, L.; Eddaoudi, M.; Zaworotko, M. J., *Nature (London, U. K.)* **2013,** *495*, 80-84; (b) Babarao, R.; Hu, Z.; Jiang, J.; Chempath, S.; Sandler, S. I., *Langmuir* **2007,** *23*, 659-666; (c) Mason, J. A.; Sumida, K.; Herm, Z. R.; Krishna, R.; Long, J. R., *Energy Environ. Sci.* **2011,** *4*, 3030-3040.

179. Bae, T.-H.; Hudson, M. R.; Mason, J. A.; Queen, W. L.; Dutton, J. J.; Sumida, K.; Micklash, K. J.; Kaye, S. S.; Brown, C. M.; Long, J. R., *Energy & Environmental Science* **2013,** *6* (1), 128-138.

180. Liu, Q.; Mace, A.; Bacsik, Z.; Sun, J.; Laaksonen, A.; Hedin, N., *Chemical Communications* **2010,** *46* (25), 4502-4504.

181. Huang, Q.; Eić, M., *Separation and Purification Technology* **2013,** *103*, 203-215.

182. Goj, A.; Sholl, D. S.; Akten, E. D.; Kohen, D., *J. Phys. Chem. B* **2002,** *106*, 8367-8375.

183. Graham, C.; Imrie, D. A.; Raab, R. E., *Mol. Phys.* **1998,** *93*, 49-56.

184. (a) Liu, Q.; Mace, A.; Bacsik, Z.; Sun, J.; Laaksonen, A.; Hedin, N., *Chem. Commun. (Cambridge, U. K.)* **2010,** *46*, 4502-4504; (b) Akhtar, F.; Andersson, L.; Keshavarzi, N.; Bergstroem, L., *Appl. Energy* **2012,** *97*, 289-296.

185. (a) Bertsch, L.; Habgood, H. W., *J. Phys. Chem.* **1963,** *67*, 1621-8; (b) Ward, J. W.; Habgood, H. W., *J. Phys. Chem.* **1966,** *70*, 1178-82; (c) Gallei, E.; Stumpf, G., *Journal of Colloid and Interface Science* **1976,** *55* (2), 415-420.

186. (a) Ojuva, A.; Akhtar, F.; Tomsia, A. P.; Bergstroem, L., *ACS Appl. Mater. Interfaces* **2013,** *5*, 2669-2676; (b) Ruthven, D. M., *Stud. Surf. Sci. Catal.* **2007,** *168*, 701-736.